Magnetic resonance imaging of lung cancer in the presence of respiratory motion:
Dynamic keyhole and audiovisual biofeedback

by

Danny Kyejun Lee

A thesis submitted to the Sydney Medical School in fulfilment
of the requirements for the degree of

Doctor of Philosophy
in
Medical Physics

Faculty of Medicine
University of Sydney
2016

To my wife, *Su Kyong*.

Declaration of Originality

I, Danny Kyejun Lee, declare that this thesis is my own work and has not been submitted in any form for another degree or diploma at any university or other institute of tertiary education. Information derived from the published and unpublished work of others has been acknowledged in the text and a list of references is given in the bibliography.

Abstract

Breath-to-breath variations in breathing can cause image artefacts. Day-to-day variations can cause a disagreement of position and volume between planning and treatment throughout radiotherapy procedures, requiring a larger treatment margin and longer treatment time. An advanced radiotherapy system requires: (1) a fast imaging technique for the compensation of breathing variations and/or (2) a respiratory motion management technique for the control of breathing variations.

To achieve the goals of the advanced radiotherapy system, we propose a fast imaging technique to directly visualise lung tumours and the use of a respiratory guidance to control lung tumour motions. Significant efforts were made to assess the fast imaging technique and the use of respiratory guidance throughout the acquisition of healthy volunteer and lung cancer patient data in an ethics approved MRI imaging study. Fifteen lung cancer patients were scanned from March 2013 to February 2016. MRI datasets were obtained with and without audiovisual (AV) biofeedback guidance and they were also utilized for MRI reconstruction simulations.

A novel MRI reconstruction method called "Dynamic keyhole" was proposed as a fast imaging technique to reduce acquisition time and simultaneously improve image quality by reducing respiratory-related artefacts in the presence of respiratory motion. The dynamic keyhole method utilizes a library of previously acquired, peripheral k-space datasets from the closest respiratory state in conjunction with central k-space datasets acquired in real-time. This thesis investigated (1) the concept of this method in terms of the improvement in temporal resolution with healthy volunteer MRI datasets and (2) the applicability of real-time lung tumour localization in terms of the accuracy of tumour motion and shape with lung cancer patient MRI datasets. The dynamic keyhole method achieved an increase in imaging frequency by up to a factor of five when compared with full k-space methods whilst achieving sub-millimetre tumour motion accuracy and preserving tumour shape within 98%. This method is a promising technique for clinical applications such as real-time image-guided cancer radiotherapy in thoracic and abdominal regions.

AV biofeedback respiratory guidance was used for healthy volunteers and lung cancer patients. This thesis investigated the impact of AV biofeedback on (1) intra- and inter-fraction lung tumour motion using cine-MRI, (2) inter-fraction lung tumour position and intra-fraction tumour volume using breath-hold MRI and (3) the improvement in image quality and the reduction in scan time using respiratory-gated MRI. AV biofeedback respiratory guidance improved intra- and inter-fraction tumour motion and position reproducibility, and intra-fraction tumour volume consistency. In addition, it was found to improve image quality and reduce scan time. These results demonstrated that AV biofeedback can facilitate reproducible tumour motion and position, and consistent tumour volume, which is advantageous towards achieving more accurate medical imaging and radiation therapy procedures.

The performance of the dynamic keyhole method and AV biofeedback respiratory guidance shown in this thesis illustrates potential advantages of real-time tumour imaging and tumour motion management in the course of lung cancer radiotherapy.

Acknowledgements

First and foremost, I would like to express utmost gratitude to my supervisor, Professor Paul Keall, for continued guidance, encouragement and support during my Ph.D. study. He continually and convincingly conveyed a spirit of adventure in regard to research progress, scholarships, manuscripts and this thesis. I could not have imagined having a better supervisor for my Ph.D. studies.

My sincerest thank goes to Professor Peter Greer who provided me an opportunity to access CT and MRI scanners for clinical trials in Calvary Mater Newcastle and Department of Radiation Oncology, and who allowed me access to the laboratory and research facilities. Without his support it would not be possible to conduct this research.

My very special thank goes out to Dr. Taeho Kim. Without his motivation and encouragement I would not have considered a graduate career in Medical Physics. He is the one who truly made a difference in my life. I developed focus and became interested in lung cancer radiotherapy. I doubt that I will ever be able to convey my full appreciation, but I owe him my eternal gratitude.

I must acknowledge Julie Baz, Dr. Robyn Keall, Sean Pollock, Brendan Whelan and Dr. Ricky O'Brien for reviewing papers, and Dr. Ricky O'Brien, Sean Pollock and Kuldeep Makhija for the technical support of AV biofeedback. Appreciation also goes out to Jameen Arm for the study design of MRI, Perry Hunter for his help with patient breathing training with AV biofeedback, Dr. Joanna Ludbrook for the recruitment of lung cancer patients and Dr. Carminia Lapuz for contouring lung tumour. Thanks also goes out to all members of Radiation Physics Laboratory who

provided me with statistical advice at times of critical need, which helped enrich the experience.

I recognize that this research would not have been possible without the financial assistance of NHMRC Australia Fellowship, NHMRC Program Grant APP1036078, ARC Discovery Grant DP120100821, Calvary Mater Newcastle Department of Radiation Oncology for MRI research scan funding, University of Sydney Postgraduate Awards and Australian Postgraduate Awards.

Last but not the least, I would like to thank my family for the support they provided me through my entire life and I must acknowledge my wife and three children William, Harry and Kristina without whose love, encouragement and assistance, I would not have finished my Ph.D. study.

Table of Contents

List of Figures

List of Tables

List of Publications

First author publications

2014 As Chapter 3: Dynamic keyhole: A novel method to improve MR images in the presence of respiratory motion for real-time MRI

Dynamic keyhole: A novel method to improve MR images in the presence of respiratory motion for real-time MRI
D. Lee, S. Pollock, B. Whelan, P. Keall and T. Kim
Medical physics, **41** (7): 072304 (2014)

2016 As Chapter 4: Quantifying the accuracy of the tumor motion and area as a function of acceleration factor for the simulation of the dynamic keyhole magnetic resonance imaging method

Quantify the accuracy of the tumor motion and area as a function of acceleration factor for the simulation of the dynamic keyhole imaging method
D. Lee, P. B. Greer, S. Pollock, T. Kim and P. Keall
Medical physics, **43** (5): 2639 (2016)

2015 As Chapter 5: Audiovisual Biofeedback Improves Cine-Magnetic Resonance Imaging Measured Lung Tumor Motion Consistency

Audiovisual Biofeedback Improves Cine-Magnetic Resonance Imaging Measured Lung Tumor Motion Consistency

D. Lee, B. P. Greer, J. Ludbrook, J. Arm, P. Hunter, S. Pollock, K. Makhija, T. R. O'Brien, T. Kim and P. Keall

Int J Radiat Oncol Biol Phys, **94** (3): 628 (2016)

2014 As Chapter 7: Audiovisual biofeedback improves image quality and reduces scan time for respiratory-gated 3D MRI

Audiovisual biofeedback improves image quality and reduces scan time for respiratory-gated 3D MRI

D. Lee, P. Greer, J. Arm, P. Keall and T. Kim

Journal of Physics: Conference Series, **489** (1): 012033 (2014)

Co-author publications

2012 **Audiovisual biofeedback improves diaphragm motion reproducibility in MRI**

T. Kim, S. Pollock, D. Lee, R. O’Brien and P. Keall

Medical physics, **39** (11): 6921 (2012)

2013 **Audiovisual biofeedback improves motion prediction accuracy**

S. Pollock, D. Lee, P. Keall and T. Kim

Medical physics, **40** (4): 041705 (2013)

2014 **The internal–external respiratory motion correlation is unaffected by audiovisual biofeedback**

H. Steel, S. Pollock, D. Lee, P. Keall, T. Kim

Australasian Physical & Engineering Sciences in Medicine, **37** (1): 97 (2014)

2014 **Quasi-breath-hold (QBH) Biofeedback in Gated 3D Thoracic MRI: Feasibility Study**

T. Kim, R. Pooley, D. Lee, P. Keall, R. Lee and S. Kim

Progress in Medical Physics, **25** (2): 72 (2014)

2015 **Quantification of lung tumor rotation with automated landmark extraction using orthogonal cine MRI images**

C. Paganelli, D. Lee, P. B. Greer, G. Baroni, M. Riboldi and P. Keall

Physics in Medicine and Biology, **60** (18): 7165 (2015)

2016 **Motion prediction in MRI-guided radiotherapy based on interleaved orthogonal cine-MRI**

M. Seregni, C. Paganelli, D. Lee, P. Greer, G. Baroni, P. Keall and M. Riboldi

Physics in Medicine and Biology, **61** (2): 872 (2016)

Submitted

2016 As Chapter 6: Audiovisual biofeedback guided breath-hold improves lung tumor position reproducibility and volume consistency

Audiovisual biofeedback guided breath-hold improves lung tumor position reproducibility and volume consistency

D. Lee, B. P. Greer, C. Lapuz, J. Ludbrook, S. Pollock, T. Kim and P. Keall

Radiotherapy and Oncology, (2016)

List of Presentations

International Conferences (First author only)

Jul 2015	Audiovisual biofeedback improves breath-hold lung tumor position reproducibility measured with 4D MRI *American Association of Physicists in Medicine Annual Meeting 2015* Anaheim California, US
Jul 2015	Audiovisual biofeedback improves the correlation between internal and external respiratory motion *American Association of Physicists in Medicine Annual Meeting 2015* Anaheim, California, US
Sep 2014	Audiovisual biofeedback improves tumour motion consistency for lung cancer patients *Combined Scientific Meeting 2014* Melbourne, Australia
Sep 2014	Respiratory motion based dynamic keyhole reconstruction for real-time thoracic MRI *Combined Scientific Meeting 2014* Melbourne, Australia
Jul 2014	Audiovisual biofeedback improves tumor motion consistency for lung cancer patients *American Association of Physicists in Medicine Annual Meeting 2014* Austin, Texas, US
Jul 2014	Dynamic keyhole MRI reconstruction for real-time tumor motion monitoring *American Association of Physicists in Medicine Annual Meeting 2014*

	Austin, Texas, US
Dec 2013	The effect of audiovisual feedback for respiratory-gated 4D MRI *Australasian College of Physical Scientists & Engineers in Medicine 2013* The University of Sydney, Australia
Nov 2013	Respiratory motion based dynamic keyhole reconstruction for real-time thoracic MRI *Sydney University Postgraduate Cancer Research Symposium 2013* The University of Sydney, Australia
May 2013	Audiovisual biofeedback improves image quality and reduces scan time for respiratory-gated 3D MRI *International Conference on the Use of Computers in Radiation Therapy 2013* Melbourne, Australia
May 2013	Audiovisual biofeedback improves image quality and reduces scan time for respiratory-gated 3D MRI *International Society for Magnetic Resonance in Medicine Annual Meeting 2013* Salt Lake City, Utah, US
Dec 2013	Effect of audiovisual biofeedback on respiratory-gated 3D thoracic MRI *Australasian College of Physical Scientists & Engineers in Medicine 2012* The University of Sydney, Australia

Jul 2012	Respiratory-Related External/internal Motion Based MR Image Reconstruction Using Dynamic Keyhole for Real-Time Tumor Monitoring *American Association of Physicists in Medicine Annual Meeting 2012*, Charlotte, NC, US

List of Abbreviations

2D	Two Dimensional
3D	Three Dimensional
4D	Four Dimensional
4DCT	Four Dimensional Computed Tomography
AP	Anterior-Posterior
AV	Audiovisual biofeedback
AVBH	AV Breath-Hold
BH	Breath-Hold
CBH	Conventional Breath-Hold
CRT	Conformal Radiotherapy
CT	Compute Tomography
DNA	Deoxyribonucleic Acid
EBRT	External Beam Radiotherapy
EE	End Exhalation
EI	End Inhalation
FB	Free Breathing
FT	Fourier Transform
FFT	Fast Fourier Transform
FOV	Field of View
GRE	Gradient Recalled Echo sequence
GTV	Gross Tumour Volume
IGRT	Image Guided Radiation Therapy
LINAC	Linear Accelerator

LR	Left-Right
MLC	Multileaf Collimator
MRI	Magnetic Resonance Imaging
MRIgRT	MRI-guided Radiation Therapy
NMR	Nuclear Magnetic Resonance
NSCLC	Non–Small Cell Lung Cancer
NTCP	Normal Tissue Complication Probability
OBI	On-Board Imager
PET	Positron Emission Tomography
RF	Radio Frequency
RMS	Root Mean Square
RMSE	Root Mean Square Error
RPM	Real-time Position Management system
SE	Spin Echo
SI	Superior-Inferior
SNR	Signal-to-noise Ratio
SPECT	Single-Photon Emission Computerized Tomography
STD	Standard Deviation
TCP	Tumour Control Probability
TNM	Tumour Node Metastasis
TPS	Treatment Planning System
U.S.	United States
US	Ultrasound

Symbols

%	Per cent
γ	Gyromagnetic ratio
B_0	Main static magnetic field
B_1	Circularly polarized magnetic field
cm	Centimetre
Hz	Hertz
mm	Millimetre
ms	Millisecond
mSv	Millisievert
s	Second
T	Tesla
T1	Longitudinal relaxation time constant
T2	Transverse relaxation time constant
TE	Echo time
TR	Repetition time

Chapter 1: Introduction to Thesis

In the field of external beam radiotherapy (EBRT), an external ionizing radiation beam is directed at the target (tumour) from multiple angles, overlapping or intersecting a certain region for the delivery of radiation dose to the target whilst only slightly irradiating the healthy tissue between the beam and the target. Hence, accurate radiation delivery is important in order to maximize the delivery to the target and minimize the radiation toxicity to the healthy tissue during EBRT. However, tumours move considerably, leading to tumour motion uncertainty and resulting in mis-targeting and collateral damage to healthy tissues and critical organs. In the case of lung cancer patients, the effect can be more severe due to tumour motion variations from breath-to-breath (intra-fraction) and fraction-to-fraction (inter-fraction), compromising the quality of treatment. To determine the tumour motion uncertainty more precisely, two cutting-edge techniques are investigated in this thesis: (1) fast tumour imaging and (2) tumour motion management. Fast tumour imaging without motion artefacts can provide a better definition of tumour position and volume, and tumour motion management can improve the reproducibility of tumour motion through the course of radiotherapy.

In this study our team invented the concept of, and developed the Dynamic Keyhole method, a novel method to improve MR images in the presence of respiratory motion for real-time MRI. We believe this approach could improve real-time MR and provide accurate estimation of tumour motion, position and volume for image guided radiotherapy (IGRT). In addition, we employed audiovisual (AV) biofeedback, an interactive and personalized breathing guidance system to improve intra- and inter-fractional breathing reproducibility. These novel techniques have a wide range of applications in medical imaging, treatment planning and treatment delivery. Dynamic keyhole and AV biofeedback provide the ability to monitor and localize lung tumours in real-time. In addition, they improve lung tumour definition in cine-MRI, breath-hold MRI and respiratory-gated MRI.

The first study of the dynamic keyhole method was a reconstruction simulation of sixty cine-MRI datasets acquired from fifteen healthy volunteers. This study demonstrated that the dynamic keyhole method achieved 79% faster acquisition speed compared with the conventional approach and is promising for real-time imaging applications. Further work is needed to evaluate the dynamic keyhole method with datasets from lung cancer patients. This study resulted in a publication in *Medical Physics*.

To evaluate the accuracy of tumour motion and area, tumour motion and area were quantified as a function of acceleration factor for the dynamic keyhole method. Sixty four cine-MRI datasets from nine lung cancer patients were used in a reconstruction simulation. Compared to the ground truth, the dynamic keyhole method achieved an average accuracy in tumour motion of 99.6% and average accuracy in tumour area of 98.0%, make it promising for real-time lung tumour monitoring applications. This study resulted in a publication in *Medical Physics*.

AV biofeedback was employed for cine-MRI for lung tumour motion consistency. A breathing training session prior to two 3T MRI scans was performed to allow patients to become familiar with AV biofeedback. A guiding wave customized for each patient based on a reference breathing pattern was utilized across two MRI sessions. Compared to free breathing (FB), AV biofeedback improved intra and inter-fraction tumour motion consistency by 34% and 42% in displacement and by 73% and 74% in period, respectively. This demonstrated that AV biofeedback significantly improved intra- and inter-fraction lung tumour motion consistency for lung cancer patients. This study resulted in a publication in *Int J Radiat Oncol Biol Phys*.

AV biofeedback was employed for breath-hold MRI for lung tumour position reproducibility and volume consistency. A breath-hold training session was performed to allow patients to become comfortable with AV biofeedback breath-hold (AVBH). Exhale and inhale breath-hold positions were utilized for individual patients across two MRI sessions. Compared to conventional breath-hold (CBH) utilizing audio-instruction on the MRI scanner, AVBH improved the reproducibility of inter-fraction tumour position by 46% and the consistency of intra-fraction tumour volume by 70% in breath-hold MRI. This study demonstrated that AVBH can improve the reproducibility of breath-hold lung tumour position and volume for emerging respiratory-gated lung cancer radiotherapy methods. This study resulted in a submission to *Radiotherapy and Oncology*.

AV biofeedback was employed for respiratory-gated MRI for scan time reduction and image quality improvement. The inhale and exhale 3D images of respiratory-gated MRI showed more anatomic information such as a clear distinction of diaphragm, lung lobes and sharper organ boundaries. Simultaneously, the scan time was reduced using AV biofeedback compared to FB. This study demonstrated the improvement in image quality and a reduction in scan time for respiratory-gated 3D MRI. This study resulted in a publication in *Journal of Physics: Conference Series*.

In order to utilize the superior soft-tissue contrast of magnetic resonance imaging (MRI) for improving treatment outcome, radiation therapy systems integrated with MRI have been proposed for MRI guided radiation therapy (MRIgRT) such as the Viewray system, which is currently available for MRI guidance in clinical practice. The dynamic keyhole method can reduce the imaging time of MRI for real-time tumour monitoring. In addition, AV biofeedback can improve the reproducibility of lung tumour motion, position and volume through the course of radiation procedures. These techniques can be utilized in treatments of tumours subjected to respiratory motion to precise the delivery of radiation more to tumours and less to surrounding healthy tissues.

The structure of this thesis is as follows. Chapter 2: Literature Review introduces the workflow of lung cancer radiation therapy, discusses the techniques of treating mobile tumours, and provides additional techniques and justification for this research. Chapter 3: Dynamic keyhole: A novel method to improve MR images in the presence of respiratory motion for real-time MRI introduces the crucial works of the proposition and concept of the dynamic keyhole method. This includes the reconstructions of MR images from healthy volunteers. Chapter 4: Quantifying the accuracy of the tumor motion and area as a function of acceleration factor for the simulation of the dynamic keyhole magnetic resonance imaging method presents the assessment of the dynamic keyhole method by quantifying the agreement in lung tumour motion and shape on reconstructed MR images from lung cancer patients. Chapter 5: Audiovisual Biofeedback Improves Cine-Magnetic Resonance Imaging Measured Lung Tumor

Motion Consistency presents the impact of AV biofeedback on cine-MRI in terms of tumour motion consistency. Chapter 6: Audiovisual biofeedback guided breath-hold improves lung tumor position reproducibility and volume consistency presents the impact of AV biofeedback on breath-hold MRI in terms of the reproducibility in tumour position and the consistency in tumour volume quantified by the gross tumour volume (GTV). Chapter 7: Audiovisual biofeedback improves image quality and reduces scan time for respiratory-gated 3D MRI presents the impact of AV biofeedback on respiratory-gated MRI in terms of the reduction in scan time and improvement in image quality. Chapter 8: Summary and future work summarizes this thesis and discusses future work.

Chapter 2: Literature Review

Lung cancer is the 5th most common cancer leading to causes of illness and deaths in US[1] and Australia.[2] The incidence and mortality rates of lung cancer was approximately 14% and 28% in U.S. (Cancer statistics 2015), and 9.4% and 18.9% in Australia (Australian Institute of Health and Welfare 2014), respectively.[1, 2] In addition, the survival rate of lung cancer for five years was about 18% from 2004 to 2010 in U.S. whilst it was about 14% from 2007 to 2011 in Australia. Fortunately, the survival rate of lung cancer in both countries increased by 3% per year in U.S.[1] and 6% in the past two decades in Australia.[2]

EBRT is widely used for current cancer treatment. In 2012, 48.3% of all cancer patients in Australia was estimated as an indication for EBRT at least once at some time during the course of their illness.[3] However, accurate treatment of mobile tumours subjected to respiratory motion remains a challenge to be overcome for lung cancer radiotherapy.[4, 5]

This literature review addresses four main topics: (1) lung cancer radiotherapy in imaging, planning and treatment, (2) methods accounting for tumour motion, (3) magnetic resonance imaging and (4) audiovisual biofeedback. The chapter concludes with the research motivation and rationale for this thesis.

2.1 Lung cancer radiotherapy

Recent advancement in imaging during the course of radiotherapy allows radiation oncologists to have lung tumour information required for the prescription of radiation delivery though treatment planning.[6] There are three steps for precise the outcome of lung cancer radiotherapy: (1) pre-treatment imaging, (2) treatment planning and (3) treatment delivery.

2.1.1 Lung tumour imaging

During the course of radiotherapy, the imaging of dynamic targets has an important role for the detection, diagnosis and staging of the disease as well as assessing response to radiation delivery and monitoring for tumour recurrence after treatment.[7] Multiple imaging modalities such as computer tomography (CT), positron emission tomography (PET), MRI and a single-photon emission computerized tomography (SPECT) were utilized to identify lung diseases in lung tumour staging depending on tumour-node-metastasis.[7-9]

Computed tomography

Computed tomography (CT)[10] is a non-invasive medical imaging technique using X-ray equipment to obtain cross-sectional images of the body as shown in Figure 2-1. These cross-sectional images are used for various diagnostic and therapeutic intentions in the CT imaging system.

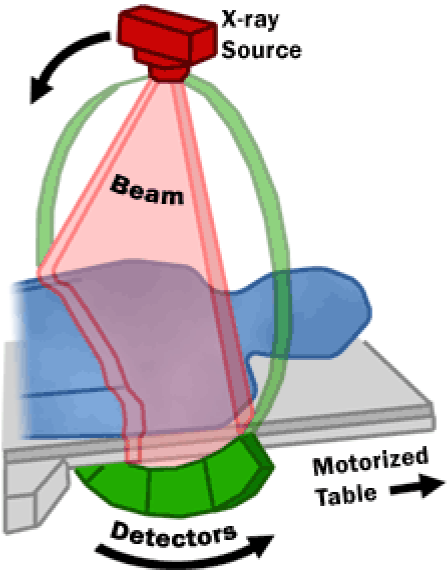

Figure 2-1. Drawing of CT fan beam and patient in a CT system. (http://www.fda.gov/Radiation-EmittingProducts/RadiationEmittingProductsandProcedures/MedicalImaging/MedicalX-Rays/, accessed on 17/09/2015).

CT system works in the five steps:

(1) A patient couch moves through a circular opening in the CT imaging system.

(2) An X-ray source (red) and detectors (green blocks) rotate around the patient. During rotation the X-ray source produces a fan-shaped beam of X-rays (pink) that passes through a cross-section of patient's body.

(3) The detectors register the X-ray at the cross-section to create an image. Many different images at correspondent angles are obtained during each full rotation (light-green circle).

(4) For each full rotation of the X-ray source and detectors, the image data are sent to image reconstruction for multiple cross-sectional images of the internal organs and tissues.

(5) Image reconstruction in CT is a mathematical process that generates images from X-ray projection data acquired at many different angles around the patient. Image reconstruction has a fundamental impact on image quality and therefore on radiation dose. For a given radiation dose it is desirable to

reconstruct images with the lowest possible noise without sacrificing image accuracy and spatial resolution.

CT images can provide detailed information of patient's body for diagnosis and treatment planning purposes, and in some cases potentially eliminating the need of exploratory surgery. However, the exposure to ionizing radiation (i.e. 7 mSv for CT chest and 1.5 mSv for lung cancer screening) during CT imaging introduces risks of possible secondary cancers.[11, 12]

Positron Emission Tomography

Positron emission tomography (PET)[7, 13-15] is a non-invasive medical imaging technique using a positron-emitting radioactive material to obtain 2D and 3D images of the body as shown in Figure 2-2.

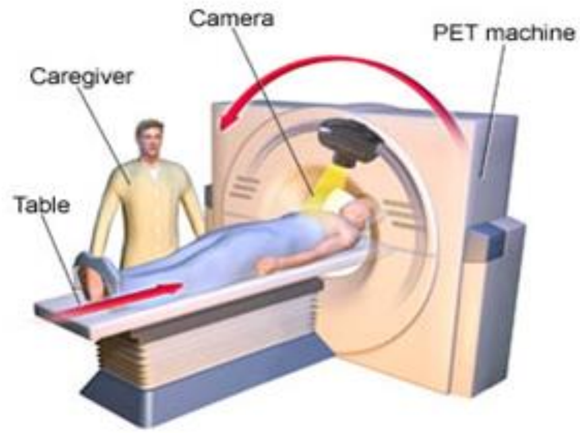

Figure 2-2. Drawing of PET camera and patient in a PET system. (http://www.iambiomed.com/equipments/pet.php, accessed on 17/09/2015).

PET system works in the five steps:

(1) A small amount of a positron-emitting radioactive material (i.e. fluorodeoxyglucose (FDG)) is injected.

(2) Patients rest for an appropriate amount of time. Cancerous cells use glucose (a type of sugar) at a much faster rate than normal cells.

(3) A PET scanner obtains body images for 15 – 35 minutes whilst detecting emissions from the FDG by the camera surrounding a patient at the area being examined to identify the cancerous cells.

(4) PET 2D and 3D images are reconstructed by the computer attached to the camera.

(5) Image reconstruction in PET is to provide cross-sectional images of the radiotracer distribution in an object, using the coincidence events detected by a scanner. In 2D imaging, the data are only collected in direct and cross planes. A direct plane is perpendicular to the scanner axis, and a cross plane connects detector elements in two adjacent detector rings. 2D images are reconstructed on each of the planes, and are stacked to form an entire image volume together (3D).

PET images can provide changes in the metabolism of organs and tissues. Many cancers are newly detected using PET imaging. PET scans can also acquire the whole body, which is beneficial to the diagnosis or detection of cancers spreading to other areas. In addition, PET can be used to distinguish an active tumour from scar tissues. Substantial radiation dose and cancer risk should be carefully considered during whole-body PET imaging.[16]

Magnetic resonance imaging

Magnetic resonance imaging (MRI) utilizes strong magnetic fields and radio frequency waves to produce cross-sectional images of organs and internal structures as shown in Figure 2-3. An MRI machine detects varying signals depending on the materials with water content affected by the magnetic fields at the cross-sectional area of the body.

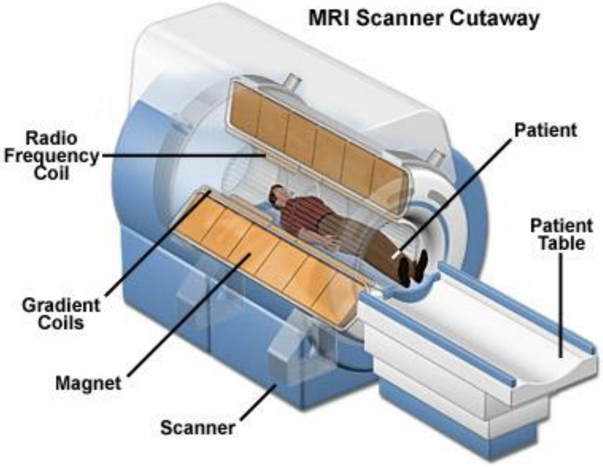

Figure 2-3. Drawing of the cutaway and patient in an MRI scanner. (http://www.cyberphysics.co.uk/topics/medical/MRI.htm, accessed on 22/09/2015).

MRI system works in three steps:

(1) An electric current is passed through coiled wires to create a temporary magnetic field around a patient's body. A magnetic field gradient is a variation in the magnetic field with respect to position.

(2) Radio frequency waves are sent from a transmitter and received by a receiver in the machine. Slice selection is achieved by applying a one-dimensional, linear magnetic field gradient during the period that the RF pulse is applied.

(3) These signals are used to produce digital images of the area of interest. The amplitude of the signal is proportional to the number of spins in a plane perpendicular to the gradient. This procedure causes the resonant frequency to be proportional to the position of the spin.

MRI does not use ionizing radiation, i.e. high-energy radiation that can potentially cause damage to deoxyribonucleic acid (DNA) such as x-rays used in CT scans. There are no known harmful side-effects associated with temporary exposure to the strong magnetic field used in MRI. As MRI forms a core part of the work in this thesis, more details on MRI can be found in the section 2.3 Magnetic resonance imaging.

Single-Photon Emission Computerized Tomography

Single Photon Emission Computed Tomography (SPECT) can show blood flows of tissues and organs through a type of nuclear imaging as shown in Figure 2-4. A SPECT scan combines CT with a radioactive material (tracer) to view blood flows in body. The tracer allows doctors to see the blood flows to tissues and organs.

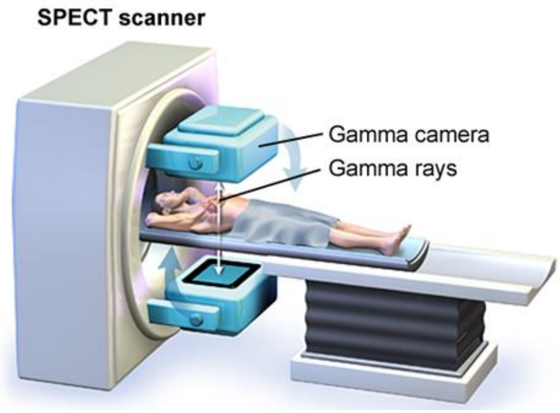

Figure 2-4. Drawing of the camera and patient in a SPECT scanner. (http://medmovie.com/library_id/3255/topic/ahaw_0224i/, accessed on 22/09/2015).

SPECT system works in five steps:

(1) A chemical radiolabeled for emitting gamma rays is injected to be detected by the scanner. The emission of the gamma rays is translated into two-dimensional cross-sections.

(2) The radioisotopes are used in SPECT to label tracers and pass safely through blood flows detected by the scanner.

(3) The type of tracers can be dependent on measurement. Radiolabeled glucose (FDG) is used to detect metabolized tumour.

(4) The tracer stays in blood stream, thereby limiting the images to areas where blood flows.

(5) Image reconstruction in SPECT is performed by using a gamma camera to acquire multiple projections (2D) from multiple angles. A computer is then used to apply a tomographic reconstruction algorithm to the multiple projections for an entire image volume (3D).

SPECT scans are safe for most patients but they may experience: (1) bleeding, pain or swelling where the needle was inserted in their arm and (2) rarely, an allergic reaction to the radioactive tracer.

Pre-treatment lung tumour imaging

Lung tumours move due to breathing. To ensure that the treatment plan encompasses the motion range of the tumour, patient images with motion information are required. Four-dimensional (4D) images (i.e. moving 3D images) can be utilized to quantify internal anatomy information as a function of the respiratory cycle.[17] Prior to treatment planning, a number of imaging simulations using CT, PET, SPECT and

MRI are performed to characterize the 4D motion of tumour and healthy tissue.[6].[13, 18, 19]

2.1.2 Treatment planning

EBRT delivers high radiation doses from outside the body to the target cancer. This is the type of radiotherapy most frequently used to treat a primary lung cancer or other organs. However, radiation affects both healthy tissues and lung tumours.[20]

The first step of treatment planning of conformal radiotherapy (CRT), intensity modulated radiotherapy (IMRT) and volumetric modulated arc radiotherapy (VMAT) is the definition of the anatomy of the lung tumour, contouring the gross tumour volume (GTV), clinical target volume (CTV), internal gross target volume (IGTV), internal target volume (ITV), planning target volume (PTV) and critical structures using report 50 and 62 of international commission on radiation units and measurements (ICRU).[21, 22]

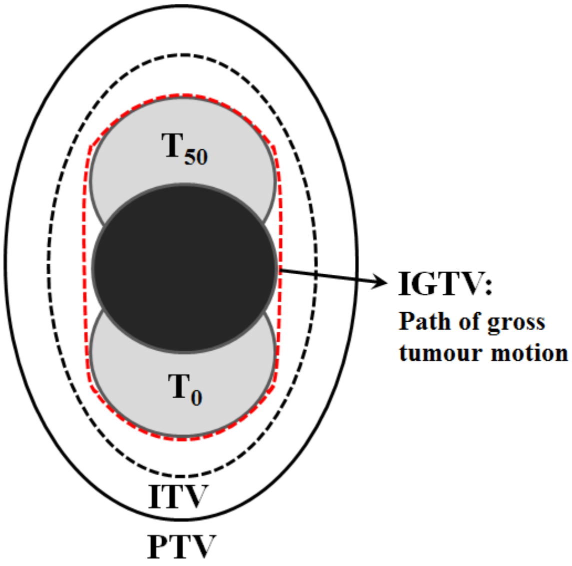

Figure 2-5. Lung tumour delineation. IGTV, internal gross tumour volume; T_0, at the end of inspiration; T_{50}, at the end of expiration; internal target volume (ITV); planning target volume (PTV). (http://www.sps.ch/artikel/progresses/modern-techniques-in-radiation-oncology-36/).

As shown in Figure 2-5, radiation oncologists define the volume of primary tumour by delineating GTV on 4D-CT images. An IGTV is anatomically defined using the area of encompassing GTVs. Geometrical volumes of ITV and PTV are usually extended around the GTV to compensate for positioning uncertainty of lung. In addition, normal structures required for the treatment planning are delineated on the 4D-CT images.[23]

Treatment planning in radiotherapy involves the following steps.

(1) The information of the area of the body to be treated is obtained through a CT scan. The images of the CT scan feed directly into the treatment planning system (TPS).

(2) The computer program models radiation beams for radiation delivery. The motion and shape of lung tumour are encompassed by the targeted region and

dose to healthy tissues is minimised as much as possible in order to reduce the risk of side effects.

A lung cancer treatment plan includes the information of tumour motion, shape and volume from the contoured 4D-CT images which are 3D-CT images typically acquired with ten respiratory phases. Encompassing lung tumour motion and volume contoured by deformable registration are utilized for 4D treatment plan, allowing precise radiation delivery.

2.1.3 Treatment delivery

Radiotherapy is a highly targeted cancer treatment, leading to technological innovations enabling the integration of imaging technology to increase the precision and accuracy of treatment delivery.[24] There are a number of radiotherapy techniques.

3D conformal radiation therapy

Three-dimensional (3D) conformal radiotherapy (CRT) uses a specialised planning CT scan and sometimes other scans, such as PET and MRI scans. This allows treatment planning in 3 dimensions of width, height and depth. After the planning session patients usually have an appointment for the first fraction within a few days or few weeks. Using radiographs and markers (skin and fiducial, and bony structures), the centroid of the lung tumour is aligned with the treatment isocenter.

Intensity modulated radiation therapy

Intensity modulated radiotherapy (IMRT) is a type of conformal radiotherapy. Conformal radiotherapy shapes external radiation beams to form the shape of lung tumour using a multileaf collimator (MLC) which is an important tool for radiation therapy dose delivery as shown in Figure 2-6.[18, 25]

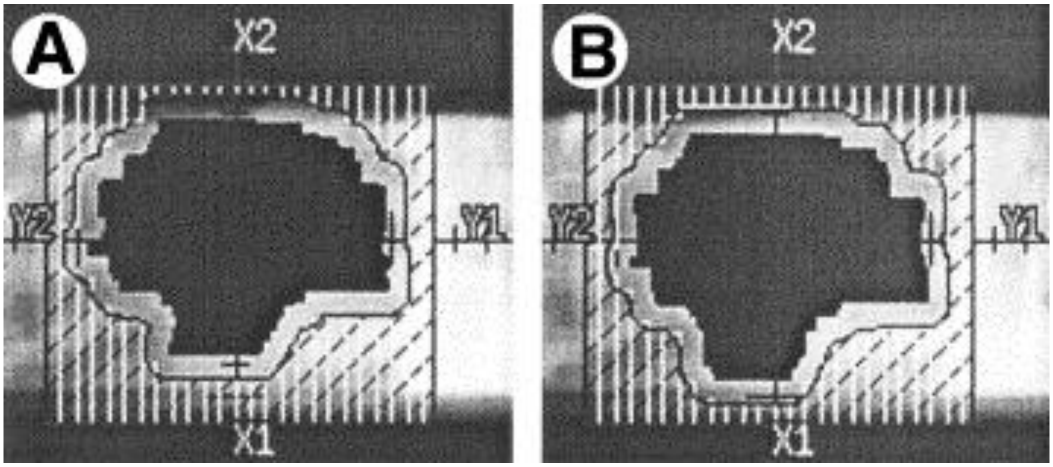

Figure 2-6. Posterior beam views corresponding to PTV shapes of (A) exhale and (B) inhale. [Image credit: Keall *et al.*[20]]

The MLC placed at the end of a linear accelerator (Linac) is utilized for IMRT. The MLC is made up of thin leaves which can move individually so the leaves can form the beam shapes that conform to the lung tumour. The MLC shapes the radiation beam to the projection of the tumour shape at each gantry angle as the machine rotates. The result is the lung tumour receiving an intended high dose and surrounding normal healthy tissues receiving a minimal dose. Each radiotherapy beam is divided into many small beamlets, allowing different radiation doses across lung tumour. IMRT avoids high radiation doses to structures that would be damaged by the radiotherapy. IMRT can reduce the radiation toxicity of the normal healthy tissue, resulted in the minimization of the risk of long term side effects.

Volumetric modulated arc therapy

During volumetric modulated arc therapy (VMAT) treatment,[26] the radiation machine rotates around the patient in single or a series of arcs delivering many small beamlets to the cancer. The shape and intensity of the radiation beams are continuously changed as the machine rotates. In other words, the beam of radiation can come from an infinite number of angles, thereby reducing the dose of radiation to normal tissue whilst increasing the dose to lung tumour. In addition, VMAT allows radiation delivery at adjacent angles to critical structures in the body.

2.2 Methods to account for tumour motion

The tumour motion of thoracic and abdominal regions affected by breathing varies both intra and inter-fractionally.[5, 27] Examples of intra and inter-fraction tumour motion variations are shown as shown in Figure 2-7.[5]

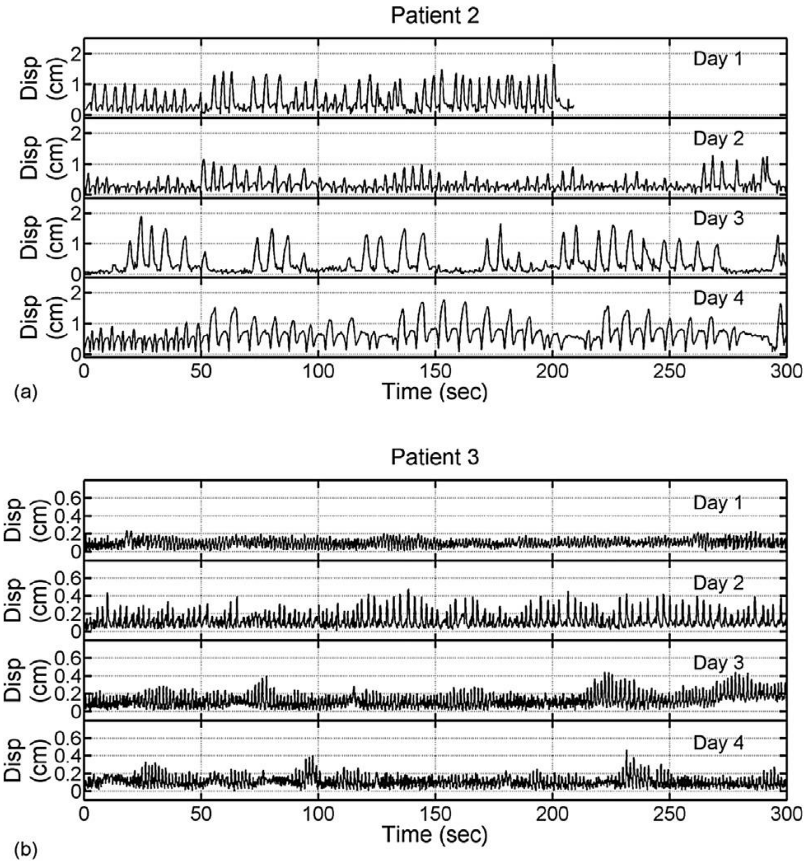

Figure 2-7. Breath-to-breath and day-to-day variations of lung tumour motions (3-dimensional displacement) for 4 consecutive treatment days shown in (a) and (b), respectively. Data truncated to first 300 seconds per tracking session. [Image credit: Shah *et al.*[5]]

Intra-fraction (breath-to-breath) variation in motion can cause image artefacts in 4D-CT images utilized in treatment planning.[17, 28] This can also lead to blurring in the dose distribution along the path of the tumour motion.[29, 30] An example of four common image artefacts in 4D-CT is shown in Figure 2-8.[28]

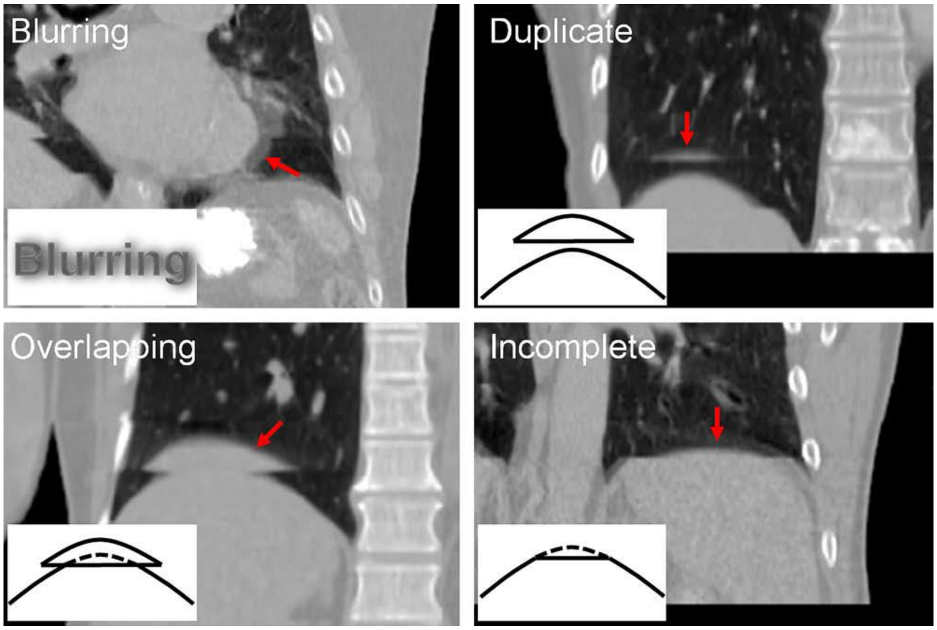

Figure 2-8. Example 4D-CT images with schematic diagrams for the four types of artefacts: blurring, duplicate structure, overlapping structure, and incomplete structure. Corresponding artefacts are indicated by arrows in respective images. Note that other artefacts can also be observed in these images. [Image credit: Yamamoto *et al.*[28]]

Inter-fraction (day-to-day) variation in motion can cause a greater discrepancy in tumour motion between treatment planning and delivery, and a shift to the dose distribution.[5, 31, 32] Tumour growth and shrinkage resulting in the change in tumour motion, position and volume can also be expected throughout the course of radiotherapy.[33, 34]

In order to improve the quality of medical imaging and the outcome of radiotherapy, tumour tracking and motion management in the presence of respiratory motion are required to compensate temporal anatomic changes and increase motion consistency, respectively. This renders more accurate estimates of the tumour position and area, thus improving the accuracy of the treatment.

2.2.1 Real-time position monitoring and adaptation

In order to account for tumour motion in terms of systematic and random errors,[5, 31, 32] the current standard care of radiotherapy adds margins to CTV, resulting in the irradiation of a PTV volume larger than necessary.[21, 22] This causes more healthy tissue to be exposed to radiation and increases the normal tissue complication probability (NTCP). In addition, irregular tumour motion could cause the beam to miss resulting in a lower tumour control probability (TCP). One solution is real-time position monitoring before and during treatment and the subsequent adaptation of treatment to dynamic tumour position.

Real-time position monitoring

Real-time position monitoring techniques[32, 35-38] allow target positions (i.e. implanted markers, surrogates or target tumours) to be determined for hypofractionated radiation therapy in which the total dose of radiation is divided into large doses over fewer fractions. IGRT techniques have evolved from localising target positions for planning, pre- and post-treatment and occasional imaging during treatment to high-frequency position monitoring of intra-fraction motion.

The Calypso 4D Localization System utilizes electromagnetic technology combined with implanted electromagnetic transponders (beacon) as shown in Figure 2-9.

Figure 2-9. Calypso (right) 4D Localization System and Beacon (left circle) electromagnetic transponder. (http://mms.businesswire.com/bwapps/mediaserver/ViewMedia?mgid=102545&vid=5&download=1, accessed on 6/10/2015)

This is designed to continuously monitor beacon position corresponding to the tumour position, which can provide greater confidence to real-time tumour tracking during radiation delivery. In addition, imaging dose from X-ray for tumour monitoring is excluded due to the use of Calypso.[5, 36]

The Varian On-Board Imager (OBI) kV imaging system provides an image of high resolution using low dose digital imaging system and this is more efficient and convenient for IGRT (see Figure 2-10, a kV beam (left) and imager (right) on horizontals). The kV imager enables the user to quickly acquire high quality online images to identify the differences in patient and tumour (or implanted marker) positions between treatment planning and treatment delivery, and correct those differences before or during treatments.[39]

Electronic portal imaging using an MV imager is a modality available on most present linear accelerators (see Figure 2-10, an MV beam (top) and imager (bottom) on verticals). The MV imager is placed in-line with the MV beam direction on the opposite side of the patient and measures the MV beam transmission through the patient. MV images have been employed for tracking techniques in pre-clinical and clinical trials.[40-42]

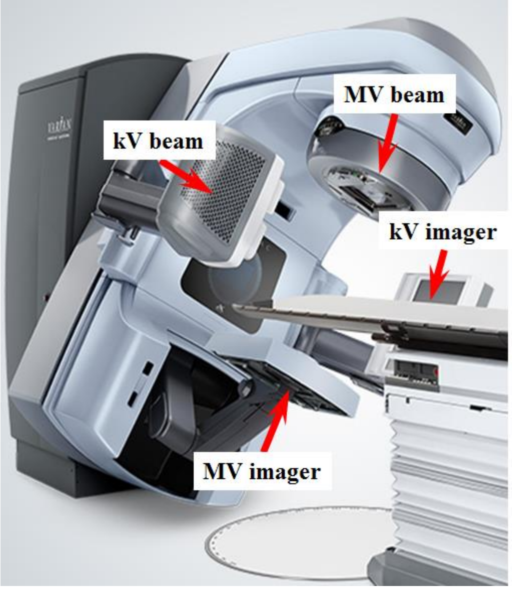

Figure 2-10. The Varian On-Board kV and MV imagers. A kV beam (left) and imager (right) and an MV beam (top) and imager (bottom) are placed in the orthogonal plane. (https://www.varian.com/oncology/products/treatment-delivery/clinac-ix, accessed on 6/10/2015).

An integrated MRI-guided radiation therapy (RT) system provides simultaneous MR imaging and radiation delivery. The MRI and radiotherapy systems share an identical isocentre, enabling simultaneous and continuous MR image acquisition and radiation delivery, and leading to on-couch adaptive and MRI-controlled IMRT at the identical isocentre.[43] The ViewRay System (see Figure 2-11(a))[44] is the first commercially available MRI–guided radiotherapy system and consists of a split 0.35T MRI with 3×^{60}Co heads mounted on a ring gantry, each head equipped with independent doubly focused multi-leaf collimators. The Utrecht System (see Figure 2-11(b))[45] consists of a fully integrated 1.5T, diagnostic quality, MRI with a 6-MV linear accelerator. The Alberta System (see Figure 2-11(c))[46] consists of 0.6T MRI with 6-MV linear accelerator. The Australian MRI-Linac System (see Figure 2-11(d))[47] consists of 1.0T open-bore MRI with 6-MV linear accelerator.

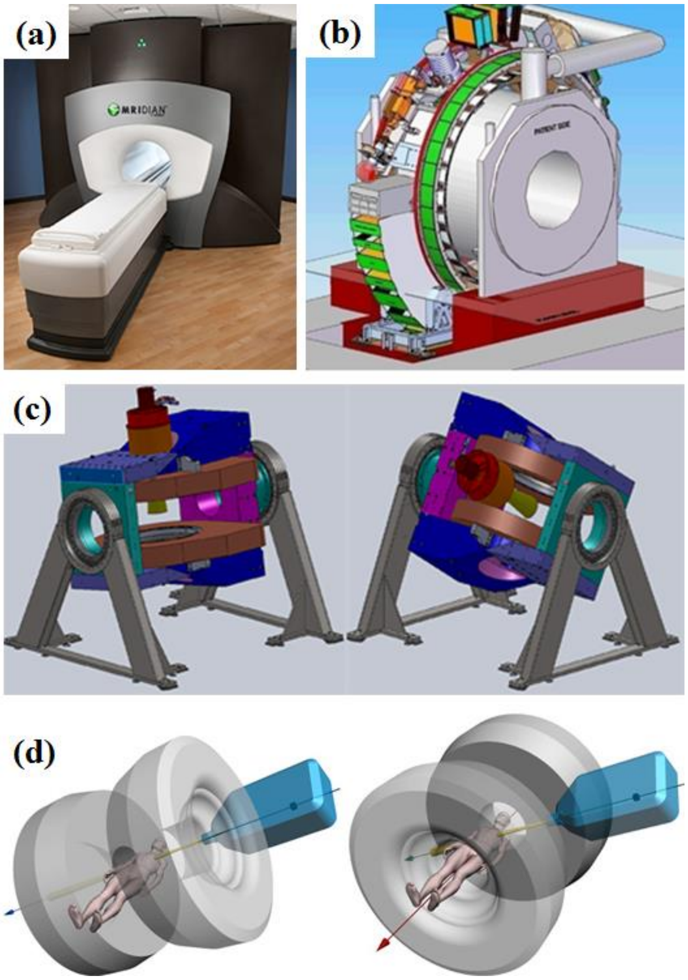

Figure 2-11. MRI combined with radiation therapy systems. (a) ViewRay System (US), (b) Utrecht (The Netherlands), (c) Alberta (Canada) and (d) Australian MRI-Linac (Australia).

Real-time adaptation

Real-time tumour position monitoring can be sued to achieve the real-time beam adaptation which corrects the difference between the tumour position at planning and the latest determined tumour position. Real-time position monitoring and real-time adaptation work in four steps:

(1) The tumour motion is detected by monitoring real-time tumour position.

(2) A correction is made for the reaction time comprising the latency of real-time position monitoring and the delay in real-time adaptation.

(3) The treatment is adjusted by real-time adaptation.

(4) During treatment, the treatment unit irradiates a moving target with planned radiation beams.

Real-time adaptation utilizes two types of loop control: (1) closed-loop and (2) open-loop. A closed-loop control known as a feedback control is a control system which includes one or more feedback loops: some portion of the output is returned back to the input to form part of the system excitation (i.e. treatment adaptation causes the target to move). Examples are real-time couch tracking and couch gating.[48, 49]

The couch for tracking is continuously moved based on real-time tumour motion during treatment. The couch for gating is only moved when a certain motion threshold is exceeded.

Figure 2-12. The Hexapod, a 6 degree of freedom motion correction couch. [Image credit: Krilavicius *et al.*[48]]

An open-loop control system does not include a feedback loop (i.e. treatment adaptation does not cause the target to move). Examples are MLC tracking[20] and Cyberknife (a robotic radio-surgery system).[50] To compensate the latency between detecting tumour positions and adapting the latest tumour position, one solution is to utilize prediction algorithms for tumour motion. The other is just to reduce the latency to an acceptable timescale much smaller than the motion timescale of the tumour.

MLC tracking (see Figure 2-6) is available on most modern linacs to shape and modulate the beam based on real-time adaptation. One advantage of MLC is that highly conformal shapes can be made due to the large number of MLC leaves. MLC tracking has been clinically demonstrated with Calypso (see Figure 2-9) as the input of real-time tumour position.[36]

Cyberknife is utilized for treating various tumours such as brain, spine, pancreas, lung, liver and prostate. It is comprised of a compact linear accelerator and a computer-controlled arm as shown in Figure 2-13.

Figure 2-13. A compact linear accelerator, a computer-controlled arm and patient in a Cyberknife system. (http://www.garber-online.com/cyberknife.htm, accessed on 6/10/2015).

Multiple radiation beams are delivered from many different angles whilst considering tumour motion to adjust a high dose of radiation delivery to the target tumours. Four fiducial markers are utilized to represent the position and movement of the target tumours during Cyberknife treatment.[50]

2.2.2 Tumour motion management techniques

Breathing management techniques can be utilized to guide and hold respiratory-induced tumour motion by measuring air volume, compressing the abdomen and guiding respiratory motion using internal and external respiratory signals. These techniques can reduce respiratory motion artefacts in medical imaging and improve tumour motion and position reproducibility in respiratory gating,[51] training[52] and breath-hold[53] for lung cancer patients.

Active Breathing Coordinator (ABC) system

Active breathing coordinator (ABC) as a respiratory motion management technique provides non-invasive, internal immobilization of lung and abdominal anatomies affected by respiratory motion. This is achieved through comfortable, simple and efficient involuntary breath-hold.[54] ABC as shown in Figure 2-14 is widely used for the clinical treatment of lung and liver cancers to hold target anatomy motion static through imaging, planning and delivery for stereotactic body radiotherapy (SBRT) due to the reduction of dose to OARs and efficiencies in automated gating and workflow.

Figure 2-14. Active breathing coordinator (ABC) constructed 2 pairs of flow monitor and scissor valve, each to control the inspiration and expiration paths to the patient. (https://www.elekta.com/radiotherapy/treatment-solutions/motion-management.html, accessed on 6/10/2015).

The patient breathes through a mouth-piece connected to the ABC apparatus. The respiratory signal is continuously processed and displays the change of lung volume in real-time on a personal computer. The radiographer activates ABC at a pre-determined phase in the respiratory cycle corresponding to the change of lung volume. Both valves are then closed to hold respiratory motion.

Abdominal Compression

The use of abdominal compression system as a SBRT solution with a belt or pressuring system can provide the reproducibility and immobilization needed for high dose and high precision treatments as shown in Figure 2-15.[55-57] The compression system consists of a base plate made of glass fiber for a low density and transparent material, and a compression arch (or belt) connected to the base plate fitted on couch tops.

Figure 2-15. Abdominal compression system using a base plate and a compression arch. (http://www.orfit.com/en/stereotactic-body-radiation-therapy-sbrt/, accessed on 6/10/2015).

Breath-hold (BH) and deep inspiration breath-hold (DIBH)

Breath-hold (BH)[58-60] can hold mobile tumours, minimizing the phase shift of the mobile tumours[61] and system latency between tumour positioning and radiation delivery.[44] In addition, deep inspiration breath-hold (DIBH),[62, 63] which involves the patient holding a deep breath during radiation delivery, can minimize radiation exposure to the heart, decreasing the risk of developing heart disease as a long-time side effect.[64] By performing the DIBH, the heart naturally moves away from the breast (i.e. women receive radiation for breast cancer) and out of the radiation beam path.

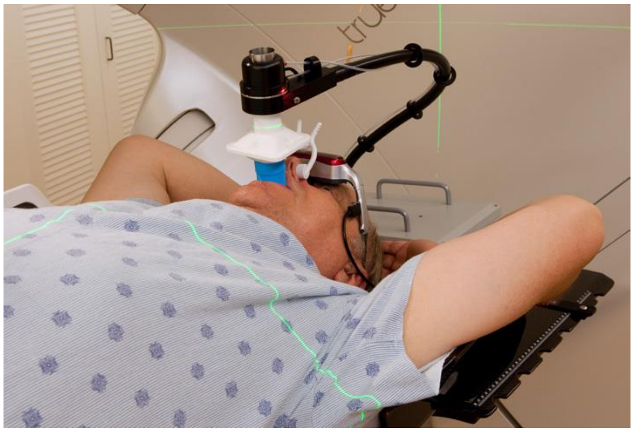

Figure 2-16. Spirometric Motion Management System with DIBH for managing thoracic and abdominal tumour motion. (http://www.oncologyimaging.com/SDX.asp, accessed on 6/10/2015).

DIBH consists of a modified slow vital capacity (SVC) maneuver followed by a deep inspiration breath-hold. The SVC maneuver consists of at least three normal (free) breaths followed by deeper inspiration and expiration prior to the maximum deep inspiration breath-hold.[62]

2.3 Magnetic resonance imaging

Magnetic resonance imaging (MRI) is an imaging modality used to produce high contrast images of internal human body. MRI was first proposed as a tomographic imaging technique to obtain microscopic chemical and physical signals about molecules using a spectroscopic technique based on nuclear magnetic resonance (NMR). MRI can also produce an image of the signals in a thin selection (i.e. slice) through the human body and a volume of target regions.

2.3.1 Imaging principles

MRI measures spatial variations of NMR signals in the phase and frequency of the radio frequency energy being absorbed and emitted by in an object and constructs images of the object.

Basic imaging principles

The principle of MRI is based on the resonance equation, which shows that the resonance frequency ν of a spin is proportional to the magnetic field it is experiencing, B_0:

$$\nu = \gamma B_0$$

A particle with a net spin, placed in a magnetic field of strength B_0 can absorb a photon of frequency (ν). The frequency depends on the gyromagnetic ratio (γ) of the particle. For example, the gyromagnetic ratio of hydrogen is equal to 42.58 MHz/T and thus the resonant frequency for protons in a 1.5 tesla scanner is 63 MHz.

MR imaging processes are comprised of four steps:

(1) Slice selection: This is the selection of spins in an imaging plane of the human body using the radio frequency (RF) of the pulse of any angles (i.e. a rotation angle of between 0 and 90°). This leads to rotate spins in a slice selection and plane through the human body.

(2) Magnetic field gradient (G): The resonance equation of B_0 varies in applying linear magnetic field gradients along three directions (G_x, G_y, G_z). Spins in a slice selection then experience a unique magnetic field, enabling spatial image positions to be determined.

(3) Frequency and phase encoding: The amplitude of the NMR spectrum signal is proportional to the ratio of spins in a plane perpendicular to the gradient. This encodes the resonance frequency to be proportional to the position of the spins.

(4) Signal processing: Signals are called raw data (or *k-space* data) and used to obtain an image of the position of spins. The signals are Fourier transformed in the frequency encoding direction (i.e. Horizontal) to acquire the frequency information and the phase encoding direction (i.e. Vertical) to acquire phase information about their locations.[65, 66]

Fourier transform imaging principles

The phase encoding gradient of MR imaging is a gradient in the magnetic field B_0 and it is used to induce a specific phase angle of spins in a slice selection to a transverse magnetization vector which depends on the location of the slice selection. For example, if a gradient in B_0 is applied along the X direction, the transverse magnetization vector will move along the gradient direction applied at frequency given by the resonance frequency (ν).

$$\nu = \gamma\,(B_0 + xG_x) = \nu_0 + \gamma\, xG_x$$

Each transverse magnetization vector has a unique frequency whilst the phase encoding gradient is on. Then, each spin vector becomes identical when the X gradient is turned off. There are three distinct angles in X, Y and Z corresponding to gradients ($\mathrm{G}_x, \mathrm{G}_y, \mathrm{G}_z$) to induce the unique frequency of each transverse magnetization. Once the phase encoding gradient pulse is turned off, a frequency encoding gradient pulse (an optimal direction of phase-encoding) is turned on and a signal is recorded in the form of a free induction decay. This pulse sequence of the frequency encoding gradient is usually repeated 128 or 256 times to acquire all the data, which corresponds to the matrix size of an MR image.

The signals of free induction decays are Fourier transformed to obtain an image of spins somewhere within the space of a slice selection. The signals are Fourier transformed in the frequency encoding direction (X direction) to acquire the unique frequency of each transverse magnetization and in the phase encoding direction (Y direction) to determine the locations.

A simple Fourier transform is used to capture a single net magnetization vector located somewhere within the space in which the phase and frequency encoding gradients are applied. The relation between the signals used to fill *k-space* data and the resultant image processed raw image data is the Fourier transformation. The *k-space* is also called the spatial frequency space and it is the conjugate of the image space.

Signal intensity and image contrast

Image contrast is dependent on signal intensity difference among tissues due to the different signal relaxation time of various tissues in the body. Tissue types are identified by using T1 relaxation time (longitudinal relaxation) and molecular interactions by using T2 relaxation time (transverse relaxation).[67] The T1 and T2 constants indicate the time taken for the spinning nuclei to emit their absorbed RF energy into the surrounding tissues and spinning protons to lose phase coherence among the nuclei spinning perpendicular to the main field, respectively.

The contrast of an MR image is determined by imaging parameters (i.e. TR = repetition time, TE = echo time) selected to emphasize certain image contrast properties (weighting) in terms of T1 and T2 relaxation. Three types of weighted image contrast are shown in Figure 2-17.

(1) Proton density (PD)-weighted: PD-weighted imaging measured in short TE and long TR is used to differentiate anatomical structures based on their proton density.

(2) T1-weighted: T1-weighted imaging measured in short TE (< 40 ms) and short TR (< 750 ms) is mainly on the basis of T1 values to minimize T2 relaxation effects. Tissues with high fat content appear bright and with water appear dark.

(3) T2-weighted: T2-weighted imaging measured in long TE (> 75 ms) and long TR (> 1500 ms) is mainly on the basis of T2 values to minimize T1 relaxation effects. Tissues filled with water appear bright and with high fat content appear dark.

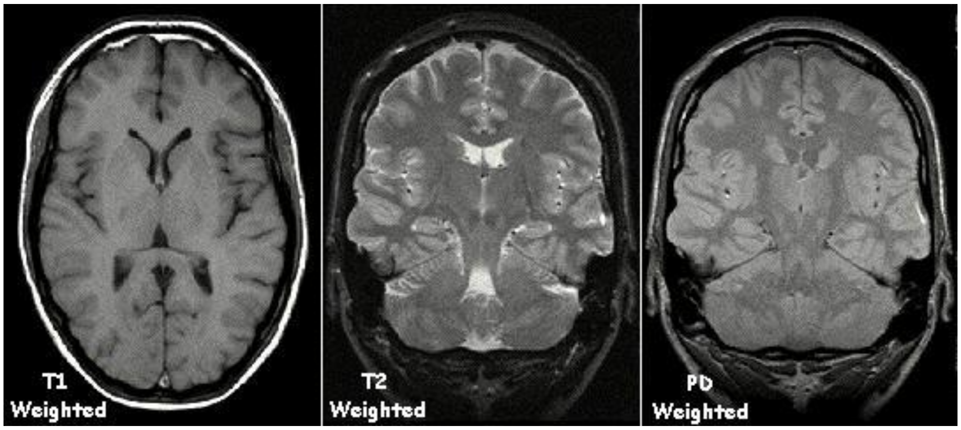

Figure 2-17. Brain images of T1-weighted, T2-weighted and PD-weighted. [Image credit: KieranMaher at English Wikibooks]

In addition, T2* (T2 star) is comprised of molecular interactions (T2) and magnetic field non-uniformities, caused by the proton precession at slightly different frequencies at various tissues. T2* effect leads to a rapid signal loss in coherence and transverse magnetization, resulting in less T2* time than T2 time. With spin echo imaging no T2* occurs, caused by the 180° refocusing pulse. For this reason, spin echo sequences are more robust against susceptibility artefacts than gradient echo sequences.

2.3.2 Basic imaging techniques

A number of imaging techniques such as gradient-echo and spin-echo have been introduced in two streams of MR imaging pulse sequences as shown in Figure 2-18.

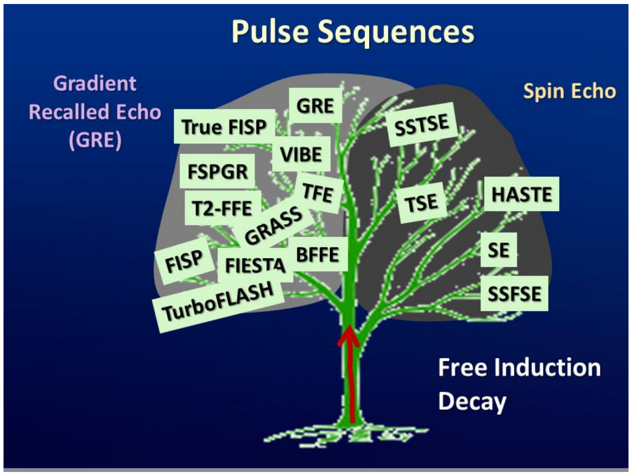

Figure 2-18. Pulse sequences in terms of MR imaging techniques: Gradient recalled echo (GRE) and spin echo (SE).
[Image credit: Kiaran P. M^{c}Gee, Mayo clinic and foundation].

Gradient echo imaging

Gradient recalled echo (GRE) sequence simultaneously utilizes a phase encoding gradient and a dephasing frequency encoding gradient to generate echoes as a consequence of echo refocusing as shown in Figure 2-19.

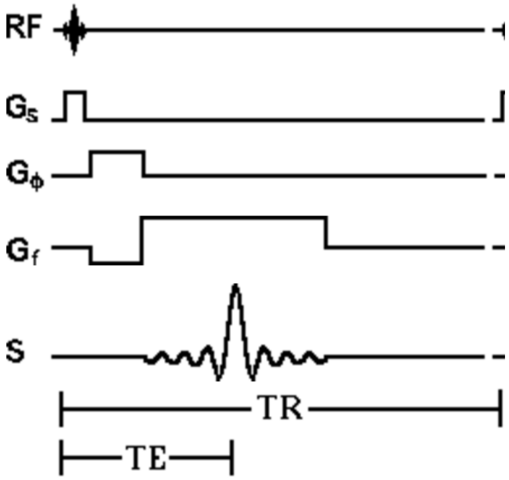

Figure 2-19. The diagram of gradient recalled echo (GRE). (https://www.cis.rit.edu/htbooks/mri/chap-8/images/ps-gr-gs.gif, accessed on 26/10/2015).

GRE imaging processes are comprised of four steps:

(1) A slice selection gradient with RF pulse is applied to the body. The RF pulse produces a rotation angle of spins between 0° and 90°.

(2) A phase encoding gradient is applied, varying between $G_{\theta m}$ and $-G_{\theta m}$ in 128 or 256 equal steps depending on the matrix size of an MR image.

(3) A dephasing frequency encoding gradient is applied at the same time as the phase encoding gradient to cause the dephasing of spins at the centre of the acquisition period. An echo of the spins is produced when the frequency encoding gradient is turned on because this gradient refocuses the dephasing which occurred from the dephasing frequency encoding gradient.

(4) A period called the echo time (TE) is defined as the time from the RF pulse to the maximum signal and it is repeated every TR seconds.

$$S = k\,\rho\left(1 - \exp\left(-\frac{\mathrm{TR}}{T_1}\right)\right)\exp\left(-\frac{TE}{T_2^*}\right)$$

Imaging with the GRE sequence is more sensitive to magnetic field inhomogeneity due to the use of the refocusing gradient.

Spin-echo imaging

Spin echo (SE), most common pulse sequence in MR imaging utilizes 180° RF pulse for echo refocusing as shown in Figure 2-20.

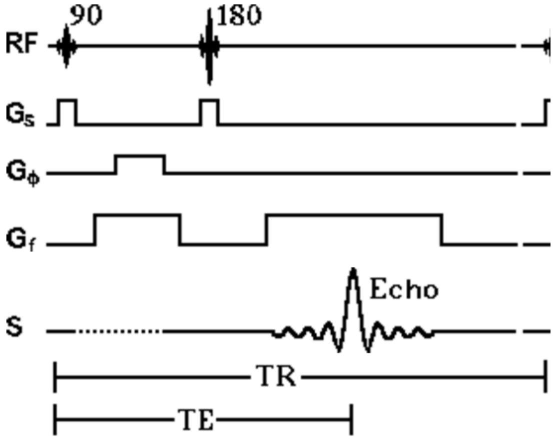

Figure 2-20. The diagram of spin echo (SE). (https://www.cis.rit.edu/htbooks/mri/chap-8/images/ps-se-gp.gif, accessed on 26/10/2015).

SE imaging processes are comprised of four steps:

(1) A slice selection using a 90º RF pulse is applied in conjunction with a slice selection gradient. A period of time equal to TE/2 elapses and a 180º slice selective 180º pulse is applied in conjunction with the slice selection gradient.

(2) A phase encoding gradient is applied between the 90º and 180º pulses, varying between $G_{\theta m}$ and $-G_{\theta m}$ in 128 or 256 equal steps. This can minimize the TE period instead of the phase encoding gradient applied after the 180º pulse.

(3) The frequency encoding gradient is applied after the 180º pulse during the time that echo is recorded as a signal. One additional frequency encoding gradient is applied between the 90º and 180º pulses along the same direction as the frequency encoding gradient, leading to dephasing the spins and resulted in rephasing the spins by the centre of the echo.

(4) The entire sequence is repeated every TR seconds until all the phase encoding steps have been recorded. The signal from a spin echo sequence is as follows.

$$S = k\,\rho\left(1 - \exp\left(-\frac{\mathrm{TR}}{T_1}\right)\right)\exp\left(-\frac{TE}{T_2}\right)$$

Imaging with the SE sequence is advantageous to T2 signals which can distinguish tissues and pathologies.

2.3.3 Temporal and spatial resolutions

Resolution is a measure of image quality dependent on field of view (FOV) and the number of data points N, across an image. The balance between temporal (i.e. the duration of time for the acquisition of a single image) and spatial (i.e. the size of image pixels or voxels) resolutions is thus a trade-off to be made for desired image capability. A number of imaging techniques use different *k-space* sampling trajectories whilst balancing the image capability between temporal and spatial resolutions.

K-space sampling trajectories

To construct an MR image, a series of *k-space* data is collected, called *acquisition*. In the acquisition, an RF excitation produces transverse magnetization along a particular trajectory in *k-space*. There are several *k-space* sampling trajectories to acquire 2D and 3D MR images as shown in Figure 2-21.[68]

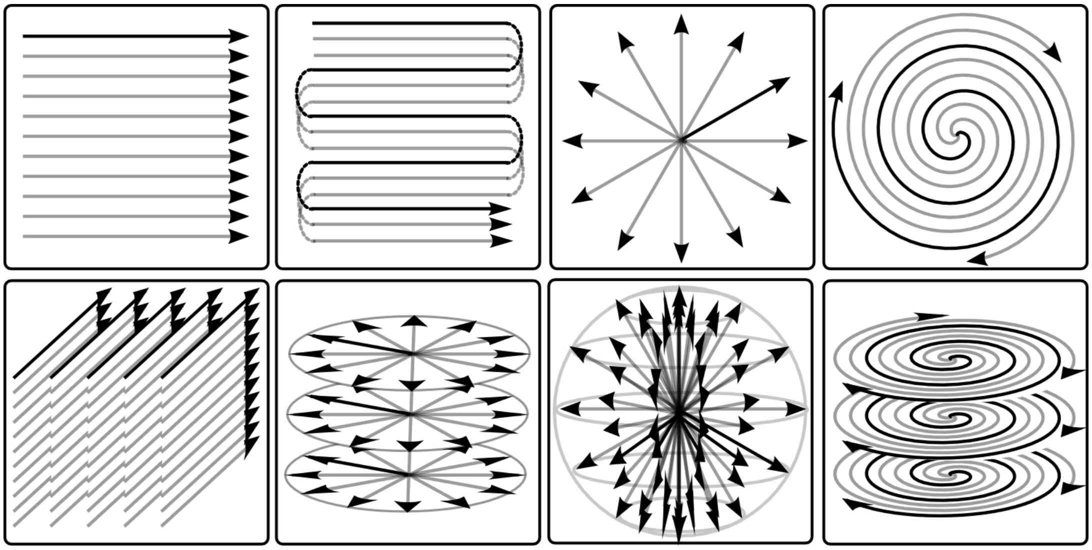

Figure 2-21. *K-space* sampling trajectories of 2D (first row) and 3D (second row) MR image acquisitions. Cartesian trajectories in sequential lines (first column) and skip lines (second column), and non-Cartesian trajectories in radial lines (third column) and spiral lines (forth column). [Image credit: Lustig M. *et al.*[68]].

The Cartesian *k-space* sampling is performed by applying a phase encoding gradient in one direction and a frequency encoding gradient in the other direction. This is the most popular trajectory along which to acquire *k-space* samples; along straight lines in Figure 2-21 (first and second columns).[68] Most pulse sequences are based on the Cartesian *k-space* sampling used in clinical imaging due to a simple reconstruction in inverse fast Fourier transform (FFT) and robustness to many sources of system imperfections. Instead of Cartesian trajectories, non-Cartesian trajectories are in use, including *k-space* sampling along radial in Figure 2-21 (third column) and spiral trajectories in Figure 2-21 (fourth column).

K-space under-sampling

Sampling a larger *k-space* in a given amount of time requires *k-space* under-sampling, which acquires *k-space* samples at only a portion of the whole *k-space*. *K-space* under-sampling in terms of Cartesian patterns and resultant image artefacts are shown in Figure 2-22.[68]

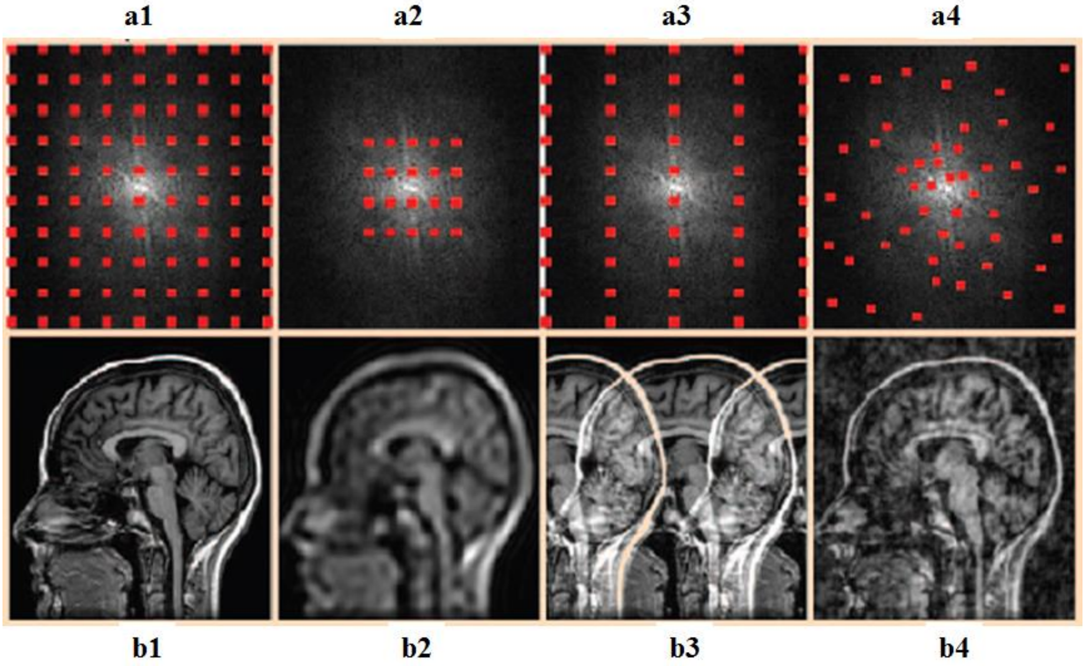

Figure 2-22. Cartesian *k-space* under-sampling patterns (first row) and resultant image artefacts (second row). Sampling patterns in (a1) full *k-space*, (a2) central *k-space*, (a3) skip *k-space* and (a4) random *k-space*. [Image credit: Lustig M. *et al.*[68]].

The *k-space* has strong signals around its centre due to most of the image being comprised of low spatial frequencies in Figure 2-22(a2) whilst high spatial frequencies around the noise level are at the edge of *k-space*. For instance, the low frequencies form the structure of objects and the high frequencies form the noise or motion of objects. Based on conjugate symmetry, theoretically only half of k-space needs to be acquired to reconstruct an MR image without the violation of the Nyquist criteria which causes artefacts in linear reconstructions. When the Nyquist criteria are not met, the objects will wrap around on the reconstructed image in Figure 2-22(b3).

Radial acquisitions are less sensitive to susceptibility to motion artefacts than Cartesian acquisitions whilst being significantly undersampled,[69] especially for high contrast objects.[70] Spiral acquisitions make efficient use of encoding gradients and are used for fast imaging applications.[71] However, non-Cartesian trajectories require filtered back-projection and/or interpolation schemes for efficient image reconstruction.[72]

The balance between temporal and spatial resolutions can be a trade-off in the change of imaging parameters to obtain images with high quality or acquired as fast as possible. Changing one affects the others because of the inter-relationship between signal-to-noise ratio (SNR), resolution and acquisition time. An important aspect of *k-space* undersampling is to acquire more k-space samples in a given amount of time for tracking and gating applications which require good temporal resolution with sufficient image quality. We explore a new method of using *k-space* undersampling for accelerating the MRI acquisition speed, more details on the dynamic keyhole method can be found in Chapter 3: Dynamic keyhole: A novel method to improve MR images in the presence of respiratory motion for real-time MRI and Chapter 4: Quantifying the accuracy of the tumor motion and area as a function of acceleration factor for the simulation of the dynamic keyhole magnetic resonance imaging method.

2.4 Audiovisual biofeedback

Audiovisual (AV) biofeedback has been employed for reducing the deleterious effects of respiratory-induced motion during medical imaging and radiotherapy by achieving reproducible breathing motion or breath-hold.[51, 52, 73-78] AV biofeedback as a respiratory guidance can render improved reproducibility in patient breathing motion, resulting in better reproducibility in patient anatomy both intra and inter-fractionally during imaging simulation and treatment.

The workflow of AV biofeedback is comprised of three steps:

(1) An individual breathing pattern is obtained using external respiratory signals from a real-time position management (RPM) system (Varian, Palo Alto, USA), monitoring the marker block on patient's abdomen.

(2) The breathing pattern is displayed on the patient's visual display using monitor, goggles, and mirror and screen.

(3) The patient controls their breathing in inhale and exhale breathing displacement and period.

The experimental setups of AV biofeedback systems are shown in Figure 2-23.

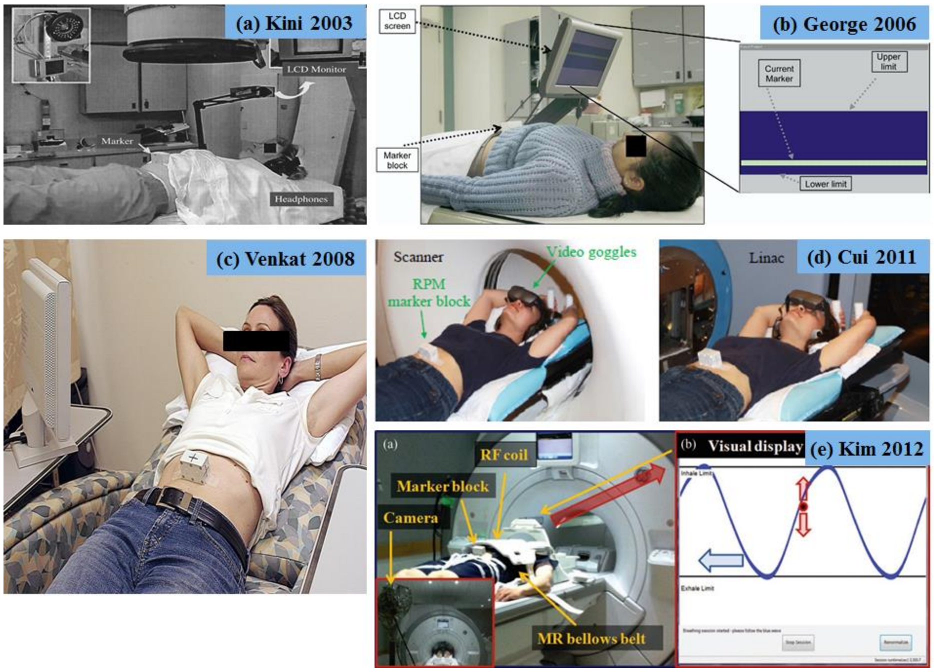

Figure 2-23. Audiovisual biofeedback systems designed by (a) Kini (2003), George (2006), Venkat (2008), Cui (2011) and Kim (2012).

Bar model

The study of Kini (2003) in Figure 2-23 (a),[51] demonstrated that FB without guidance resulted in a variable displacement and period, and an audio-instruction of "breathe in" or "breathe out" at periodic intervals can improve the reproducibility of the period of patient's breathing cycle and visual feedback shown as a real-time respiratory motion using a bar model which moves up (as they inhale) and down (as they exhale) can limit the displacement of patient's breathing displacement. Compared with FB and audio-only instruction, the study of George (2006) in Figure 2-23 (b)[73] using AV biofeedback combined the audio-instruction and the bar model visual biofeedback significantly reduced residual motion. However, baseline drift and shift occurred in a session and over sessions, respectively.[73]

Wave model

A wave model, utilizing a guiding wave of an average of ten individual breathing cycles was proposed by Venket (2008) in Figure 2-23 (c).[74] This study demonstrated that the wave model was superior to the bar model for all volunteers in sub-millimetre (0.8 mm) and sub-second (0.2 s), and also significantly better than the bar model by 50% and 70% in terms of respiratory motion reproducibility in displacement and period, respectively. A respiratory training system based on AV biofeedback in Figure 2-23 (d) was implemented to improve patients' respiratory regularity during 4DCT image acquisition.[75] This is to eliminate the artefacts in 4DCT images caused by intra-fraction irregular breathing and improve dose delivery efficiency during radiotherapy. AV biofeedback in Figure 2-23 (e) was employed to improve the reproducibility of diaphragm motion measured in MRI.[76] The reproducibility of intra-fraction diaphragm motion was improved by (1) 38% from 2.6 mm (FB) to 1.6 mm (AV biofeedback) in displacement and (2) 82% from 1.7 s (FB) to 0.3 s (AV biofeedback) in period.

2.5 Research motivation and rationale for this thesis

Magnetic resonance imaging (MRI) is an ideal candidate for medical applications owing to the fact that it has excellent soft-tissue contrast and does not expose the patient to ionizing radiation. In addition, MRI is also capable of providing both anatomical and functional imaging. Radiotherapy systems integrated with MRI have been proposed and the Viewray system is currently clinically available for MRI guided radiotherapy.[44, 79] In addition, tumour motion and position using MRI guidance can be directly measured from MR images of tumours without the use of surrogates and implanted markers.

Real-time imaging is necessary for continuous monitoring of patient for therapeutic guidance.[80-83] However, the frame-rate of MRI in thoracic and abdominal regions is considerably slower (4 Hz) due to a large FOV, decreasing the prediction accuracy of tracking and gating techniques in the presence of system latency from target imaging and radiation delivery.[84] This thesis proposes a novel MRI reconstruction method (Dynamic Keyhole) which can (1) improve temporal resolution for real-time lung tumour imaging (i.e. imaging frequency greater than 15 Hz) to compensate the system latency and (2) maintain the accuracy in reconstructed tumour motion and area for real-time tumour gating and tracking.

Respiratory guidance is important tool for improving the regularity of tumour motion, position, and volume throughout the course of radiotherapy. The impact of AV biofeedback on surrogates' motion has already been investigated.[85] However, lung tumour motion is independent to tumour size, location and pulmonary function.[122] Thus, it is necessary to investigate the impact of AV biofeedback on tumour motion, position and volume using lung tumour information directly measured from MR images (no imaging doses). This thesis proposes a novel approach of AV biofeedback which improves (1) cine-MRI for tumour motion consistency, (2) breath-hold MRI for tumour position reproducibility and volume consistency, and (3) respiratory-gated MRI for image quality improvement and scan time reduction for improving the quality of lung cancer radiotherapy.

This thesis presents a novel MRI reconstruction method (Dynamic Keyhole) and its assessment. This also presents the impact of AV biofeedback guidance on lung tumours across cine-MRI, breath-hold MRI and respiratory-MRI.

Chapter 3: Dynamic keyhole: A novel method to improve MR images in the presence of respiratory motion for real-time MRI

A version of this chapter has been published: Lee D, Pollock S, Whelan B, Keall P, Kim T. "Dynamic keyhole: A novel method to improve MR images in the presence of respiratory motion for real-time MRI", Medical physics, ***41*** *(7): 072304 (2014). http://dx.doi.org/10.1118/1.4883882.*

ABSTRACT

Purpose: In this work, we present a novel MRI reconstruction method to improve the quality of MR images in the presence of respiratory motion for real-time thoracic image-guided radiotherapy.

Methods: This new reconstruction method is called Dynamic Keyhole and utilizes a library of previously acquired, peripheral k-space datasets from the same (or similar) respiratory state in conjunction with central k-space datasets acquired in real-time. Internal or external respiratory signals are utilized to sort, match, and combine the two separate peripheral and central k-space datasets with respect to respiratory displacement, thereby reducing acquisition time and improving image quality without respiratory-related artifacts. In this study, the dynamic keyhole, conventional keyhole, and zero-filling methods were compared to full k-space acquisition (ground truth) for sixty coronal datasets acquired from 15 healthy human subjects.

Results: For the same image-quality difference from the ground-truth image, the dynamic keyhole method reused 79% of the prior peripheral phase-encoding lines, while the conventional keyhole reused 73% and zero-filling 63% (p-value < 0.0001), corresponding to faster acquisition speed of dynamic keyhole for real-time imaging applications.

Conclusions: This study demonstrates that the dynamic keyhole method is a promising technique for clinical applications such as image-guided radiotherapy requiring real-time MR monitoring of the thoracic region. Based on the results from this study, the dynamic keyhole method could increase the temporal resolution by a factor of five compared with full k-space methods.

Keywords: real-time imaging; thoracic imaging; motion artifacts; respiratory motion; radiotherapy guidance

3.1 Introduction

There are a number of medical applications in interventional radiology and cancer radiotherapy that require real-time patient images to continuously monitor the region of interest for therapeutic guidance.[81-83, 86] Magnetic resonance imaging (MRI) is an ideal candidate for these applications; it has excellent soft-tissue contrast, does not expose subjects to ionizing radiation,[87] and is capable of both anatomical and functional imaging. Recently, radiotherapy systems integrated with MRI have been proposed by Kolling (2013),[88] Viewray Inc. (2011),[89] Raaymakers (2009),[79] and Fallone (2009).[90]

In order to be utilized for real-time imaging,[91-93] a technique offering both fast and quasi-continuous image acquisition and reconstruction is required for MR image guidance. However, thoracic imaging in conventional MRI often suffers from motion artifacts[94] and long scan times, which are not suitable for image-guided therapeutic procedures. Hence, there is a need for methods that can reduce scan times without inducing respiratory-related artifacts in the images of the thoracic region.

One method to speed up MR image acquisition is to exploit the basic structure of the raw datasets (digitized MRI signals) in k-space (Fourier transform of the MR image). Central (low-frequency) k-space datasets contain the majority of the image information, while peripheral (high-frequency) k-space datasets are associated with fine image details, such as edge definition and image sharpness. In applications requiring real-time imaging, undersampling k-space datasets directly corresponds to a reduction in imaging time.[95]

Conventionally, the unmeasured datasets are simply filled with zeros in a technique called zero-filling,[96] but this results in image blurring, low image resolution and contrast. An improvement to zero-filling is the conventional keyhole technique.[95, 97, 98] In this case, the missing data are filled with a previously measured single peripheral k-space dataset. The conventional keyhole method allows continuous motion to be monitored with an acceptable level of image quality in cases where motion is negligible. But, in cases in which the range of motion is large, there will be a mismatch between the previously obtained peripheral dataset and the central k-space datasets. This mismatch can result in significant image artifacts, particularly in large field of view (FOV) imaging due to longer acquisition times.

Other undersampling techniques to reduce both acquisition time and motion sensitivity are circular,[69] radial[99], and spiral[100] undersampling. In these approaches, unmeasured points can still cause artifacts due to zero-filling, interpolation, and oversampling in duplicated data.[101, 102] The large FOV in thoracic imaging limits these undersampling schemes due to the out-of-field object size exceeding the diameter of FOV.[69] The speed of acquisition can be accelerated using compressed sensing[103] in some applications. However, this requires computationally-intensive iterative reconstruction[104], leading to a delay between image acquisition and reconstruction which is a barrier to real-time applications. This limits the applicability of these undersampling techniques in the thoracic region, in which respiration can cause significant organ motion and a large field of view is often required.[105-108] As yet, an effective technique for real-time imaging in these regions has not been proposed.

In this study, we introduced a new reconstruction method called Dynamic Keyhole, which utilizes a library of previously acquired prior peripheral k-space datasets for the same (or similar) respiratory state in conjunction with the central k-space datasets. In this method, real-time internal or external respiratory signals were utilized to sort, match, and combine the two separate peripheral and central k-space datasets with respect to respiratory displacement. In addition, we demonstrated that the dynamic keyhole method can reduce MR image acquisition time, as well as improve image quality in the presence of respiratory motion in the thoracic region. Image reconstruction performance was compared using sixty MRI datasets from fifteen healthy human subjects. The dynamic keyhole method was compared with the conventional methods: zero-filling and conventional keyhole.

3.2 Methods

The following sections describe the processes of the dynamic keyhole method, its implementation, and a retrospective simulation to test its efficiency compared to the zero-filling and conventional keyhole methods.

3.2.1 Dynamic Keyhole Method

The dynamic keyhole method is an extension of the conventional keyhole method.[95] Instead of using a single prior peripheral k-space dataset, the dynamic keyhole method uses a library of prior peripheral k-space datasets, each corresponding to a different respiratory displacement. Hence, rather than matching a prior peripheral k-space dataset of a particular respiratory displacement to every central k-space dataset across a range of respiratory displacements, the dynamic keyhole method selects and closely matches peripheral k-space datasets from the library, with the central k-space datasets taken in real time and combined with the prior k-space datasets by respiratory displacement matching. A comparison between the dynamic keyhole method and the conventional keyhole method is shown in Figure 3-1.

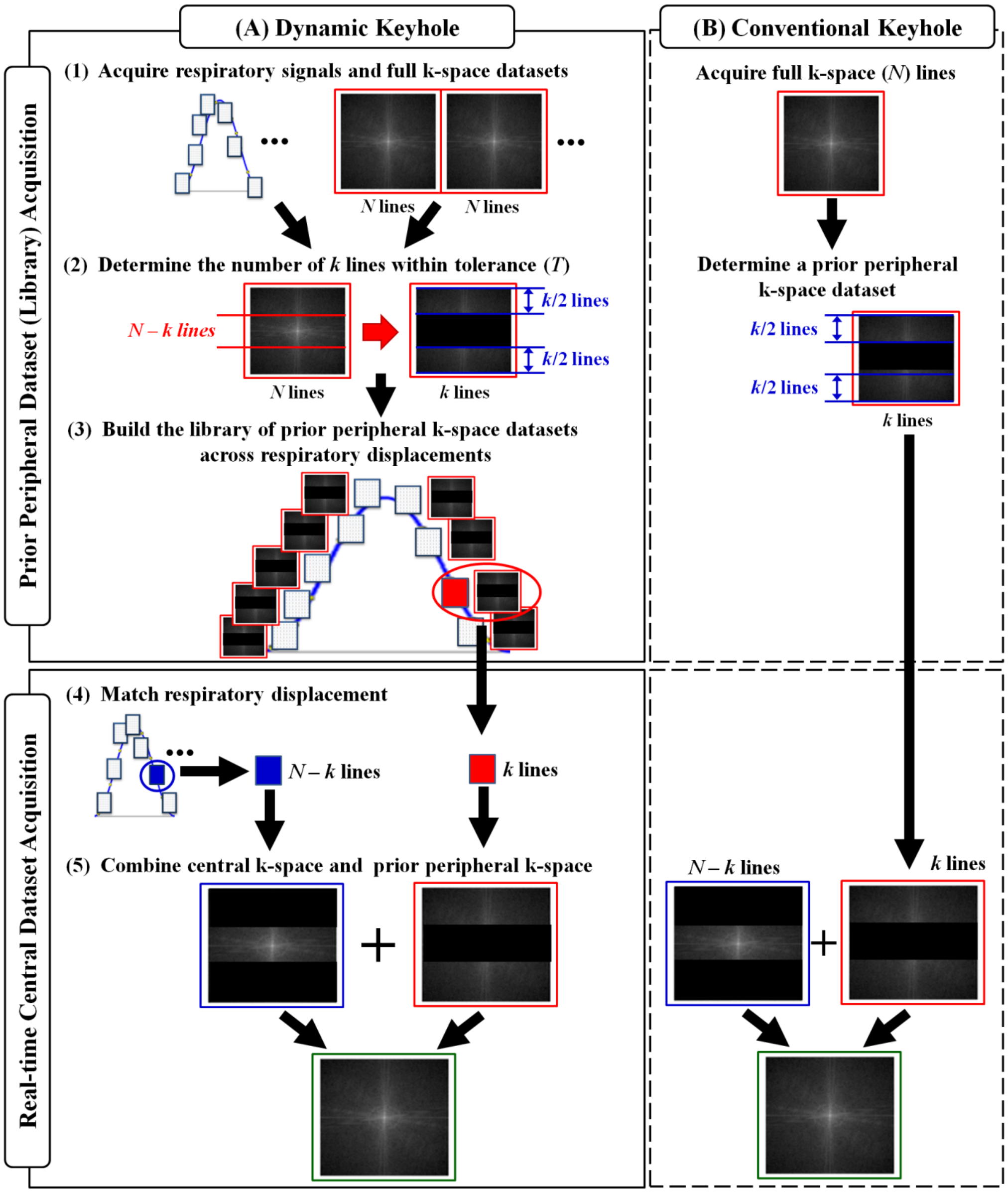

Figure 3-1. The dynamic keyhole method (A) compared to the conventional keyhole method (B). The conventional keyhole method uses a single prior peripheral k-space dataset while the dynamic keyhole method uses a library of multiple prior peripheral k-space datasets across a range of respiratory displacements.

The dynamic keyhole method is composed of two processes: (1) Acquiring a library of prior peripheral k-space datasets; (2) Acquiring real-time central k-space datasets. Respiratory signals are utilized to improve a match of the library of prior peripheral k-space datasets with central k-space datasets, resulting in fast MR imaging by undersampling k-space, while minimizing respiratory-related artifacts. Each of these steps is explained in detail below.

3.2.2 Prior peripheral k-space dataset (library) acquisition

In this retrospective study using existing datasets, five respiratory cycles of about twenty seconds were initially used, based on clinical MRI respiratory-gating practice,[109] to build the library of prior peripheral k-space datasets, using the following steps:

1. In Figure 3-1(1), respiratory signals were continuously acquired. Full k-space datasets were synchronized with the respiratory signal, beginning at peak inhalation and ending after five respiratory cycles. The synchronized respiratory signals and full k-space datasets can be expressed as $Lib(d_{n,}\, N)$, where d is respiratory displacement, n is the n^{th} full k-space dataset and N is the number of full k-space phase encoding lines (N = 256).
2. At the end of the five respiratory cycles, $Lib\left(d_{n,}\, N\right)$ was sorted with respect to unique respiratory displacements $Lib'(d_{m,}\, N)$, where m is the m^{th} position of the respiratory displacement from the peak inhalation with a millimeter bin width, and reconstructed using a 2D Fourier Transform, $I\left(Lib'(d_{m,}\, N)\right)$. A tolerance T , which represents a fraction δ of average image intensity $\overline{I(L\imath b'(d_{m,}\, N))}$ determined on a pixel-by-pixel basis, was chosen and used as a measure of image quality. The tolerance T can be expressed as

$$Tolerance\ (T) = \overline{I(Lib'(d_{m,}\ N))} \times \delta \qquad (1)$$

In this study, we used δ=0.1 (10%) of $\overline{I(Lib(d_{m,}\ N))}$ for the tolerance, which corresponds to the typical image quality achievable by conventional keyhole method. Then, the number of prior peripheral k-space phase-encoding lines, k, was determined within T in Figure 3-1(2).

3. In Figure 3-1(3), the library of prior peripheral k-space datasets, $Lib'(d_{m,}\ k)$ acquired at the same respiratory displacements from d_1 to d_m, was reconstructed using $256 - k$ lines ($k = 1, 2, \dots, 255$). Each reconstructed image was compared with the image reconstructed using 256 lines, and k was increased until the difference between the two images exceeded T. If there were more than two k-space datasets with the same respiratory displacement, the process was repeated and the average value of k was used to form the library.

For the zero-filling and conventional keyhole reconstructions, the k lines of N with zeros (zero-filling) or a single dataset taken in the mid-exhalation phase (conventional keyhole) was determined using a similar process as described in the three steps above. The k lines of zeros (zero-filling) or the k lines of a single dataset (conventional keyhole) were increased until the difference of the two images exceeded T.

3.2.3 Real-time central k-space dataset acquisition

The real-time central k-space dataset acquisition began after the library acquisition. In this instance, the size of the central k-space datasets (N- k lines) was determined through matching respiratory displacement between a present respiratory signal and the matched dataset of the library, shown in Figure 3-1(4). Then, the (N- k lines) of central k-space dataset were combined with the k lines of the matched dataset in Figure 3-1(5).

3.2.4 Testing the dynamic keyhole method

In order to investigate the efficacy of the dynamic keyhole method compared to the zero-filling and conventional keyhole methods, the three methods were implemented in Matlab version 7.13 (The MathWorks, Natick, USA) and tested retrospectively using respiratory and MR image datasets acquired in a previous study.[76] Sixty MRI datasets with associated respiratory motion datasets were acquired from fifteen healthy human subjects in the supine position using a 3T GE MR scanner (GE Healthcare, Waukesha, USA). Each subject had a total of four MRI scans over two separate imaging sessions. Each dataset consisted of 512 images in the 2D coronal plane acquired approximately every 200 ms using fast gradient recalled echo (fGRE) pulse sequence with a field of view (FOV) of 480×384 mm^2 and a 96×96 matrix size per frame across more than twenty respiratory cycles. Each MR image was interpolated to a 256×256 matrix by the MR scanner. Internal respiratory signals (5Hz) were obtained from each MR image at the peak of the right diaphragm of the dome of the liver. The Real-time Position Management (RPM) system (Varian Medical Systems, Palo Alto, USA) was used to monitor the subjects' abdominal respiratory motion to obtain external respiratory signals (30Hz). Overall, for these datasets, the correlation of internal and external signals was found to be very high in a previous study, an average Pearson's R-value of 0.96.[85] The 30 Hz external signal was downsampled to the temporal resolution of 5 Hz for (1) the use of respiratory displacements at the closest acquisition time between respiratory signals and full k-space datasets in Figure 3-1(3), and (2) the use of the sixty datasets acquired at 5 Hz temporal resolution during the acquisition of central k-space datasets in Figure 3-1(4).

The dynamic keyhole method was compared with the zero-filling and conventional keyhole methods in two ways: firstly, by evaluating the acquisition speed for the same image quality and secondly, by evaluating the image quality at the same acquisition speed[95]. For the first comparison, the acquisition speeds of the methods were quantified by using the number of *k* lines reused by each method to achieve the same image quality. For the second comparison, the quality of the images reconstructed from the same number of *k* lines was compared with the quality of the original ground-truth image reconstructed from the full k-space datasets by using the differences in image intensity.

The impact of the use of internal or external respiratory signals was also investigated. The number of *k* lines required to achieve the same image quality was quantified for both respiratory signals for each of the three methods. Quantitative statistical comparison of the performance was determined using the mean, standard deviation, and paired Student’s t-test (Excel 2010, Microsoft, Redmond, USA).

3.3 Results

The correlation between faster image acquisition and better image quality for the zero-filling, conventional keyhole, and dynamic keyhole methods is shown in Figure 3-2.

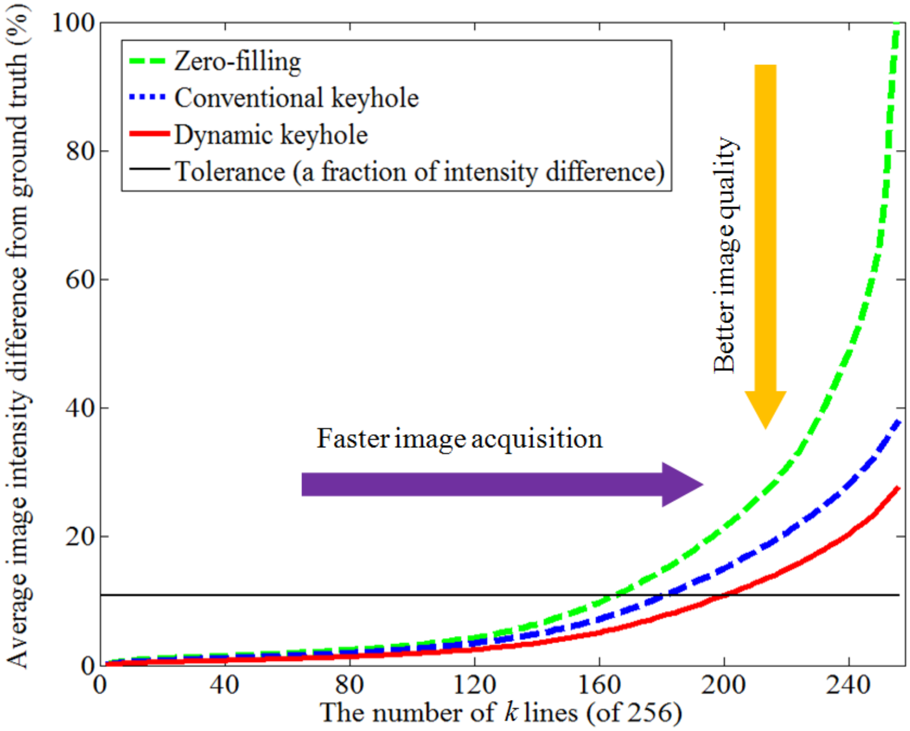

Figure 3-2. The relationship between faster image acquisition (horizontal arrow) and better image quality (vertical arrow) for each of the three methods tested.

The intersections of each of the curves with the tolerance, which is 10% of average image intensity (thin, horizontal black line), indicate the number of *k* lines that were reused for each method. The image intensity difference increased when the number of *k* lines was increased in all three methods, but was smallest in the dynamic keyhole method. This showed that the dynamic keyhole method can reuse more *k* lines for the same image quality, resulting in faster image acquisition.

Figure 3-3 shows reconstructed images using the different number of *k* lines required to produce the same image quality compared to original ground truth image.

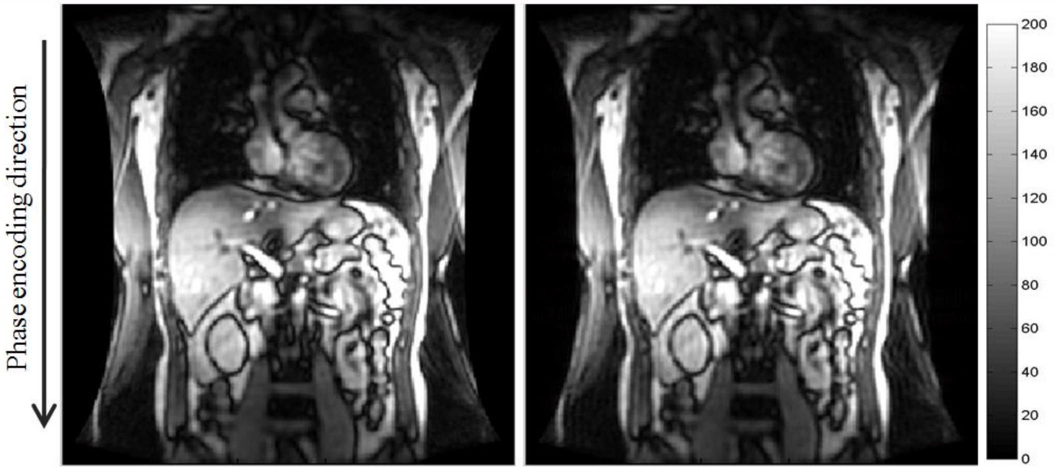

(a) Original image (0 of 256 lines) (b) Zero-filling (152 of 256 lines with zeros)

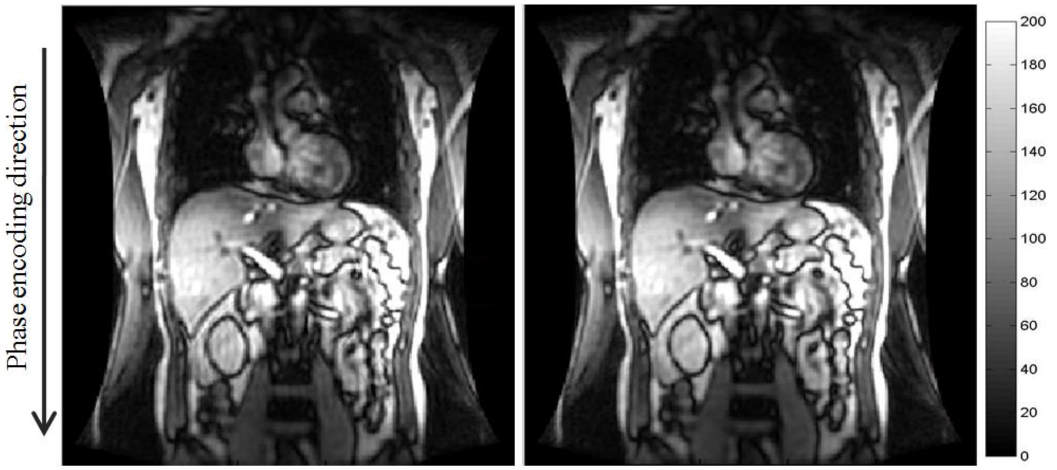

(c) Conventional keyhole (170 of 256 lines) (d) Dynamic keyhole (196 of 256 lines)

Figure 3-3. Reconstructed images using the different number of *k* lines required to produce the same image quality compared to original ground truth image: (a) original image (*k* = 0 lines), (b) zero-filling reconstructed image (*k* = 152 lines with zeros), (c) conventional keyhole reconstructed image (*k* = 170 lines) and (d) dynamic keyhole reconstructed image (*k* = 196 lines).

The zero-filling method in Figure 3-3(b) reused 152 lines with zeros, the conventional keyhole method in Figure 3-3(c) reused 170 lines, and the dynamic keyhole method in Figure 3-3(d) reused 196 lines. Compared to the other two methods, the dynamic keyhole method reused more *k* lines to reconstruct the same image quality, indicating a faster image acquisition time.

The performance of the three methods regarding the improvement of image quality was also evaluated. To provide a comparison of the image quality, an example of reconstructed images with 204 of 256 lines for a library across all the methods is shown in Figure 3-4.

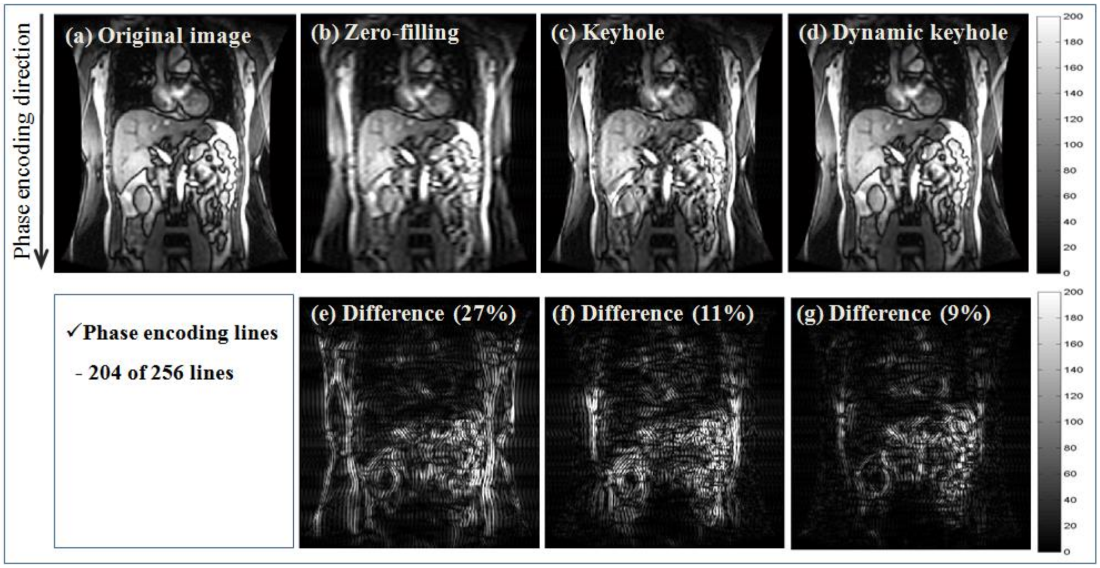

Figure 3-4. Reconstructed MR images utilizing (b) zero-filling, (c) conventional keyhole and (d) dynamic keyhole, where 204 of 256 lines were reused. (e), (f) and (g) display the difference between the original image (a) and the reconstructed images for the zero-filling (27%), conventional keyhole (11%), and dynamic keyhole (9%) methods, respectively.

From the reconstructed images shown in Figure 3-4, it is evident that the image quality of the dynamic keyhole method was superior to the zero-filling and conventional keyhole methods when 204 of 256 lines were reused. The reconstructed images using the zero-filling method in Figure 3-4(b) contained considerable blurring image artifacts. The conventional keyhole image in Figure 3-4(c) produced better image quality than the zero-filling method, but still contained motion artifacts around regions affected by respiratory motion such as the diaphragm, kidneys, and liver. However, respiratory-related artifacts were minimized on the reconstructed image by the dynamic keyhole method in Figure 3-4(d).

The average number of *k* lines from the sixty datasets across the three methods using internal or external respiratory signals is shown in Table 3-1.

Table 3-1. Zero-filling, conventional keyhole and dynamic keyhole results of the mean and standard deviation (STD) of the number of *k* lines to achieve the same image quality difference compared with the original images for the sixty obtained datasets.

Methods	Mean ± STD of *k* lines
Zero-filling	162 (63%) ± 8
Conventional keyhole	188 (73%) ± 14
Dynamic keyhole (internal respiratory signal)	204 (79%) ± 17
Dynamic keyhole (external respiratory signal)	202 (78%) ± 17

Across the sixty datasets, the dynamic keyhole method using the internal respiratory signals reused an average of 204±17 of 256 (79%) lines compared to

162±8 of 256 (63%) lines in the zero-filling method and 188±14 of 256 (73%) lines in the conventional keyhole method to achieve the same difference from the ground truth image. The difference in the number of *k* lines between the dynamic keyhole method and the zero-filling or conventional keyhole method were statistically significant with a *p-value* < 0.0001 in both cases. There was a two-line difference in the average of *k* lines between the internal and external respiratory signals in the dynamic keyhole method (*p-value* < 0.0001). However, there was only a 1% difference, indicating that either internal or external respiratory signals are suitable for the dynamic keyhole method. The dynamic keyhole method required less scan time compared to the conventional keyhole method to achieve the same image quality during real-time central k-space dataset acquisition. For example, once the library of the prior peripheral k-space datasets were acquired, the real-time central k-space dataset acquisition of the dynamic keyhole method achieved image acquisition speeds of about 40 ms (52 of 256 lines) per image compared to about 53 ms (68 of 256 lines) per image for the conventional keyhole.

The performance of the dynamic keyhole method using the different input signals over the intra- and inter-subject variations is shown in Figure 3-5. For the intra- and inter-subject variations, sixty datasets were grouped by respiratory signal and subject.

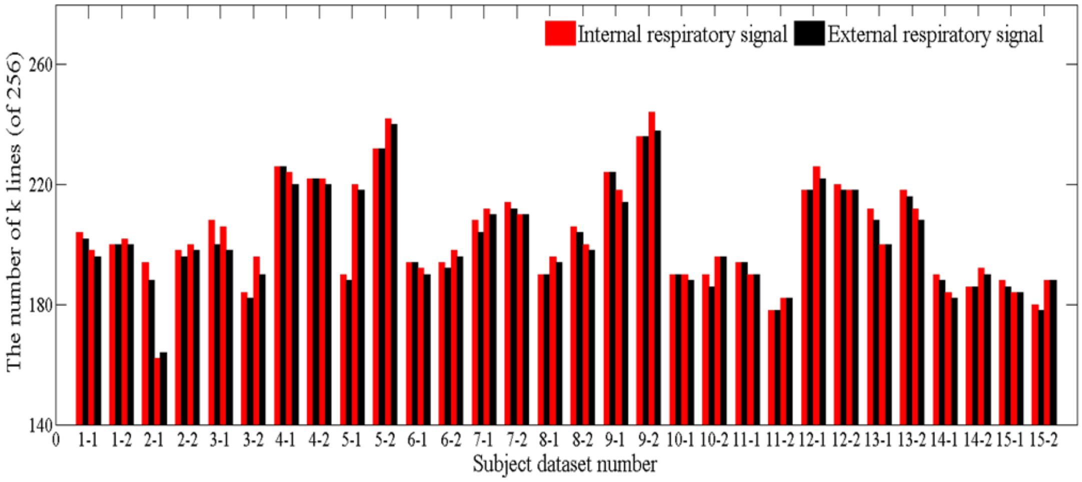

Figure 3-5. The number of *k* lines (of 256) for the dynamic keyhole method to achieve a 10% difference with the original image using the internal (red) and external (black) respiratory signals over the sixty obtained datasets of 15 subjects (two datasets, each with internal and external respiratory signals, over two imaging sessions). The subject dataset numbers are labeled by subject-imaging session, e.g. 5-2 is subject 5, session 2.

The internal respiratory signals compared to the external respiratory signal were similar in all of the sixty datasets. The largest difference was observed in subject 3, session 1, where eight more *k* lines were reused using the internal respiratory signals than the external signal. A larger difference in *k* lines was found when there were regular internal and relatively irregular external respiratory cycles, for example the datasets in subject 3, session 1 and subject 9, session 2. The *k* lines were lower with the internal respiratory signals in only one case, subject 2, session 1, due to irregular internal and relatively regular external respiratory signals.

The average of maximum-to-minimum range of intra-subject variation using internal (or external) respiratory signals and the standard deviation of *k* lines was

12±11 lines (or 12±10 lines). The average of maximum-to-minimum range of inter-subject variation across fifteen subjects and the standard deviation of k lines was 47±15 lines (or 49±16 lines).

3.4 Discussion

Real-time thoracic imaging often requires a large FOV and includes respiratory motion, leading to longer acquisition time and respiratory-related artifacts due to organ displacement. In this study, we introduced the dynamic keyhole method, which utilizes a library of prior peripheral k-space datasets corresponding to multiple respiratory states that are matched to real-time central k-space datasets using internal or external respiratory information. Using the dynamic keyhole method, we demonstrated fast image acquisition while maintaining image quality.

We demonstrated that the dynamic keyhole method resulted in a significant reduction in the amount of central k-space datasets necessary to acquire an image of sufficient quality. For the same amount of central k-space datasets, the dynamic keyhole method resulted in improved image quality compared to the zero-filling and conventional keyhole methods, as shown in Figure 3-3 and Figure 3-4. The dynamic keyhole method reused 79% of prior peripheral k-space datasets to reconstruct artifact-free images, 6% more than conventional keyhole, and 16% more than zero-filling. As a result, the number of phase encoding lines was reduced by up to 79% from the full k-space acquisition during the central k-space dataset acquisition. This shows that the dynamic keyhole could be a valuable tool for fast MR image acquisition, which is required for real-time thoracic imaging in the presence of respiratory motion. In addition, the acquisition of full k-space datasets may not be necessary during library acquisition (Figure 3-1(A)(1)) when the same number of peripheral phase encoding lines is used. The scan time could be further reduced in this stage of the dynamic keyhole method if the k-space is not fully acquired.

To accelerate image acquisition time, compressed sensing[103, 104] and parallel imaging[110, 111] have been proposed for improving both acquisition time and quality of MR images. However, the delay between image acquisition and reconstruction in compressed sensing, due to the iterative reconstruction, and the sensitivity of multi-receiver coils in parallel imaging lead to residual aliasing and noise enhancement artifacts.[101] The barrier to real-time thoracic or abdominal imaging in compressed sensing could be, however, improved using the dynamic keyhole method. In compressed sensing, superior image quality of images reconstructed by the dynamic keyhole method could reduce iterations. Furthermore, the dynamic keyhole method can be combined with other undersampling methods, such as circular[69], radial[99], and spiral[100] to improve undersampling schemes for the out-of-field object size exceeding the diameter of FOV.[69]

In the current retrospective study, the internal respiratory signal measured directly from obtained images (manual process) was utilized.[76] This resulted in slightly better dynamic keyhole performance than the external respiratory signal in terms of *k*-line reduction. For prospective implementation, an automatically determined diaphragm position[82, 105, 112] is necessary instead of the manual process utilized here, but it requires additional internal respiratory signal measurements whilst k-space datasets are measured and images reconstructed. Alternatively, the external respiratory signals can be easily utilized with only a small penalty in terms of *k*-line reduction, as there is a high internal-external signal correlation for the dataset used in this study (Pearson's R-value = 0.96).[85]

The dynamic keyhole method uses previously acquired full k-space datasets, and in an actual implementation, the library of k-space datasets for the prior peripheral k-space dataset and the central k-space dataset acquisition would be at a different frequency. Even though the library may be acquired at a lower temporal resolution, the dynamic keyhole method should give improved results over the conventional keyhole method because it utilizes multiple prior peripheral datasets matched to various respiratory displacements. In an additional study (data not shown), a temporal resolution of 800 ms was tested instead of 200 ms. In this case, the match between central and peripheral datasets was compromised; the library of a lower temporal resolution resulted in six fewer reused *k* lines on average compared with the 200 ms case. However, even in this case, the dynamic keyhole method was superior to the conventional keyhole when reusing an average of ten more *k* lines. Serially acquired peripheral dataset acquisitions corresponding to the same dataset magnitude as that needed for the real-time central k-space datasets could reduce data mismatch, but it would increase the time required to create the library.

The performance of the proposed dynamic keyhole method is reliant on the quality of the library and the ability to match it accurately to the central k-space datasets. After an additional simulation to find the optimum amount of datasets for the library, we suggest a greater number of breathing cycles when large cycle-to-cycle variations in respiratory displacement are present. This increase is to better account for variability in the subjects' breathing patterns. In an example from the subject 9, session 1, the number of *k* lines was measured at 186 and 200 lines when a single respiratory cycle and five respiratory cycles were used, respectively, due to irregular breathing (e.g. baseline drifts, overly deep/shallow breathing) during the library acquisition. The major factors leading to improved performance in the dynamic keyhole method were regular breathing[76] and the coverage of the library in respiratory displacements, which resulted in up to an 80% performance improvement with the internal respiratory signals and 70% with the external respiratory signals.

This study has demonstrated that the dynamic keyhole method is a promising MR image reconstruction technique applicable for real-time imaging of the thoracic and abdominal regions. The dynamic keyhole can be easily applied to a variety of pulse sequences and scanners, and can be combined with other fast imaging techniques, such as k-space undersampling, and respiratory-gated imaging for real-time image guided radiotherapy, such as radiotherapy systems integrated with MRI.[79, 89, 90] A variety of inputs can be utilized for a respiratory signal, such as bellows belts[113], navigator[112], and ANZAI.[114]

3.5 Conclusions

In this study, the dynamic keyhole method utilized respiratory signals to improve MR images in the presence of respiratory motion, leading to a 79% reduction in central k-space datasets required for real-time MR imaging, while maintaining sufficient image quality. In addition, this was the first study in which MR image reconstruction utilized respiratory signals for real-time thoracic imaging. Our results suggest that the dynamic keyhole method could be a desirable technique for image-guided radiation therapy and MRI-guided radiotherapy that requires real-time MR monitoring in the thoracic region.

Chapter 4: Quantifying the accuracy of the tumor motion and area as a function of acceleration factor for the simulation of the dynamic keyhole magnetic resonance imaging method

A version of this chapter has been published: Lee D, Greer B P, Pollock S, Kim T and Keall P. "Quantifying the accuracy of the tumor motion and area as a function of acceleration factor for the simulation of the dynamic keyhole magnetic resonance imaging method", Medical physics, ***43*** *(5): 2639 (2016), http://dx.doi.org/10.1118/1.4947508.*

ABSTRACT

Purpose: The dynamic keyhole is a new MR image reconstruction method for thoracic and abdominal MR imaging. To date, this method has not been investigated with cancer patient MRI data. The goal of this study was to assess the dynamic keyhole method for the task of lung tumor localization using cine-MR images reconstructed in the presence of respiratory motion.

Methods: The dynamic keyhole method utilizes a previously acquired a library of peripheral k-space datasets at similar displacement and phase (where phase is simply used to determine whether the breathing is inhale to exhale or exhale to inhale) respiratory bins in conjunction with central k-space datasets (keyhole) acquired. External respiratory signals drive the process of sorting, matching and combining the two k-space streams for each respiratory bin, thereby achieving faster image acquisition without substantial motion artifacts. This study was the first that investigates the impact of k-space undersampling on lung tumor motion and area assessment across clinically available techniques (zero-filling and conventional keyhole). In this study, the dynamic keyhole, conventional keyhole and zero-filling methods were compared to full k-space dataset acquisition by quantifying (1) keyhole size required for central k-space datasets for constant image quality across sixty four cine-MRI datasets from nine lung cancer patients, (2) the intensity difference between the original and reconstructed images in a constant keyhole size, and (3) the accuracy of tumor motion and area directly measured by tumor auto-contouring.

Results: For constant image quality, the dynamic keyhole method, conventional keyhole and zero-filling methods required 22%, 34% and 49% of the keyhole size ($P < 0.0001$), respectively, compared to the full k-space image acquisition method. Compared to the conventional keyhole and zero-filling reconstructed images with the keyhole size utilized in the dynamic keyhole method, an average intensity difference of the dynamic keyhole reconstructed images ($P < 0.0001$) was minimal, and resulted in the accuracy of tumor motion within 99.6% ($P < 0.0001$) and the accuracy of tumor area within 98.0% ($P < 0.0001$) for lung tumor monitoring applications.

Conclusions: This study demonstrates that the dynamic keyhole method is a promising technique for clinical applications such as image-guided radiation therapy requiring the MR monitoring of thoracic tumors. Based on the results from this study, the dynamic keyhole method could increase the imaging frequency by up to a factor of five compared with full k-space methods for real-time lung tumor MRI.

Keywords: lung tumor; real-time imaging; thoracic MRI; image reconstruction; MRI-guided;

4.1 Introduction

The tumor motion of thoracic and abdominal regions affected by respiration varies both breath-to-breath and day-to-day[5, 27], resulting in an averaging of the dose distribution over the path of the tumor motion and a shift of the dose distribution.[115] In order to improve the quality of radiation delivery, external respiratory surrogates are often used to predict internal tumor motion[84, 116] but the internal tumor motion does not always accurately correlate to the external surrogates due to breathing and heartbeat.[117-119] In addition, tumor growth and shrinkage is expected throughout the course of radiation treatment.[34]

Tumor motion monitoring[27, 32, 35-38] can provide tumor positions measured from implanted markers or surrogates for cancer radiotherapy,[4] but there is not an appropriate method to consider tumor deformation due to the lack of tumor contrast required for tumor contouring resulted in the limitation of tumor delineation. In order to utilize the superior soft-tissue contrast of magnetic resonance imaging (MRI), radiation therapy systems integrated with MRI have been proposed for MRI guided radiation therapy[79, 88, 90, 120, 121] and the Viewray system is commercially available for MRI guidance in clinical practice.[121] MRI-based techniques[81, 121, 122] monitor respiratory-induced lung and abdominal organ motion at a rate of 4 Hz, however this is considerably slower for accurate prediction in the system latency (greater than 200 ms) between target location and radiation delivery,[84] compared with 25 Hz for Cyberknife Synchrony (Accuray Incorporated, Sunnyvale, CA)[32] and the external surrogate monitoring of 25 to 30 Hz for the real-time position management (RPM) system (Varian Medical System Inc, Palo Alto, CA).[123, 124]

Given the advantages of MRI over other image modalities and tumor monitoring techniques and the emerging hybrid MRI-radiotherapy systems, optimizing the imaging speed of MRI for continuous, tumor monitoring is a valuable milestone for future hybrid radiotherapy systems. Zero-filling (filling unmeasured data points with zeros) and conventional keyhole (filling unmeasured data points with a previously acquired single full k-space dataset) are current MR image reconstruction methods designed to reduce MR image acquisition time, however such techniques often result in a compromise of image quality due to intensity loss in the zero-filling method, and displacement and phase changes averaged intensity in the conventional keyhole method.[95, 96] Non-Cartesian undersampling such as radial[99] and spiral[100] can reduce image artifacts from motion sensitivity, but this still causes intensity loss due to interpolation at unmeasured points and out-of-field due to the limited diameter for a large field of view.[69] The sensitivity of multi-receiver coils in parallel imaging leads to residual aliasing and noise enhancement artifacts[101] and compressed sensing requires an iterative reconstruction[104], which limits real-time thoracic and abdominal MR imaging. Hence, an MR image reconstruction method reducing image acquisition time whilst maintaining the image quality of full k-space datasets on reconstructed images is desirable for real-time lung tumor monitoring.

The previous study introduced the concept of the dynamic keyhole method and evaluated it using the MR images of healthy volunteers.[125] This previous study imaged healthy volunteers utilizing the peak of liver dome for diaphragm motion monitoring, but the position of cine-MR image measurement can vary based on the tumor location of each cancer patient.[126, 127] This study is hence required to assess (1) the dynamic keyhole method which reconstructs lung tumor MR images in the presence of respiratory-driven lung tumor motion and (2) the tumor motion difference and tumor area similarity between original and reconstructed images for the technical improvement of the dynamic keyhole method.

In this study, we test that the dynamic keyhole method can reduce MR image acquisition time and improve image quality compared to currently available MRI reconstruction methods (zero-filling and conventional keyhole) in sixty four lung tumor datasets acquired from nine lung cancer patients. In addition, we assess the accuracy of the tumor motion and area in the reconstructed two-dimensional cine-MR images. Lung tumors directly measured by auto-contouring were compared between the original and the dynamic keyhole reconstructed images, in addition to the conventional keyhole and zero-filling reconstructed images.

4.2 Methods

The dynamic keyhole method is comprised of library acquisition (full k-space datasets) and central k-space dataset acquisition (central k-space datasets).[125] A keyhole size, the size of the central k-space datasets is determined using the full k-space datasets (i.e. full k-space datasets = peripheral k-space datasets + central k-space datasets (keyhole)) at similar respiratory states prior to the central k-space dataset acquisition. Then, the central k-space datasets are obtained to be combined with the library of peripheral k-space datasets at the corresponding respiratory state in displacement and phase (where phase is simply used to determine whether the breathing is inhale to exhale or exhale to inhale).

In the previous study,[125] full k-space datasets were continuously obtained at a set acquisition interval (i.e. 200 ms) over five respiratory cycles so that multiple full k-space datasets could be obtained for each displacement bin. This required extra time to process the multiple full k-space datasets acquired during the library acquisition phase of the dynamic keyhole method. However, the current study optimized the library acquisition to allow only one full k-space dataset for each respiratory displacement bin. The following sections describe lung tumor cine-MRI datasets, the optimized library acquisition of the dynamic keyhole method, and a retrospective reconstruction simulation to assess the dynamic keyhole method compared to the zero-filling and conventional keyhole methods for the task of lung tumor localization.

4.2.1 Lung tumor cine-MRI datasets and external respiratory signals

Two-dimensional (2D) coronal and sagittal cine-MR images for lung tumors were obtained in a 3 Tesla MRI (Skyra, Siemens Healthcare Erlangen, Germany). For lung tumor images, a true-FISP (true fast imaging with steady state free precession) MR pulse sequence was used to acquire 512 images, one every 308 ms. Typical MR imaging parameters were repetition time (TR)/echo time (TE) = 3.8/1.3 ms, acquisition time = 308 ms, flip angle = 45°, field of view = 380 × 380 mm^2, pixel size = 1.48 × 1.48 mm^2, slice thickness = 4 mm, bandwidth = 1500 Hz and image matrix = 256 × 256. The real-time position management (RPM) system (Varian Medical Systems, Palo Alto, USA) was used to monitor the subjects' abdominal respiratory motion to obtain external respiratory signals (25Hz). In this study, external respiratory signals obtained from the RPM were only utilized for the detection of respiratory displacement in a millimeter interval and respiratory phase (the inhalation and exhalation phase of each respiratory cycle) because the internal diaphragm visibility is often absent or limited on lung tumor images depending on lung tumor location.[27, 28]

Sixty four cine-MRI datasets with simultaneous external respiratory signals were obtained from nine lung cancer patients with informed consent under a local ethics board approved study. Seven patients had two separate imaging sessions on two different dates (pre and mid-treatment) and two patients had a single imaging session. Four datasets (coronal, sagittal, coronal and sagittal datasets) from the pre-treatment MRI session and another four datasets from the mid-treatment MR session were obtained. The images from the cine-MRI datasets were then converted to the full k-space datasets using the Fourier Transform.

4.2.2 Optimized library acquisition and real-time acquisition

The previous dynamic keyhole study (Lee *et al*, 2014)[32] acquired one or more full k-space datasets for each displacement bin (a millimeter bin width). However, this study simply remove the duplicates from the library but in a way that would mirror an online implementation, i.e. keeping the first and removing subsequent full k-space datasets that would fit into the bin. The library acquisition of the dynamic keyhole method was optimized to obtain the minimum number of full k-space datasets in five respiratory cycles. The optimized library acquisition is shown in Figure 4-1.

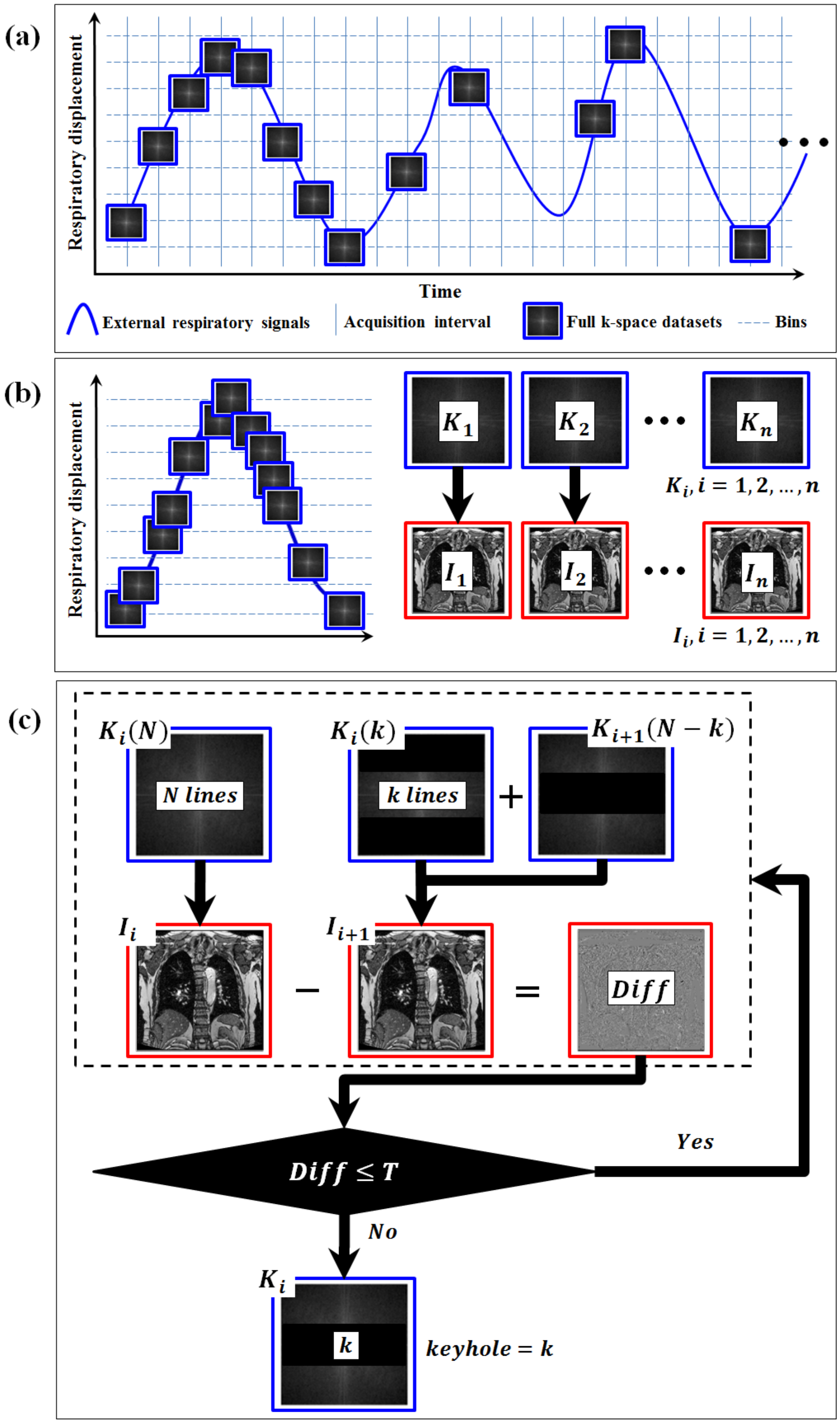
(a)
Respiratory displacement
Time
External respiratory signals
Acquisition interval
Full k-space datasets
Bins
(b)
Respiratory displacement
K_1
K_2
K_n
$K_i, i = 1, 2, \ldots, n$
I_1
I_2
I_n
$I_i, i = 1, 2, \ldots, n$
(c)
$K_i(N)$
N lines
$K_i(k)$
k lines
+
$K_{i+1}(N-k)$
I_i
−
I_{i+1}
=
$Diff$
$Diff \leq T$
Yes
No
K_i
k
keyhole = k

Figure 4-1. The optimized library acquisition of the dynamic keyhole method: (a) acquiring only one full k-space dataset at displacement bins (a set at 1 mm displacements), (b) sorting full k-space datasets into the displacement bins and (c) determining a keyhole size corresponding to the central k-space datasets of the full k-space datasets for the library.

Continuously obtained external respiratory signals (40 ms) and occasionally obtained full k-space datasets corresponding to acquisition intervals (308 ms) were utilized in this retrospective simulation. The three key steps are described below. Compared to the previous dynamic keyhole study,[32] Step 1 was modified to only allow one full k-space acquisition for each displacement bin and Step 3 was consequently simplified by processing one full k-space dataset for each displacement bin.

Step 1 (Figure 4-1 (a)): Displacement binning (a set at 1 mm displacements) using external respiratory signals (blue wave) was initiated at the first inhalation (or exhalation) of respiratory displacement. Then, full k-space datasets were obtained at acquisition intervals (horizontal dotted lines) and simultaneously allocated to displacement bins (vertical solid lines) where a displacement bin was similar to the displacement of the present external respiratory signals (blue wave). Only the first full k-space dataset for each displacement bin was obtained and subsequent full k-space datasets were not acquired to obtain the minimum number of full k-space datasets in five respiratory cycles.

Step 2 (Figure 4-1 (b)): The full k-space datasets were sorted by the displacement bins, expressed as K_i, where i=1,2,…,n, and also reconstructed using the 2D Fourier

Transform, expressed as I_i, where i=1,2,…,n. A tolerance T based on the pre-determined acceptable error fraction (δ)[32] was determined, where T is a fraction (δ) of the average pixel value of I_i on a pixel-by-pixel basis. To minimize the intensity variation of pixel values between images, the intensity range of each image is equalized to a minimum and maximum range from 0 to 255 for 8-bit images (i.e. stretching the histogram of the intensity range so a minimum value is 0 and maximum value is 255).

Step 3 (Figure 4-1 (c)): To determine a keyhole size (k) for $K_i(N)$, where k is the size of central k-space datasets (k=1,2,…,N) and N is 256 (the size of K_i), I_i of $K_i(N)$ was compared to I_{i+1} determined from $K_i(k) + K_{i+1}(N - k)$ in a loop of incremental k. In this study, I_i and I_{i+1} represent the present and next respiratory states and the difference between the two states indicates the maximum change of respiratory motion in a millimeter bin width. A keyhole size (k) for $K_i(N)$ was consequently determined when the average pixel of the difference ($Diff$) between corresponding images of I_i and I_{i+1} on pixel-by-pixel basis was below T. A small bin width obtaining more numbers of library datasets requires a long library acquisition time but results in a reconstructed image of better quality in a prospective implementation.

After this library acquisition, central k-space dataset acquisition began,[125] and a keyhole size central k-space dataset was conjunct with a library through matching the similar displacement bin utilizing external respiratory signals. The motion trajectory of the tumor is unknown, however the five breathing cycles used to create the library will give an array of image from which the most appropriate to match to the image can be selected.

4.3.3. Image reconstruction and quantification

For the retrospective image reconstruction simulation, sixty four k-space datasets were used with three methods: zero-filling, conventional keyhole and dynamic keyhole. Prior to central k-space dataset acquisition, the three methods were followed by the step 1 and 2 of library acquisition but for the step 3, I_i of $K_i(N)$ was compared to I_{i+1} determined from $K_i(k) + K_i(N - k)$ in a loop of incremental k, where $K_i(N - k)$ was continuously filled with zeros for the zero-filling method instead of $K_{i+1}(N - k)$ until the $Diff$ is below T. For the conventional keyhole method, $K_i(N - k)$ was continuously filled with a single k-space dataset from a middle of the first respiratory cycle.

After the retrospective image reconstruction, lung tumors were automatically contoured on original and reconstructed images using Otsu's method[128] which converts a gray scale image to a binary image in normalized intensity value that lies in the range [0, 1] and a region growing algorithm on the binary image. A single seed point on the tumor region was manually chosen on the first image of each dataset and the centroid of tumor contoured was used as a seed point of the next image until all images were segmented. The centroid of tumor motion was calculated using the mean of row and column positions where binary pixel values were equal to 1. The centroid and the area of contoured tumors were used for tumor motion and area, respectively.

The performance of three methods in real-time central k-space dataset acquisition was compared to full k-space dataset acquisition by quantifying (1) keyhole size required for central k-space datasets for constant image quality in the tolerance, indicating a small number corresponding to faster image acquisition; (2) intensity difference (i.e. intensity refers the numerical value of a pixel) in a constant keyhole size utilized in the dynamic keyhole method across the two other methods, indicating a small number corresponding to better image quality; and (3) the accuracy of tumor motion and area based on the images obtained in analysis (2). Qualitative outcomes were compared using examples of the original and reconstructed images with contoured tumors. Quantitative outcomes of keyhole size, intensity difference, tumor motion difference using the centroid of tumor contour and tumor area similarity were compared using the mean and standard deviation (STD), and a paired Student's t-test. The area similarity was quantified using the Dice index (i.e. $index = 2|A \cap B|/(|A| + |B|)$, where A is the original tumor area and B is the reconstructed tumor area).

4.3 Results

The performance of three methods measured in real-time dataset acquisition simulation varied in image acquisition, image quality and accuracy of tumor motion and area.

4.3.1 Image acquisition time with constant image quality

Figure 4-2 shows reconstructed images using different keyhole sizes across the three reconstruction methods to achieve constant image quality from the original image in the tolerance.

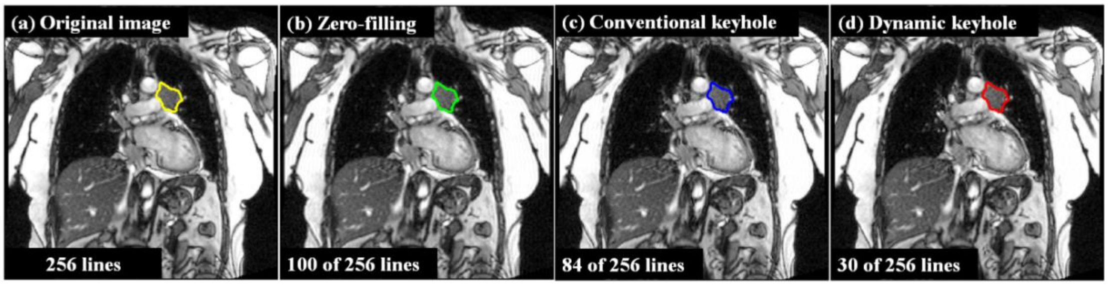

Figure 4-2. Reconstructed images of Patient 5 using different keyhole sizes required for constant image quality in the tolerance across three methods: (a) original image (256 lines) with full k-space data, (b) zero-filling reconstructed image, (c) conventional keyhole reconstructed image, and (d) dynamic keyhole reconstructed image. Lung tumors were contoured on the reconstructed images using different colors: (a) original image (yellow), zero-filling (green), conventional keyhole (blue) and dynamic keyhole (red).

To maintain the constant image quality from the original image of Patient 5, zero-filling, conventional keyhole, and dynamic keyhole required keyhole sizes of 100, 84, and 30 phase encoding lines, respectively.

Figure 4-3 shows the keyhole size for constant image quality for the sixty four datasets across the three methods.

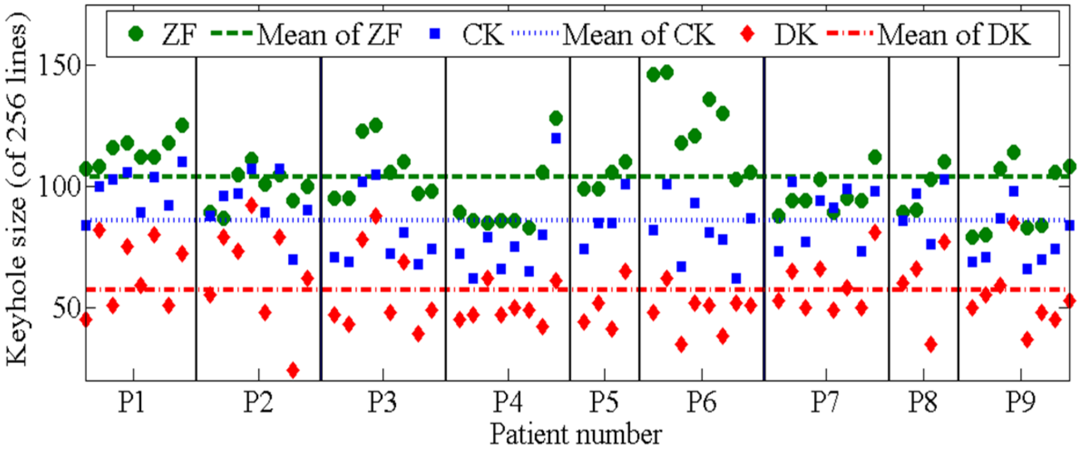

Figure 4-3. The keyhole size of three methods measured in central k-space dataset acquisition to produce constant image quality from the original image. The keyhole size measured in each dataset and over all datasets: (a) zero-filling (ZF, green circle and dashed line), conventional keyhole (CK, blue square and dotted line) and dynamic keyhole (DK, red diamond and dashed with dotted line). Four datasets (coronal, sagittal, coronal and sagittal) from the first MRI sessions in Patient 5 (P5) and 8 (P8), and eight datasets from the first and second MRI sessions in the other patients. A smaller keyhole size indicates faster image acquisition.

The keyhole size is the smallest in the dynamic keyhole method (red diamond) over all datasets and followed by the conventional keyhole method (blue square) and the zero-filling method (green circle). The keyhole size of the conventional keyhole method sometimes exceeded the keyhole size of the zero-filling method.

Table 4-1 shows the mean and STD of keyhole size from the sixty four datasets of coronal and sagittal image orientations across the three methods.

Table 4-1. The mean ± STD keyhole size (of 256 lines) of zero-filling, conventional keyhole and dynamic keyhole reconstruction methods from nine lung cancer patients.

Methods	Coronal Mean ± STD	Sagittal Mean ± STD	Average Mean ± STD
Zero-filling	100 ± 1	108 ± 2	104 ± 2
Conventional keyhole	83 ± 9	88 ± 8	86 ± 9
Dynamic keyhole	55 ± 12	59 ± 12	57 ± 12

Compared to the original image acquisition, the dynamic keyhole method required image acquisition speeds of about 68 ms (22% keyhole size compared to full k-space datasets), 104 ms (34%) in the conventional keyhole method and 126 ms (41%) in the zero-filling method for constant image quality within the tolerance. The reduction in the keyhole size between the dynamic keyhole and both the zero-filling and conventional keyhole methods were statistically significant with a $p < 0.0001$ in both cases. By having a keyhole size of 57 out of 256 lines, the dynamic keyhole method can achieve 78% faster image acquisition than original cine-MR image acquisition, in addition to being 45% and 33% faster than zero-filling and conventional keyhole image acquisition time, respectively.

4.3.2 Varying image quality with constant keyhole size

MR images of the three different reconstruction methods using a constant keyhole size of 30 lines in k-space are shown in Figure 4-4. Three reconstructed images were compared to the original image.

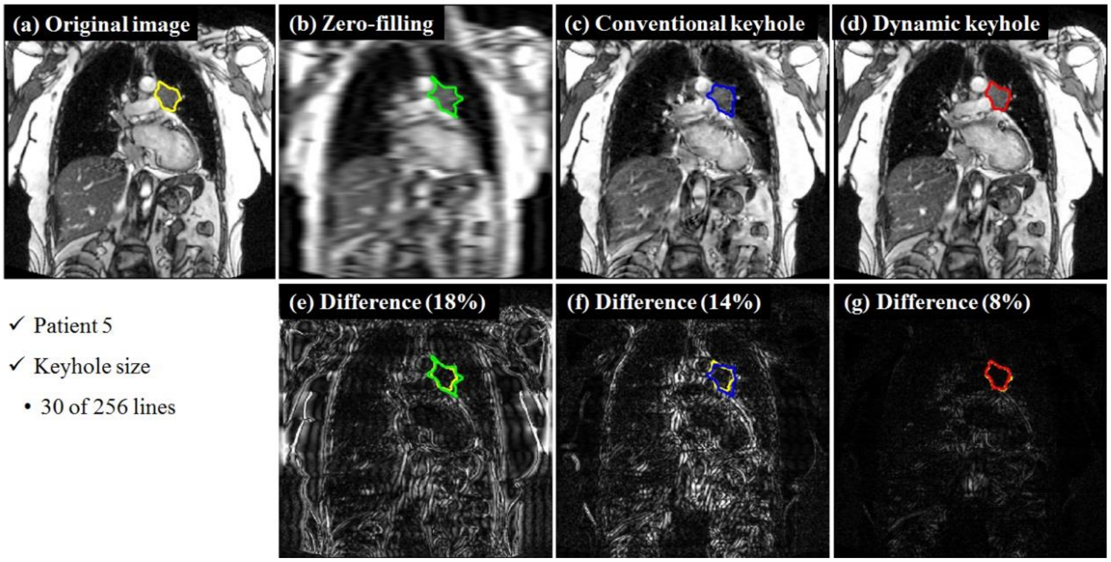

Figure 4-4. Reconstructed MR images of (a) original full k-space image, as well as reconstructed MR images with a constant keyhole size of 30 of 256 phase encoding lines for (b) zero-filling, (c) conventional keyhole and (d) dynamic keyhole. (e), (f) and (g) display the difference (and percentage of difference) between original image and the reconstructed zero-filling, conventional keyhole, and dynamic keyhole images, respectively. Lung tumors were contoured on the reconstructed images in different colors: (a) original image (yellow), zero-filling (green), conventional keyhole (blue) and dynamic keyhole (red) methods.

The reconstructed image was entirely blurred in the zero-filling method (see Figure 4-4(b)) and it was partially blurred at organ edges, such as diaphragm and heart in the conventional keyhole method (see Figure 4-4(c)), however, an image with fine and sharp organ edges was reconstructed in the dynamic keyhole method (see Figure 4-4 (d))

Table 4-2 shows the mean and STD of the intensity difference between the original and the reconstructed images from the sixty four datasets.

Table 4-2. Averaged intensity differences of the MR image and tumor itself between the original and the zero-filling, conventional keyhole and dynamic keyhole reconstructed images.

Methods	Image intensity difference Mean ± STD	Tumor intensity difference Mean ± STD
Zero-filling	14.2 ± 2.9	11.8 ± 4.9
Conventional keyhole	13.0 ± 2.0	13.1 ± 5.3
Dynamic keyhole	11.6 ± 2.0	11.6 ± 4.5

Compared to the original MR image, dynamic keyhole improved the image intensity difference by 2.6% ($p < 0.0001$) and 1.4% ($p < 0.0001$) over zero-filling and conventional keyhole respectively. Compared to the original image, dynamic keyhole improved the tumor intensity difference by 0.2% ($p = 0.53$) and 1.5% ($p < 0.0001$) over zero-filling and conventional keyhole respectively.

4.3.3 Accuracy of tumor motion and area with constant keyhole size

The performance of the three methods using the constant keyhole size of the dynamic keyhole method was compared for lung tumor motion and area. Figure 4-5 shows examples of tumor motion and differences from Patient 6 who had substantial tumor motion.

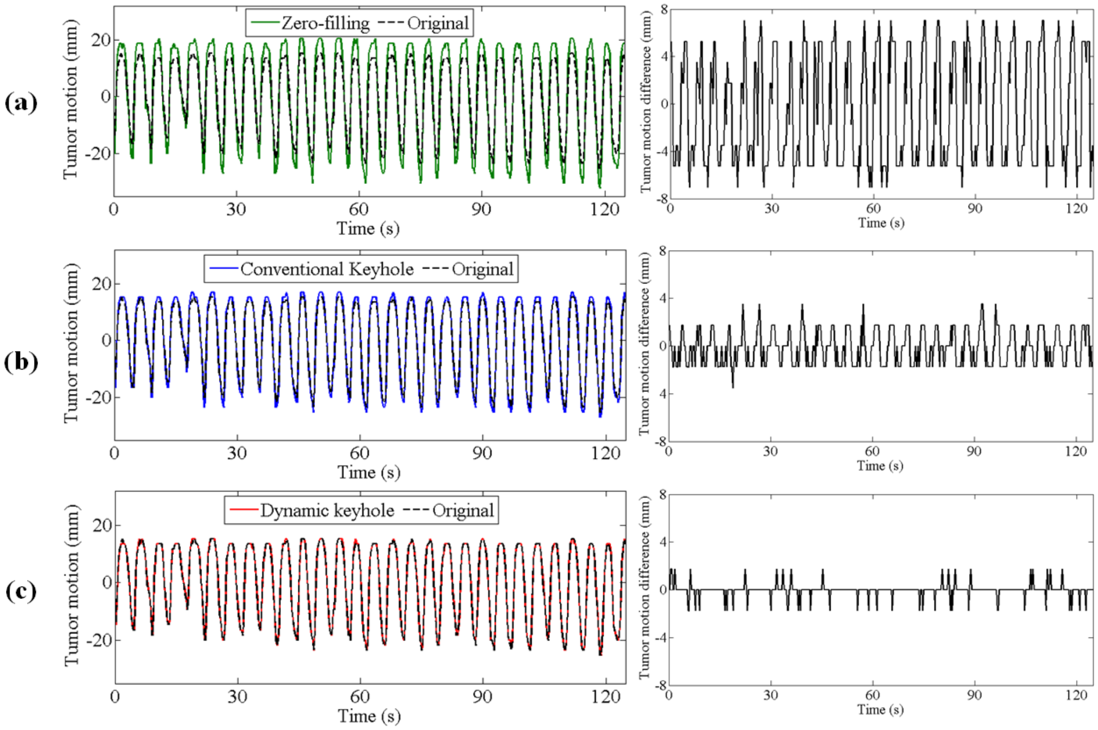

Figure 4-5. The tumor motion of original (black dashed) and reconstructed images using a constant keyhole size based on the keyhole size of the dynamic keyhole method. (a) Zero-filling (green line), (b) conventional keyhole (blue line) and (c) dynamic keyhole (red line), and tumor motion difference (black line) between the two tumor motions from the original and reconstructed images.

The dynamic keyhole tumor motion (red line) was visually comparable to the original tumor motion (black dashed) in Figure 4-5 (c) but the conventional keyhole tumor motion (blue line) was a couple of data points larger in Figure 4-5 (b) and several data points larger in the zero-filling tumor motion (green line) in Figure 4-5 (a). In terms of tumor motion accuracy, the tumor motion difference (black line), was minimal in the dynamic keyhole method compared to the conventional keyhole and zero-filling methods.

Figure 4-6 illustrates examples of tumor areas contoured on the original and reconstructed images using a constant keyhole size based on the keyhole size of the dynamic keyhole method from Patient 5.

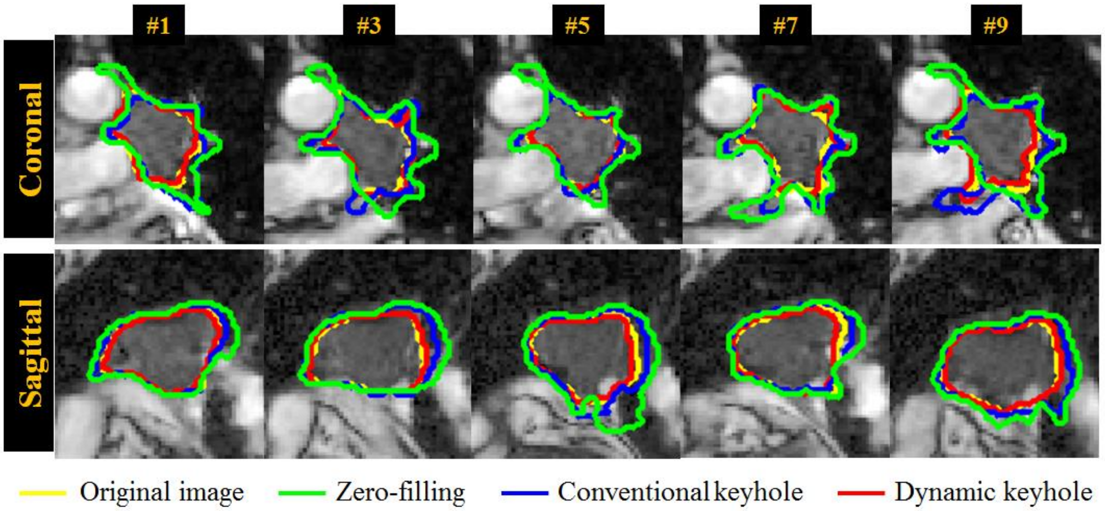

Figure 4-6. Tumor areas contoured on the original and reconstructed images using constant keyhole size: original image (yellow), zero-filling (green), conventional keyhole (blue) and dynamic keyhole (red). Image number (#) indicates the sequential order of MR images.

The dynamic keyhole tumor areas (red) were visually comparable to the original tumor areas (yellow) in all the illustrated images. The zero-filling tumor areas (green) were considerably larger than the original tumor areas and the conventional keyhole tumor areas were slightly larger than the original tumor areas but it was often considerably larger shown in #3 and #9 of coronal images and #5 and #9 of sagittal images.

Table 4-3 gives the overall of tumor motion difference using the centroid of tumor contour and area similarity using Dice index in the mean and STD from sixty four datasets.

Table 4-3. The tumor motion difference and area similarity of zero-filling, conventional keyhole and dynamic keyhole images from original image in the mean and STD from sixty four datasets.

Methods	Tumor motion difference (mm) Mean ± (STD)	Tumor area difference (%) Mean ± (STD)
Zero-filling	2.6 ± 4.7	9.6 ± 3.4
Conventional keyhole	1.1 ± 2.8	7.2 ± 3.0
Dynamic keyhole	0.3 ± 1.8	0.2 ± 1.2

Compared to the original tumor motion, dynamic keyhole improved tumor motion difference by 2.3 mm ($p < 0.0001$) and 0.8 mm ($p < 0.0001$) over zero-filling and conventional keyhole, respectively. Compared to the original tumor area, dynamic keyhole improved tumor area similarity by 0.52 ($p < 0.0001$) and 0.76 ($p < 0.0001$) over zero-filling and conventional keyhole, respectively. Compared to the original tumor motion, the accuracy of the dynamic keyhole tumor motion was measured at 99.6% and the accuracy of the dynamic keyhole tumor area was measured at 98.0%. The tumor motion difference and area similarity were minimized in the dynamic keyhole method compared to the other two methods.

4.4 Discussion

In this study, we evaluated the dynamic keyhole method[125] which utilizes a library of previously acquired peripheral k-space datasets corresponding to multiple respiratory states that are combined with keyhole size central k-space datasets at the closest respiratory state using external respiratory information. Using the dynamic keyhole method, we demonstrated the accuracy of the tumor motion and area as a function of acceleration factor through sixty four lung tumor image dataset reconstruction.

Similar to the previous study of healthy volunteer dataset reconstruction,[125] the dynamic keyhole method achieved 78% faster image acquisition than original image acquisition with improved image quality, which is essential for tumor imaging in the presence of respiratory-induced tumor motion. As shown in Figure 4-3, there was some variation in keyhole size across image orientations (i.e. coronal and sagittal) and the patients; this was due to factors such as patient size, the magnitude of breathing motion, and breathing regularity in the dynamic keyhole method. The variation of keyhole size can cause different imaging speeds over image orientations and patients but this can be a trade-off between temporal and spatial resolution. The relationship between keyhole size and image size due to variations of patient size and image orientation will be investigated to determine an optimal keyhole size for variable image size in a future study.

This study assessed the intensity difference between original and reconstructed images shown in Table 4-2. An intended average intensity difference was a fraction (10%) of the average pixel value but the measured intensity difference of the dynamic keyhole method was 1.6% greater than the intended average intensity difference due to the limited coverage of respiratory displacements in the library, which obtained from at the beginning of five respiratory cycles. In order to improve the limitation of the respiratory displacement coverage, library reacquisition or real-time update could be required if the breathing changes with a large breath or baseline shift, where there is no corresponding library dataset during treatment.

The accuracy of tumor motion and area was quantified and analyzed using the lung tumors directly measured from reconstructed images using auto-contouring. A consistent tumor auto-contouring condition was used for both original and reconstructed images in order to investigate the dependency of reconstructed images within intensity difference in Table 4-2. This study demonstrated that the dynamic keyhole tumors compared to the original tumors are consistent with 99.6% accuracy for tumor motion and 98% accuracy for tumor area in Table 4-3. This provides evidence that the dynamic keyhole is a promising MR image reconstruction technique applicable for tumor imaging in thoracic and abdominal regions.

Compared to the previous library acquisition of the dynamic keyhole method, the new optimized library acquisition reduced the number of full k-space datasets by 72% whilst maintaining the reconstruction performance of central k-space dataset acquisition in Table 4-1. To optimize the library acquisition of dynamic keyhole method in Figure 4-1, a number of full k-space dataset acquisitions were skipped at displacement bins in five respiratory cycles, possibly acquiring well-distributed library datasets at the displacement bins while controlling a library acquisition time and a respiratory bin width, when utilizes a respiratory-triggering technique.[129] For example, more numbers of library datasets in sub-millimeter bin width could be acquired for better image quality to consider the size of human subjects and their respiratory displacement and period.

The relationship between the raw (k-space) data and the resultant image is the Fourier transformation which enables to capture (or revert) the measurement of a single net magnetization vector located somewhere within the space in which phase and frequency encoding gradients are applied. In addition, temporal resolution (i.e. the duration of time for the acquisition of a single image) depends on fields of view and the number of data points across an image along the frequency (i.e. each transverse magnetization) and phase (i.e. location) encoding directions. Thus, this study utilized the k-space data (i.e. Fourier transformed MR images) in a retrospective reconstruction simulation and the number of k-space data points was measured to demonstrate the reduction of imaging speed, corresponding to the reduction of data points. However, the dynamic keyhole method should be prospectively tested in an experimental implementation prior to clinical uses.

Real-time tracking[6, 36, 130] has been developed to account for tumor motion variability and this can improve the uncertainty of the tumor motion variability, but the real-time tracking using lung tumor MR images[81, 122, 131] is still under investigation due to a considerably long acquisition time. In addition, real-time tracking requires measuring tumor positions in near real-time and predicting tumor positions to allow for beam repositioning synchronized with a continuously moving tumor. However, the response of the beam repositioning to a tumor position cannot occur instantaneously.[4] A prospective implementation of the dynamic keyhole method would allow for more accurate motion prediction calculation to mitigate the inherent system latency, an accurate tumor position can be predicted in shorter intervals due to that accuracy degrades rapidly with longer delay intervals.[84, 116]

The dynamic keyhole method, compared to iterative reconstruction can neglect MR image reconstruction time due to excluded computationally-intensive iterative calculations. Compared to undersampling methods filling zeros at unmeasured points,[96, 99, 100] MR images of full k-space datasets combined central k-space datasets with library at an appropriate displacement bin can be utilized to directly measure lung tumors on dynamic keyhole reconstructed images in sufficient accuracy of tumor motion and area. The dynamic keyhole method could be applicable for real-time tumor imaging without an extra piece of equipment in a number of radiotherapy systems integrated with MRI.[79, 88, 90, 120, 121] In addition, this could be applicable for real-time 3D and 4D MRI acquisition to overcome the issue of out-of-plane motion in 2D MRI. In clinical implementation, the dynamic keyhole method could reduce scan times without compromising image quality for real-time thoracic and abdominal tumor motion tracking while possibly utilizing a variety of MR compatible respiratory sensors such as physiological measurement unit (Siemens Healthcare Erlangen, Germany) for cardiac and chest motion, bellows belts (Philips Healthcare, Best, The Netherlands) for chest and abdominal motion, and active breathing coordinator (Elekta Oncology Systems Ltd, Crawley, West Sussex, UK) for air volume.

The dynamic keyhole method can be applied to MRI-guided tumor tracking required that an image of sufficient quality be utilized for real-time tumor imaging, a technique offering both fast and quasi-continuous image acquisition for MR image guidance.

4.5 Conclusions

In this study, the dynamic keyhole method utilized respiratory signals to improve lung cancer patient MR images in the presence of respiratory-induced tumor motion, leading to a 78% reduction of the time required for a full k-space acquisition method for lung tumor MR imaging, whilst maintaining image quality. In addition, this was the first study in which the dynamic keyhole MR image reconstruction was applied to lung tumor imaging. Our results demonstrate the dynamic keyhole method as a useful technique for image-guided radiation therapy and MRI-guided radiotherapy that requires real-time tumor monitoring in the thoracic and potentially abdominal regions.

Chapter 5: Audiovisual Biofeedback Improves Cine-Magnetic Resonance Imaging Measured Lung Tumor Motion Consistency

A version of this chapter has been published: Lee D, Greer B P, Ludbrook J, Arm J, Hunter P, Pollock S, Makhija K, O'Brien T R, Kim T and Keall P, "Audiovisual Biofeedback Improves Cine-Magnetic Resonance Imaging Measured Lung Tumor Motion Consistency" Int J Radiat Oncol Biol Phys, ***94*** *(3): 628 (2016), http://dx.doi.org/10.1016/j.ijrobp.2015.11.017.*

ABSTRACT

Purpose: To assess the impact of an audiovisual (AV) biofeedback on intra- and inter-fraction tumor motion for lung cancer patients.

Methods and Materials: Lung tumor motion was investigated in nine lung cancer patients who underwent a breathing training session with AV biofeedback prior to two 3T MRI sessions. The breathing training session was performed to allow patients to become familiar with AV biofeedback, which utilizes a guiding wave customized for each patient based on a reference breathing pattern. In the first MRI session (pre-treatment), 2D cine-MR images with (1) free breathing (FB) and (2) AV biofeedback were obtained and the second MRI session was repeated within three to six weeks (mid-treatment). Lung tumors were directly measured from cine-MR images using an auto-segmentation technique; the centroid and outlier motions of the lung tumors were measured from the segmented tumors. FB and AV biofeedback were compared using several metrics: intra- and inter-fraction tumor motion consistency in displacement and period, and the outlier motion ratio.

Results: Compared to FB, AV biofeedback improved intra-fraction tumor motion consistency by 34% in displacement ($p=0.019$) and by 73% in period ($p<0.001$). Compared to FB, AV biofeedback improved inter-fraction tumor motion consistency by 42% in displacement ($p<0.046$) and by 74% in period ($p=0.005$). Compared to FB, AV biofeedback reduced the outlier motion ratio by 21% ($p<0.001$).

Conclusions: These results demonstrated that audiovisual biofeedback significantly improved intra- and inter-fraction lung tumor motion consistency for lung cancer patients. These results demonstrate that AV biofeedback can facilitate consistent tumor motion, which is advantageous towards achieving more accurate medical imaging and radiation therapy procedures.

5.1 Introduction

Breathing variations[27, 132-135] can cause image artifacts in 4-dimensional CT (4D-CT) images,[136] utilized in radiotherapy treatment planning and lead to a greater variation in tumor motion between treatment planning and treatment delivery.[29, 30] In addition, breath-to-breath (intra-fraction) variations compromises the quality of radiation delivery, as it causes an averaging or blurring of dose distribution over the path of the tumor motion; whilst day-to-day (inter-fraction) variations cause a shift of the dose distribution.[4]

Breathing management techniques utilizing patient respiratory signals such as respiratory gating,[51] training[52] and breath-holds[53] have been developed to address intra-fraction breathing variability. However, inter-fraction variability from the daily changes of patient breathing is still prominent[51, 137] and this variability is larger than intra-fraction variability.[27, 132, 133] Tumor motion tracking has also been developed to account for tumor motion variability. This technique can decrease the uncertainty of respiratory-induced tumor motion; however, non-invasive, markerless lung tumor tracking is not in widespread use.[5, 50]

AV biofeedback,[51, 52, 73, 74, 76, 138] an interactive personalized breathing guidance system, has been developed to minimize breathing variability. AV biofeedback utilizes an external respiratory signal from a real-time position management (RPM) system (Varian, Palo Alto, USA) to track patient breathing in real-time. Previous AV biofeedback results have demonstrated that the breathing consistency of external and internal surrogates has been improved[10,11,16,76] whilst maintaining a robust correlation between external and internal breathing motion.[139] However, AV biofeedback results on tumor motion have been less conclusive,[78,140] with additional further investigation strongly suggesting that patient compliance and performance with AV biofeedback improve with time.[141] In addition, the variation of lung tumor in outlier motion has not been matched to treatment margins.

In this study, we introduced a novel approach of AV biofeedback for non-small cell lung cancer (NSCLC) patients, involving a breathing training session to obtain a guiding wave customized for each patient based on a reference breathing pattern with AV biofeedback and utilizing the guiding wave over two 3T MRI sessions. This study is the first investigation of the impact of AV biofeedback on lung tumor motion consistency, both intra- and inter-fractionally, directly measured from cine-MR images.

5.2 Methods and Materials

5.2.1 Patients

Nine NSCLC patients (age: 25-74) with a stage varying from I to III of any histology to be treated using radiotherapy were enrolled in an ethics approved protocol. Excluded patients had the presence of metallic objects such as surgical clips, surgery metalware and pacemakers. This study was designed with a breathing training session followed by two MRI sessions across different dates (pre- and mid-treatment). The breathing training session was scheduled on the same day of the first MRI session and the second MRI session was then repeated within three to six weeks at approximately the mid-point of the radiation treatment.

5.2.2 Audiovisual biofeedback

A breathing training session was performed to allow patients to become familiar with a guiding wave; an average of 10 breathing cycles was calculated using a Fourier Series fit,[74] customized in the displacement and period of respiratory cycles,[142] and presented to them on the AV biofeedback breathing guide. Figure 5-1(a) shows the workflow of operation of AV biofeedback. Patient breathing is tracked in real-time using RPM, which monitors the up (as they inhale) and down (as they exhale) motion of the gray marker-block positioned on the patient's abdomen. The guiding wave was displayed on the patient's visual display in inhale and exhale breathing limits as the gray horizontal lines which frame the blue wave. The patient then adjusts their breathing such that a gray marker-block on their visual display stays within the breathing limits and traces the motion of the guiding wave.

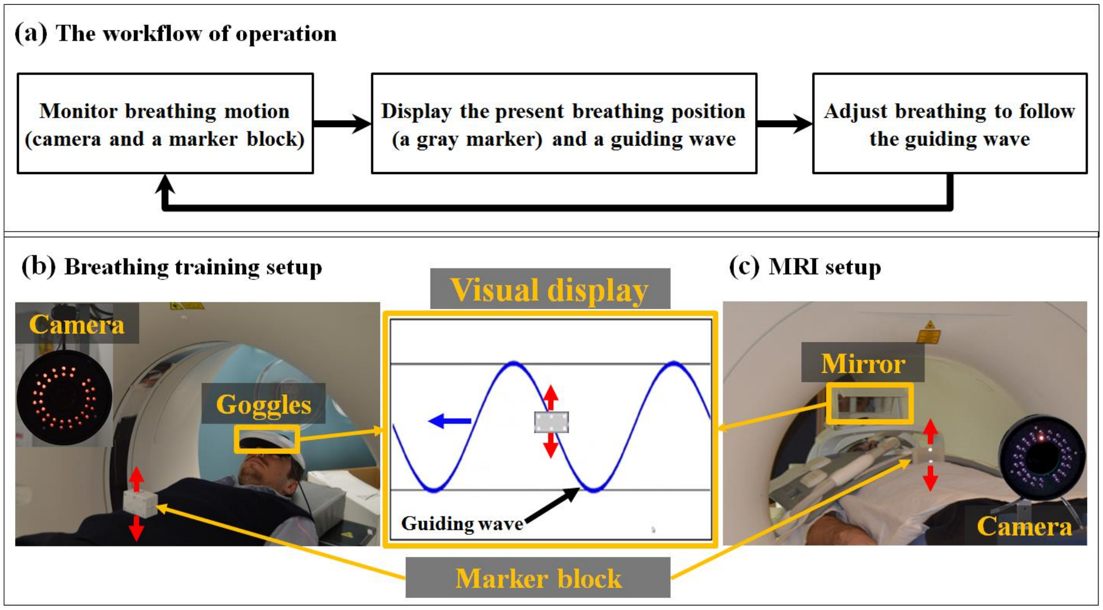

Figure 5-1. The workflow of operation and experimental setups of AV biofeedback. (a) The workflow of operation, (b) breathing training setup for a breathing training session and (c) MRI setup for two MRI sessions.

Two experimental setups of AV biofeedback for a breathing training session (see Figure 5-1(b)) used a ceiling mounted RPM and display goggles. For the MRI setup, a mobile RPM and a mirror-display setup overlooking an MR-compatible projection screen[76, 138] (see Figure 5-1(c)) was utilized for the two MRI sessions.

5.2.3 Breathing training session with AV biofeedback

Prior to MRI sessions, each patient participated in a breathing training session with AV biofeedback (no imaging performed) to allow them to become familiar the

AV biofeedback breathing guidance and obtain a guiding wave to be used in two MRI sessions.

This session was to allow the patient to practice their breathing for approximately 30 minutes to an hour, which included the acquisition of up to three guiding waves and breathing practices. Once a guiding wave was acquired, patients were guided by AV biofeedback for 5 – 10 minutes in a practice session. After each breathing practice, based on a discussion with the patient, the displacement and period of the guiding wave was modified to make it more comfortable before allowing the patient to practice with the modified guiding wave. This was repeated 2 – 3 times until the patients were comfortable using the guiding wave. At the end of a breathing training session, the guiding wave the patient was most comfortable with was chosen as was used for the subsequent MRI sessions.

5.2.4 Magnetic resonance imaging with AV biofeedback

Two-dimensional (2D) coronal and sagittal cine-MR images were obtained in a 3 Tesla MRI (Skyra, Siemens Healthcare Erlangen, Germany). For thoracic imaging, a true-FISP (true fast imaging with steady state free precession) MR pulse sequence was used to acquire 512 images per 2D cine-MR imaging every 308 ms. Typical MR imaging parameters were repetition time (TR)/echo time (TE) = 3.8/1.3 ms, flip angle = 45°, field of view = 380 × 380 mm^2, pixel size = 1.48 × 1.48 mm^2, slice thickness = 4 mm, bandwidth = 1500 Hz, and image matrix = 256 × 256.

Coronal and sagittal images were obtained at different positions (center of the tumor region) and times (coronal followed by sagittal) with (1) free breathing (FB) and (2) AV biofeedback across the first and second MRI sessions. Hence, tumor motion varied between coronal and sagittal image datasets. At the beginning of an

MRI session with AV biofeedback, the guiding wave was loaded to display on a patient screen in Figure 1(b). Eight datasets per patient (two image datasets (coronal and sagittal) × two breathing types (FB and AV)) were obtained from two MRI sessions; however, only four datasets were obtained from the first MRI session of Patient 5 and 8, as the patients withdrew from study before the second MRI session.

5.2.5 Tumor auto-segmentation

Tumor motion was directly measured from cine-MR images through auto-segmentation in order to consider the changes in displacement and shape. The auto-segmentation was performed in the following steps:

1. A single seed point on the tumor region was manually chosen on the first image of each dataset and an arbitrary image pixel matrix (i.e. 9×9) surrounding the single seed point was chosen but a smaller (or bigger) matrix size can be used, depending on tumor size.
2. For the range of image intensity (threshold), an average of three minimum and maximum pixel values of the arbitrary image pixel matrix was computed to filter tumor image intensity within the threshold.
3. Otsu's method[128] was used to convert a gray scale image to a binary image in normalized image intensity value that lies in the range [0, 1].
4. The tumor was segmented by a region growing algorithm[143] with the seed point on the binary image. The centroid of tumor motion was calculated using the mean of row and column positions where binary pixel values were equal to 1. In the next image, the tumor was segmented using the present centroid as a seed point until all binary images were segmented. All segmented tumors

were visually inspected to assess auto-segmentation. If an abrupt motion occurred, a new seed point would be chosen again; but this did not happen for all datasets.

An in-house tumor auto-segmentation was implemented in Matlab version 8.2 (The MathWorks, Natick, USA) and used for 2D coronal and sagittal cine-MR image datasets.

5.2.6 Tumor motion consistency

For the impact of the use of AV biofeedback, tumor motion consistency was investigated in (1) intra-fraction tumor motion in each dataset and (2) inter-fraction tumor motion over two datasets from the first and second MRI sessions. For the intra-fraction tumor motion consistency, the centroid of tumor motion was separated into individual cycles of a peak to peak (or a trough to trough), excluding incomplete data, and the root mean square error (RMSE) of a cycle to cycle in displacement[74] was computed whilst comparing the average cycle of the individual cycles with each individual cycle. RMSE in period was also computed from each individual cycle.

For the inter-fraction tumor motion consistency, RMSE of a session to session in displacement and period was computed by comparing two average cycles of the two datasets. In order to match tumor motion variability to outlier motion, each segmented tumor was accumulated on a pixel-by-pixel basis over the path of all segmented tumors in each dataset and then over two datasets at their center. Then, the value of the pixels (frequency), how many times the tumor passed and the number of pixels (distribution) where the tumor passed more than once were quantified. For example, the frequency of all the pixel values can be the same as the number of segmented tumors if no tumor motion and shape changes occur. However, a wide spread distribution in various frequencies, directly connected to treatment margins can be expected if a large baseline shift and displacement change of tumor motion occurs.[4, 144] To evaluate outlier motion caused by baseline shifts and irregular breathing, we computed the ratio of the distribution in which the tumor was found 5% or more of the time to the total distribution encompassed by the tumor motion. This ratio, referred to henceforth as the outlier motion ratio, was computed for all of the patient datasets for FB and AV. Quantitative statistical comparison between AV biofeedback and FB was determined using RMSE in displacement and period for intra-fraction tumor motion consistency, and RMSE in displacement and period, and the outlier motion ratio for inter-fraction tumor motion consistency using a paired Student’s t-test.

5.3 Results

Figure 5-2 shows the nine lung tumors delineated by auto-segmentation on coronal and sagittal cine-MR images. Segmented tumors at the end of exhalation (EE) and inhalation (EI) were chosen for each patient.

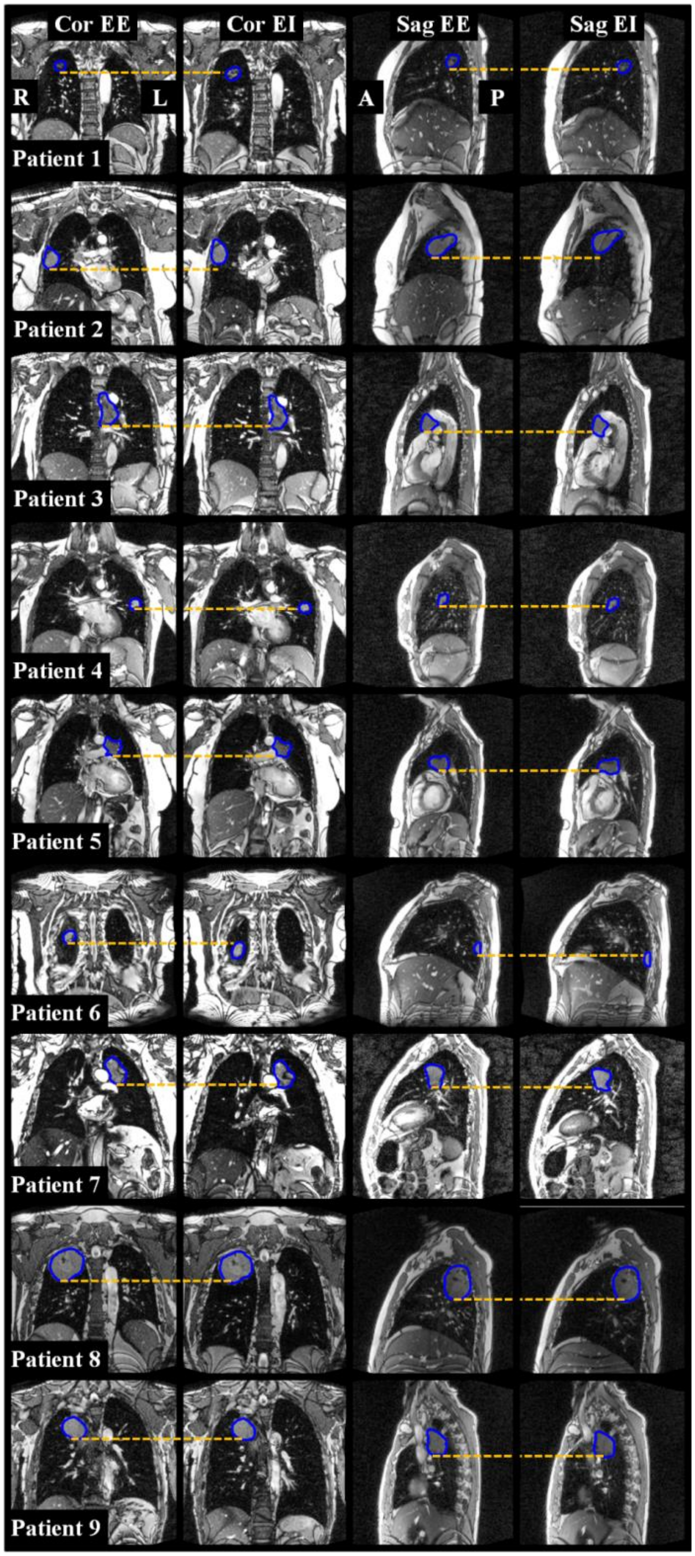
Cor EE
Cor EI
Sag EE
Sag EI
R
L
A
P
Patient 1
Patient 2
Patient 3
Patient 4
Patient 5
Patient 6
Patient 7
Patient 8
Patient 9

Figure 5-2. The tumor delineation (blue line) of nine lung cancer patients. Segmented tumors at EE and EI were chosen for each patient and an orange dotted-line highlights the changes in tumor displacement.

The location of the identified tumors (blue line) varied across patients; (1) four tumors (Patient 3, 4, 5 and 7) were on the left lung and five (Patient 1, 2, 6, 8 and 9) were on the right lung, (2) five (Patient 1, 5, 7, 8 and 9) were on the upper lung and four (Patient 2, 3, 4 and 6) were on the middle lung, (3) and three (Patient 1, 4 and 6) were isolated from organs but the other six (Patient 2, 3, 5, 7, 8 and 9) were connected to (or between) organs. In addition, tumor shape varied on different coronal and sagittal image orientations; (1) two (Patient 1 and 4) were mostly the same shape on both image orientations but the other seven (Patient 2, 3, 5, 6, 7, 8 and 9) were considerably different between image orientations. All tumors moved in the direction of respiratory motion apart from Patient 2 where the tumor attached to the chest wall moved superiorly during expiration.

5.3.1 Intra-fraction tumor motion consistency

Figure 5-3 shows a comparison of tumor motion between FB and AV biofeedback. Four superior-inferior (SI) tumor displacements indicate the different combinations of breathing type and MRI session in Patient 4 and 6.

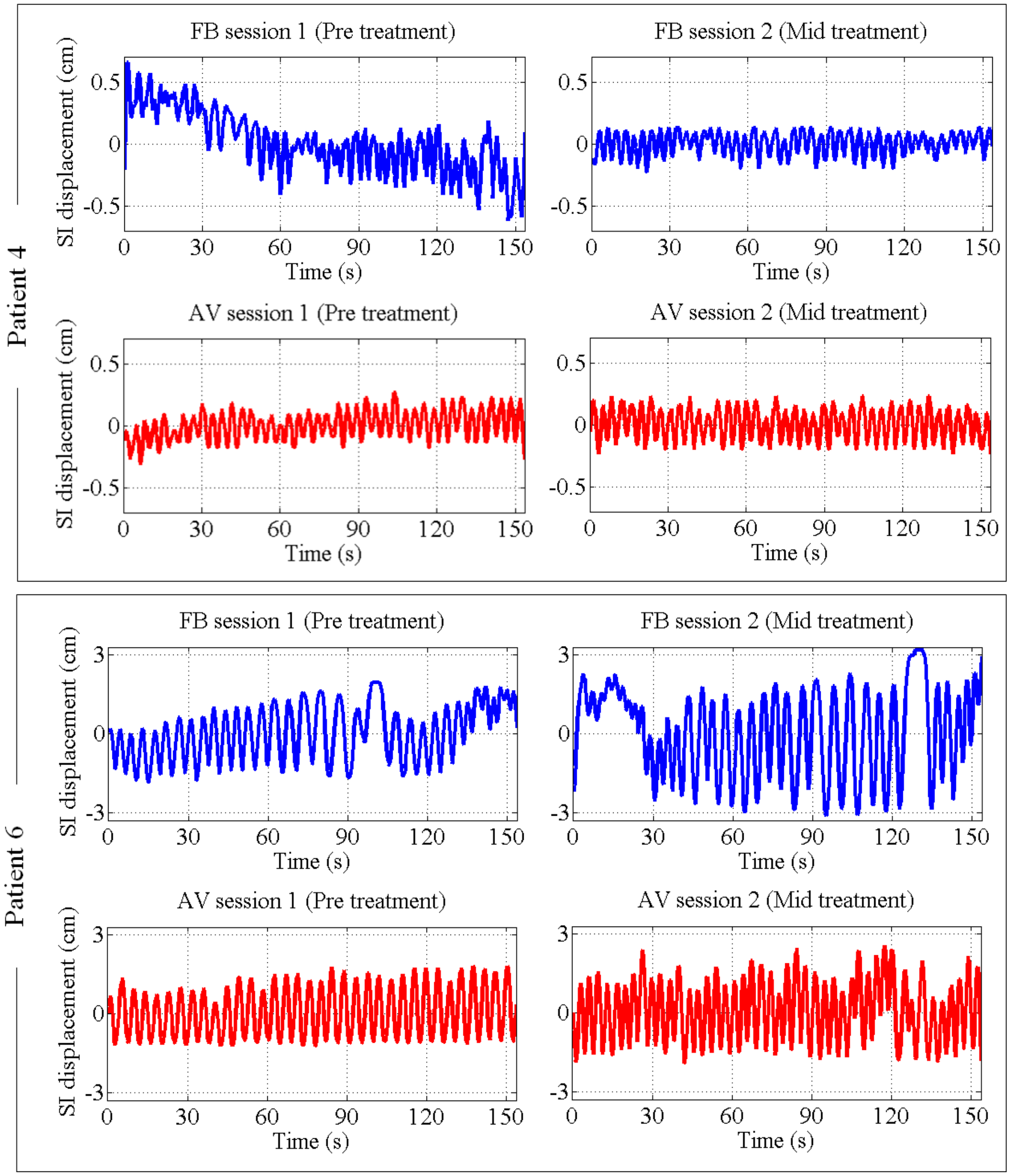

Figure 5-3. SI tumor displacement (cm) of Patient 4 and 6 between FB and AV biofeedback measured from coronal image datasets and organized by breathing type and MRI session. Extreme displacements were either a function of continuous drift with FB in Patient 4 or a drift stable and breath hold with FB in Patient 6.

The tumor of Patient 4 moved in a small range of ±0.5 cm, whilst a large range of ±3 cm was found in Patient 6. In Patient 4, the baseline of tumor displacement continuously drifted over the entire FB session 1 and the tumor displacement of FB session 2 was more regular but smaller, whilst the regularity of tumor displacement was improved over AV biofeedback sessions. In Patient 6, regular tumor displacement was found in the AV biofeedback sessions, compared to irregular tumor displacement in both FB sessions due to a drift stable and breath hold.

Table 5-1 shows the intra-fraction tumor motion consistency results with FB and AV biofeedback in RMSE of displacement and period.

Table 5-1. Results for intra-fraction tumor motion consistency in RMSE of displacement and period. A smaller number of RMSE indicates more consistent tumor motion. P: Patient, Cor: Coronal, Sag: Sagittal, S: MRI Session and *p*: a paired Student's t-test between FB and AV biofeedback (coronal and sagittal together).

Patients		RMSE displacement (cm)				RMSE period (s)			
		FB Cor	FB Sag	AV Cor	AV Sag	FB Cor	FB Sag	AV Cor	AV Sag
P1	S1	0.25	0.14	0.16	0.10	1.22	0.53	0.66	0.32
	S2	0.08	0.07	0.14	0.12	0.54	0.32	0.33	0.36
P2	S1	0.07	0.04	0.07	0.06	0.72	0.95	0.49	1.02
	S2	0.07	0.05	0.09	0.04	0.73	0.76	0.24	0.38
P3	S1	0.07	0.06	0.06	0.07	0.50	0.38	0.38	0.53
	S2	0.06	0.09	0.07	0.05	0.26	0.50	0.22	0.28
P4	S1	0.18	0.05	0.05	0.03	1.38	1.38	0.22	0.23
	S2	0.04	0.04	0.04	0.03	0.49	0.46	0.21	0.16
P5	S1	0.05	0.08	0.04	0.03	0.47	0.32	0.36	0.22
P6	S1	0.50	0.29	0.23	0.18	1.38	0.96	0.19	0.28
	S2	0.99	0.51	0.45	0.32	1.83	0.48	0.36	0.28
P7	S1	0.12	0.08	0.08	0.05	1.23	2.11	0.25	0.26
	S2	0.13	0.16	0.04	0.08	1.33	1.70	0.23	0.26
P8	S1	0.07	0.03	0.03	0.03	1.42	4.93	0.23	0.33

P9	S1	0.03	0.01	0.03	0.02	1.04	0.53	0.24	0.18
	S2	0.03	0.04	0.03	0.03	1.06	0.67	0.18	0.22
Average		0.20	0.13	0.12	0.09	0.98	1.34	0.30	0.39
p		= 0.019				< 0.001			

RMSE displacement of intra-fraction tumor motion varied with AV biofeedback between 0.02 and 0.45 cm, but it was larger for FB, with RMSE displacement between 0.03 and 0.99 cm. Only two patients with AV biofeedback had more than 0.1 cm in RMSE displacement, compared to four patients with FB. In addition, RMSE period with AV biofeedback was between 0.16 s and 1.02 s, which were smaller than FB, with RMSE period between 0.26 s and 4.93 s. Intra-fraction RMSE values were significantly reduced by 34% in displacement (p=0.019) and by 73% in period (p<0.001) when AV biofeedback was utilized whilst there wasn't any difference in mean displacement and period with FB and AV biofeedback.

5.3.2 Inter-fraction tumor motion consistency

Table 5-2 shows the inter-fraction tumor motion consistency results with FB and AV biofeedback in the RMSE of displacement and outlier motion ratio. The inter-fraction tumor motion consistency in period was increased by 74% in period (p = 0.005).

Table 5-2. Results for inter-fraction tumor motion consistency in RMSE of displacement and outlier motion ratio. A smaller number indicates more consistent tumor motion.

Patients	RMSE displacement (cm)				Outlier motion ratio (%)			
	FB Cor	FB Sag	AV Cor	AV Sag	FB Cor	FB Sag	AV Cor	AV Sag
P1	0.07	0.05	0.06	0.03	40	39	35	31
P2	0.13	0.09	0.06	0.06	30	31	29	23

P3	0.05	0.05	0.02	0.05	32	40	26	42
P4	0.03	0.03	0.02	0.02	50	38	25	24
P6	0.44	0.21	0.22	0.11	35	42	25	29
P7	0.06	0.03	0.05	0.03	39	36	33	35
P9	0.01	0.01	0.01	0.01	36	42	33	29
Average	0.11	0.07	0.06	0.04	37	38	29	30
p	= 0.046				< 0.001			

RMSE displacement of inter-fraction tumor motion varied with AV biofeedback in 0.22 cm but it was larger with FB in 0.44 cm. Only one patient with AV biofeedback had more than 0.1 cm in RMSE displacement, compared to two patients with FB. In addition, the outlier motion ratio with AV biofeedback was between 24% and 42%, and it was also larger with FB between 31% and 50%. Inter-fraction variation of RMSE using AV biofeedback was reduced by 42% (p=0.046) in displacement and the outlier motion ratio was also decreased by 21% (p<0.001).

Figure 5-4 shows the distribution of tumor motion and the outlier motion for Patient 4 and 6 with FB and with AV biofeedback. A wide spread outlier motion in the same color bar scale indicates more variation of inter-fraction tumor motion.

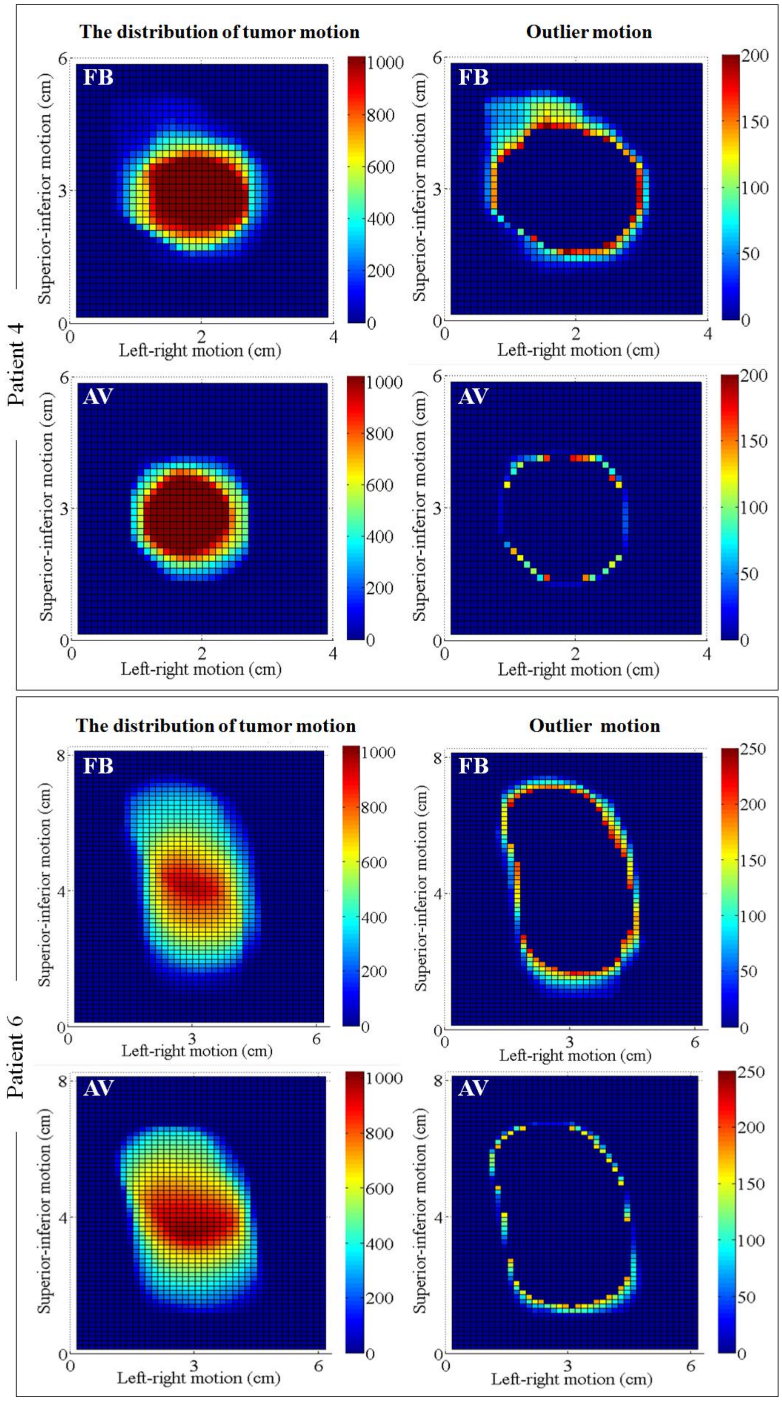

Figure 5-4. The distribution of tumor motion and the outlier motion measured

from coronal image datasets for Patients 4 and 6. The color bar scale indicates the ratio of the distribution of tumor motion.

A wide spread outlier motion with FB was found due to irregular tumor displacement (see FB sessions in Figure 5-3) in both patients whilst the comparatively regular tumor displacement (see AV biofeedback sessions in Figure 5-3) resulted in a smaller outlier motion with AV biofeedback. Subsequently, the color bar scale of outlier motion was smaller with AV biofeedback in both patients. The results of sagittal image datasets for Patients 4 and 6 are shown in Figure e1 (available online at www.redjournal.org).

5.4 Discussion

Medical imaging and radiation treatment in thoracic and abdominal regions often requires tumor motion management due to the variability of tumor motion pattern both intra-fractionally and inter-fractionally. In this work, we introduced AV biofeedback which utilizes the same guiding wave from the breathing training session customized for each patient in displacement and period across repeated MRI sessions to reduce intra and inter-fraction tumor motion consistency. Using AV biofeedback, we demonstrated the improvement of tumor motion consistency in intra-fraction displacement and period and inter-fraction displacement and period, and outlier motion whilst using the segmented tumor directly measured on coronal and sagittal cine-MR images.

Respiratory-induced thoracic and abdominal tumor motion varies with tumor size, location and patients,[127] and this study also demonstrated independent tumor locations and sizes through tumor auto-segmentation. Tumor motion also varied in an MRI session and across two MRI sessions, but it was improved with AV biofeedback compared with FB. In previous studies, intra-fraction regularity in displacement was improved by more than 50% (external abdomen)[74] and 38% (internal diaphragm).[76] This study demonstrated that the intra-fraction tumor motion consistency of all patients with AV biofeedback in Table 5-1 was improved by 34% and 73% in displacement and period, respectively. In addition, inter-fraction tumor motion consistency in Table 5-2 was improved by 42% in displacement and by 74% in period. Then, those significant improvements resulted in 21% reduction of the outlier motion ratio, directly linked to the minimization of the disagreement between planning and treatment resulting in more dose delivered to the tumor itself and less dose to the surrounding healthy tissue.[28-30, 145] Consequently, AV biofeedback can be applicable for respiratory motion management techniques, such as respiratory gating,[51] training[52] and breath-hold,[53] due to tumor motion consistency.

The external respiratory signal can be replaced with any respiratory signals such as ANZAI (AZ-733V, Anzai Medical Corporation, Tokyo, Japan)[146] and Bellows-belt,[113] and internal respiratory signals such as MR navigator[112] and electromagnetic transponder.[36] In addition, tumor motion from MR images could be used as the respiratory signal input for AV biofeedback. If tumor motion using a faster imaging[125] in MRI integrated with radiotherapy system[79, 88] is used for lung tumor motion management, real-time tumor deformation[147] can be utilized for image-guided AV biofeedback.

One of the limitations of the present study was that the inter-fraction changes were determined using only two MRI sessions, one before and the other in the middle of treatment. Tumor segmentation included manual work to set a seed point on an MR image and manual validation of the segmentation method.

We also skipped three to five images at the beginning of datasets due to the MR images being too bright. This study did not consider tumor deformation or out-of-plane motion. For better quantification of deformed tumor motion compared to only rigid motion, deformable image registration could be utilized, as well as 3D tumor motion using 3D MRI.[138]

5.5 Conclusions

This was the first study to directly evaluate the impact of audiovisual biofeedback on lung tumor motion in cine-MRI. By utilizing AV biofeedback, inter-fraction and intra-fraction tumor motion consistency was improved across two MRI sessions, spaced several weeks apart. AV biofeedback led to a 34% and 73% improvement of tumor motion consistency in intra-fraction displacement and period, respectively. AV biofeedback also led to an improvement of 42% and 74%, and 21% in inter-fraction displacement and period and outlier motion ratio, respectively. These results demonstrate that AV biofeedback can facilitate consistent lung tumor motion, which could be a desirable technique for achieving more accurate medical imaging and radiation therapy procedures.

Chapter 6: Audiovisual biofeedback guided breath-hold improves lung tumor position reproducibility and volume consistency

A version of this chapter has been submitted to Radiotherapy Oncology (2016): Lee D, Greer B P, Lapuz C, Ludbrook J, Arm J, Hunter P, Pollock S, Makhija K, O'Brien T R, Kim T and Keall P, "Audiovisual biofeedback guided breath-hold improves lung tumor position reproducibility and volume consistency".

ABSTRACT

Purpose: Respiratory variations can increase the variability of tumor position and volume, resulting in larger treatment margins and longer treatment times. Audiovisual biofeedback as a breath-hold technique can be utilized to reproduce tumor positions at inhalation and exhalation for the radiotherapy of moving lung tumors due to respiratory motion. This study assessed the impact of audiovisual biofeedback breath-hold (AVBH) on inter-fraction lung tumor position reproducibility and volume consistency for lung cancer radiotherapy.

Methods: Lung tumor position and volume were investigated in nine lung cancer patients who underwent a breath-hold training session with AVBH prior to two 3 Tesla (T) MRI sessions. In the first MRI session (pre-treatment), breath-hold MR images with (1) conventional breath-hold (CBH) using audio-instructions alone and (2) AVBH were acquired. The second MRI session (mid-treatment) was repeated within six weeks from the first session. Gross tumor volumes (GTV) were delineated on each dataset. CBH and AVBH were compared in terms of (1) tumor position reproducibility assessed by GTV centroid position and position range defined as the distance of GTV centroid positions between inhalation and exhalation, and (2) tumor volume consistency assessed by GTV between inhalation and exhalation.

Results: Compared to CBH, AVBH improved the reproducibility of inter-fraction GTV centroid position by 52% (p=0.002) from 6.6 mm to 3.2 mm and GTV position range by 74% (p=0.001) from 6.4 mm to 1.7 mm. Compared to CBH, AVBH also improved the consistency of intra-fraction GTVs by 70% (p=0.023) from 7.8 cm^3 to 2.5 cm^3.

Conclusions: This study demonstrated that audiovisual biofeedback can be utilized for improving the reproducibility and consistency of breath-hold lung tumor position and volume, respectively. These results may provide a pathway utilizing breath-hold procedures to achieve more accurate lung cancer radiation treatment, in addition to improving various medical imaging and treatments.

6.1 Introduction

Breath-hold techniques[53, 62, 63, 148-152] are often used to immobilize the movement of lung tumors, leading to reduced motion artifacts in medical imaging, and clinically meaningful tumor positions and shapes in respiratory-gated radiation treatment. In addition, the immobilization of lung tumors[148] can reduce phase shift between tumors and surrogates (i.e. chest, abdomen and diaphragm)[61] and system latency between tumor positioning and gating.[44] Immobilizing the tumor position is advantageous for reducing treatment margins and treatment delivery time.[53, 58]

Several breath-hold strategies have been studied and practiced to obtain the same level of breathing in repeated breath-holds. Deep inspiration breath-holds (DIBH) improved the reproducibility of intra- and inter-fraction target positions compared with free-breathing.[62, 63] Conventional breath-hold (inhalation and exhalation positions of free breathing) using the audio-instructions of a CT scanner (automated "Breathe in, breathe out, hold your breath" commands) reduced the variation of exhalation diaphragm positions compared with free-breathing.[148] Active breathing coordinator (ABC) forcibly suspends patient breathing without automated verbal or audio-instruction at pre-determined positions of lung volume. ABC has been demonstrated to improve the reproducibility of intra-fraction tumor position but still needs to improve large variations in inter-fraction tumor positions greater than 5 mm.[149, 150] Quasi-breath-hold (QBH) using successive short breath-holds (3, 5, or 7 seconds) have demonstrated equivalent or less motion variations while improving treatment efficiency.[151, 152] Visual biofeedback techniques[59, 60, 63, 151, 152] also reduce the uncertainty of target position by improving reproducibility of abdominal and chest wall positions, and pancreatic tumors using voluntary breath-hold techniques. However, lung tumor position reproducibility and volume consistency with the use of audio-visual guidance for inhalation and exhalation breath-holds for precise lung cancer radiation therapy has not been studied.

Audiovisual (AV) biofeedback,[51, 52, 73-76, 138] an interactive breathing guidance system has been employed to improve inhalation and exhalation breath-hold reproduciblity.[153] AV biofeedback consists of (1) tracking the respiratory motion of patients' abdomens using a real-time position management (RPM) system (Varian Medical Systems, Palo Alto, CA, USA) to form an individual guiding wave, (2) displaying their present breathing position and the guiding wave on a screen which patients can see, and (3) the patient controls their breathing to follow the guiding wave and holds their breathing at the inhalation and exhalation positions of the guiding wave when instructed.

Previous AV breath-hold (AVBH) results from healthy volunteers have demonstrated that the breath-hold reproducibility of inhalation and exhalation abdominal positions was improved whilst reducing image intensity variation over multiple breath-holds.[153] However, previous AVBH investigations have recruited healthy volunteers, so the impact of AVBH on tumor position and volume for lung cancer patients has not been examined.

In this study, we introduced a novel approach for AVBH for lung cancer patients, involving a breath-hold training session to obtain a guiding wave customized for each patient and utilizing the inhalation and exhalation breath-hold positions over two 3T MRI sessions. This study was the first investigation of the impact of AVBH on lung tumor position reproducibility and volume consistency, and used the direct measurement of gross tumor volume (GTV) from breath-hold high resolution 3D MR images.

6.2 Methods and Materials

6.2.1 Patients

Eleven patients who underwent radiation treatment between April 2013 and June 2015 were enrolled with their consent in an ethics-approved protocol. These patients met the following eligibility criteria: 1) Non-small-cell and small-cell lung cancers stage I-IIIB of any histology to be treated using radiation treatment; 2) ≥ 18 years old; 3) No gender or ethnic restrictions; 4) No pregnant women / mentally impaired subjects; and 5) No surgical clips, surgery metalware or pacemakers. The study comprised a breath-hold training session and two MRI sessions on different dates (pre- and mid-treatment). The breath-hold training session was scheduled on the same day of the first MRI session and the second MRI session was then repeated within three to six weeks depending on the duration of radiation treatment. The nine patients who completed the training and two MRI sessions are shown in Table 6-1. Two patients were excluded because they withdrew from the study prior to their second MRI session. The patients received a prescription dose of 40 ~ 60 Gy for primary lung cancer or for metastatic lung cancer at the isocenter in 15 ~ 30 fractions.

Table 6-1. Patient and disease characteristics.

Patient #	Gender	Age	Height (cm)	Weight (kg)	Stage	PS	Location	Glasses	Gy/fr	Hearing aid	Breath-hold (s)
P01	F	62	170	80	IIIA	0	RUL	Y	60/30	N	16
P02	F	61	158	72	IIA	1	RUL	Y	60/30	N	16
P03	F	66	165	66	IIIB	1	LUL	Y	40/15	N	16
P04	F	26	170	70	IIIA	1	LUL	N	50/20	N	16
P05	M	72	175	114	IIA	1	RLL	N	60/30	N	22
P06	M	54	170	84	IIIA	0	LUL	N	60/30	N	16
P07	M	55	180	69	IIIB	1	RUL	N	60/30	N	17
P08	M	79	168	80	IB	1	RUL	N	60/30	Y	16
P09	M	68	160	76	IIIA	1	LUL	Y	50/20	N	17

Abbreviations: P=Patient; PS = Eastern Cooperative Oncology Group performance status; RUL = right upper lobe; LUL = left upper lobe; RLL = right lower lobe; Gy = Gray; Fx = fractions;

6.2.2 Audiovisual biofeedback breath-hold training session

Each patient participated in a breath-hold training session (no imaging performed) in head first supine position to allow them to become comfortable with AVBH guidance. The workflow of AVBH is as follows (shown in Figure 6-1 (red arrows)): (1) monitor the breathing motion of the patient's abdomen using RPM to build a guiding wave calculated from the average of ten breathing cycles in a Fourier Series fit[74] (shown in Figure 6-1 (blue waves)), (2) display the real-time breathing position and the guiding wave on the patient's screen (shown in Figure 6-1 (visual display)), and (3) control their breathing to follow the guiding wave and hold their breath at inhalation or exhalation breath-hold position (shown in Figure 6-1 (red lines)) by following the verbal-instruction of radiographers.

Once inhalation and exhalation breath-hold positions were determined, patients were guided by AVBH and practiced breath-holds (first inhalation and second exhalation), as shown in Figure 6-1 (red lines). After each breath-hold practice, based on a consult with the patient, the inhalation and exhalation positions were set for the subsequent breath-hold MRI sessions.

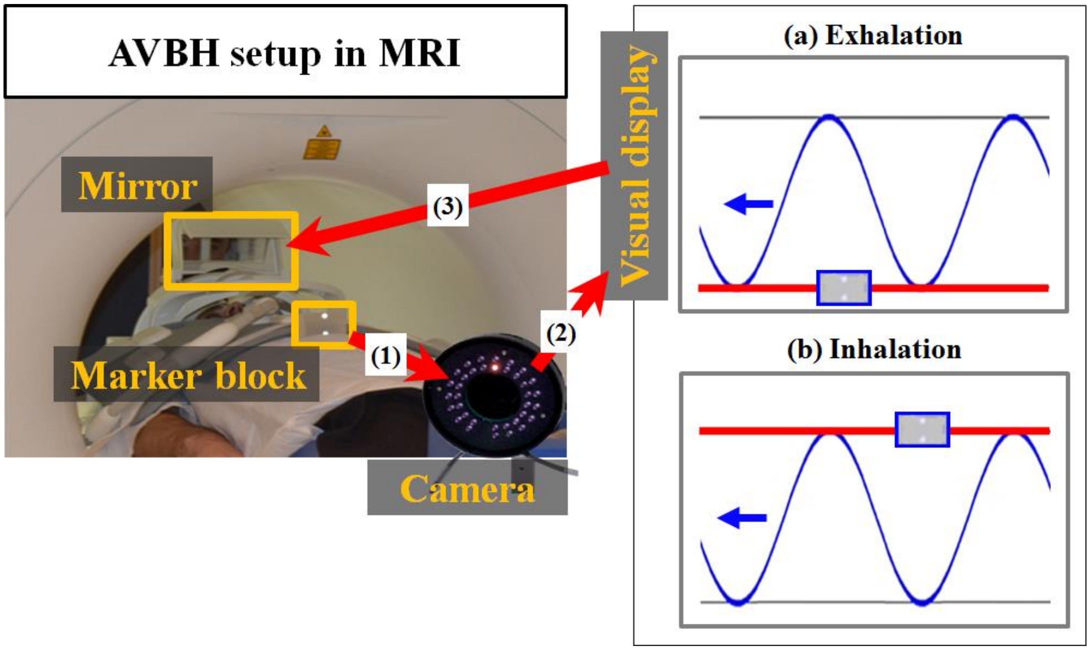

Figure 6-1. The AVBH setup in MRI. (a) Exhalation and (b) inhalation breath-hold positions (red line) of the guiding wave (blue line) for two MRI sessions.

For the AVBH setup in MRI, patients were positioned with an optical marker block on their abdomen to monitor their breathing motion. Display goggles for an AVBH training session were used and a head mounted mirror overlooking an MR-compatible projection screen was used (as shown in Figure 6-1) for the two MRI sessions. The gray marker block on the screen represents patients' actual breathing position and the red line indicates desired inhalation and exhalation breath-hold positions.

6.2.3 Magnetic resonance imaging with AVBH

High resolution three-dimensional (3D) MR images in head first supine position were obtained in a 3 Tesla MRI (Skyra, Siemens Healthcare Erlangen, Germany). For thoracic imaging, a VIBE (volumetric interpolated breath-hold examination) MR pulse sequence was used to acquire 160 slices per 3D MRI with an acquisition time between 16 and 22 seconds (see Table 6-1). Typical MR imaging parameters were repetition time (TR)/echo time (TE) = 2.24/0.88 ms, flip angle = 9°, field of view (width × height) = 368 × 380 mm^2, pixel size = 1.2 × 1.2 mm^2, slice thickness = 1.2 mm, bandwidth = 710 Hz, and image matrix = 310 × 320. For Patient 05 (P05 in Table 6-1), repetition time (TR)/echo time (TE) = 2.14/0.83 ms, field of view = 435 × 450 mm^2 and pixel size = 1.4 × 1.4 mm^2 due to the large field of view required.

In the first MRI session (pre-treatment), (3D exhalation and 3D inhalation) breath-hold MR images with (1) CBH and (2) AVBH were acquired, and the second MRI session (mid-treatment) was repeated within six weeks of the first session. Audio-instruction (MRI: Siemens Skyra) in CBH (i.e. “Breathe in, breathe out, hold your breath” or “Breathe out, breathe in, hold your breath”) and verbal-instruction (radiographers) in AVBH were used. For the verbal-instruction, radiographers continuously monitor patient’s breathing on an MR-compatible projection screen that displayed the real-time breathing position and the guiding wave, and verbally began to provide (1) the exhalation breath-hold instruction once patient’s breath reaches at inhalation position (“Breathe out, breathe in, breathe out, hold your breath”) and (2) the inhalation breath-hold instruction once patient’s breath reaches at exhalation position (“Breathe in, breathe out, breathe in, hold your breath”).

Eight datasets per patient (two image datasets (Inhalation and exhalation) × two breath-hold types (CBH and AVBH)) were obtained from two MRI sessions. Seventy two breath-hold datasets were obtained from nine lung cancer patients.

6.2.4 Lung tumor delineation

The gross tumor volume (GTV) of the seventy two breath-hold datasets was delineated by a radiation oncologist using Eclipse (Varian Medical Systems, Palo Alto, CA, USA). Rigid registration based on spinal vertebral anatomy was performed between the first and second MRI sessions. In this study, two rigid registrations were included per patient: (1) the exhalation dataset of the first MRI session with CBH to the exhalation dataset of the second MRI session with CBH and (2) the exhalation dataset of the first MRI session with AVBH to the exhalation dataset of the second MRI session with AVBH. During the rigid registration, the first and the second datasets were used for the fixed and moving datasets, respectively. Inhalation datasets were used for the rigid registrations because they were obtained at the beginning of the breath-hold image acquisition with CBH and AVBH.

6.2.5 Breath-hold lung tumor position and volume

For the impact of the use of AVBH on breath-hold lung tumors, (1) inter-fraction tumor position reproducibility across the first ($S1$) and the second ($S2$) MRI sessions was investigated in GTV centroid position and GTV position range, defined as the distance between inhalation and exhalation GTV centroids, and (2) intra-fraction tumor volume consistency between inhalation and exhalation GTVs in each MRI session.

(1) Inter-fraction tumor position reproducibility along each direction (LR: Left-Right, AP: Anterior-Posterior and SI: Superior-Inferior) using the following two equations and in 3D vector using 3D Euclidean distance.

- $The\ difference\ in\ the\ GTV\ centroid\ position = GTV^{S1}_{CENTROID} - GTV^{S2}_{CENTROID}.$

- $The\ difference\ in\ the\ GTV\ position\ range = ({}_{EXHALE}GTV^{S1}_{CENTROID} - {}_{INHALE}GTV^{S1}_{CENTROID}) - ({}_{EXHALE}GTV^{S2}_{CENTROID} - {}_{INHALE}GTV^{S2}_{CENTROID})$.

(2) Intra-fraction tumor volume consistency using the following equation.

- $The\ difference\ of\ GTV = {}_{INHALE}GTV - {}_{EXHALE}GTV$.

Quantitative statistical comparisons between CBH and AVBH were determined from the root mean square (RMS) along each direction and the 3D vector using the Wilcoxon signed rank test to evaluate the inter-fraction GTV centroid position and position range reproducibility, and intra-fraction GTV consistency.

6.3 Results

Figure 6-2 shows an example of breath-hold lung tumors with CBH and AVBH across two MRI sessions.

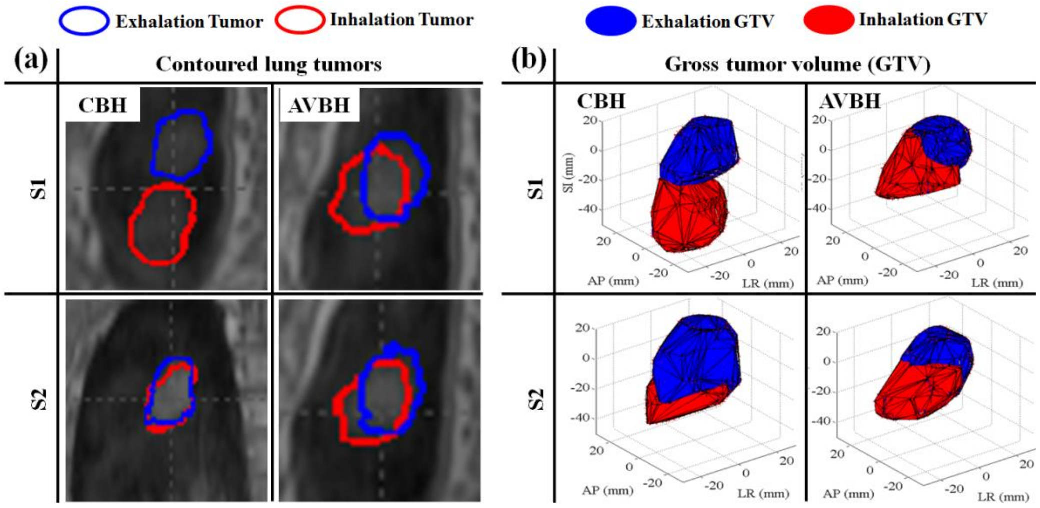

Figure 6-2. Lung tumors during CBH (left) and AVBH (right). (a) Contoured inhalation and exhalation breath-hold lung tumors, (b) corresponding inhalation and exhalation GTVs. S1: the first MRI session, S2: the second MRI session.

Table 6-2. The difference in the GTV centroid position with CBH and AVBH from seventy two breath-hold datasets across two MRI sessions.

Patients	The GTV centroid position difference (mm), $GTV^{S1}_{CENTROID} - GTV^{S2}_{CENTROID}$								
	CBH					AVBH			
	BHP	LR	AP	SI	3D vector	LR	AP	SI	3D vector
P01	E	−3.5	1.4	−3.3	5.0	2.5	4.8	3.9	6.6
	I	−1.5	14.0	11.1	18.0	2.3	4.9	5.1	7.4
P02	E	1.3	−3.2	−6.9	7.7	3.7	2.6	−5.0	6.7
	I	0.5	−2.7	−5.1	5.8	0.7	3.2	−5.7	6.6
P03	E	−9.7	−2.6	9.9	14.1	−3.1	−4.7	9.5	11.1
	I	−7.5	−11.4	6.2	15.0	−3.2	−3.4	6.4	7.9
P04	E	−2.7	0.0	3.7	4.6	−1.0	−0.6	7.2	7.3
	I	−2.7	5.6	6.6	9.0	−1.4	−0.6	1.9	2.5
P05	E	5.9	−0.8	−6.2	8.6	2.7	−1.8	−0.2	3.3
	I	0.6	−4.2	−27.8	28.1	1.8	−1.2	1.1	2.5
P06	E	6.0	3.0	7.4	10.0	5.0	4.2	2.7	7.1
	I	10.3	11.6	10.3	18.6	4.1	3.8	2.5	6.2
P07	E	−4.5	4.3	−0.4	6.2	0.7	0.6	1.7	2.0
	I	−6.1	2.5	−0.3	6.6	−0.8	2.8	1.2	3.1
P08	E	−0.2	2.2	−0.4	2.3	1.2	1.6	0.6	2.0
	I	−1.5	−9.5	4.1	10.4	1.7	1.9	0.6	2.6
P09	E	0.6	−2.6	−2.2	3.5	1.4	0.0	−1.5	2.1

	I	−0.5	−6.4	1.2	6.5	2.4	2.8	2.1	4.3
RMS		**4.8**	**6.3**	**8.8**	**11.8**	**2.5**	**3.0**	**4.2**	**5.7**

Abbreviations: P = Patient; BHP = Breath-hold positions; LR = left-right; AP = anterior-posterior’ SI = superior-inferior; 3D vector = $\sqrt{LR^2 + AP^2 + SI^2}$; E = Exhalation; I = Inhalation; RMS = Root mean square.

In Table 6-2, compared with CBH, the reproducibility of the inter-fraction GTV centroid position with AVBH was improved by 51.6% (*p*=0.002) from 6.6 mm (the RMS average of each direction) to 3.2 mm and 51.9% (*p*=0.002) from 11.8 mm (the RMS of 3D vector) to 5.7 mm. The GTV centroid position difference in the 3D vector greater than 10 mm using CBH was seen in 7/18 GTVs across five patients and only 1/18 GTVs using AVBH in one patient. For both CBH and AVBH, the largest GTV centroid position difference was found in the SI followed by the AP and LR. In terms of inhalation and exhalation GTV centroid positions, the exhalation GTV centroid position difference with CBH was 4.3 mm (the RMS average of each direction) and it was 8.2 mm for the inhalation GTV centroid position. For AVBH, the differences in the exhalation and inhalation GTV centroid positions were 3.4 mm and 3.0 mm respectively, corresponding to an improvement in reproducibility by 21% and 63% compared to CBH.

Table 6-3. The difference in the GTV position range across two MRI sessions.

Patients	The GTV position range difference (mm), $\left({}_{EXHALE}GTV^{S1}_{CENTROID} - {}_{INHALE}GTV^{S1}_{CENTROID}\right) - \left({}_{EXHALE}GTV^{S2}_{CENTROID} - {}_{INHALE}GTV^{S2}_{CENTROID}\right)$							
	CBH				AVBH			
	LR	AP	SI	3D vector	LR	AP	SI	3D vector
P01	−1.9	−12.0	−14.5	18.9	0.2	−0.1	−1.2	1.2

P02	0.8	−0.5	−1.7	2.0	3.1	−0.6	0.8	3.2
P03	−2.2	8.8	3.7	9.8	0.0	−1.3	3.1	3.4
P04	−0.1	−5.6	−2.8	6.2	0.4	0.0	5.3	5.3
P05	5.3	3.8	21.6	22.6	0.9	−0.6	−1.3	1.7
P06	−4.3	−8.6	−2.9	10.0	0.8	0.4	0.2	0.9
P07	1.6	1.8	−0.1	2.4	1.5	−2.2	0.6	2.7
P08	1.4	11.7	−4.5	12.6	−0.6	−0.3	−0.1	0.6
P09	1.1	3.7	−3.4	5.2	−1.0	−2.9	−3.5	4.7
RMS	**2.6**	**7.4**	**9.1**	**12.0**	**1.3**	**1.3**	**2.5**	**3.1**

In Table 6-3, compared with CBH, the reproducibility of the inter-fraction GTV position range with AVBH was improved by 73.5% (*p*=0.001) from 6.4 mm (the RMS average of each direction) to 1.7 mm, and also 74.4% (*p*=0.039) from 12.0 mm (the RMS of 3D vector) to 3.1 mm. The GTV position range difference with CBH varied between −14.5 mm and 21.6 mm, whilst it was between −3.5 mm and 5.3 mm for AVBH. The GTV position range in the LR and AP had the smallest difference for AVBH but it was twice and approximately six times smaller than the LR and AP position ranges using CBH, respectively. The GTV position range difference was smaller with AVBH compared to CBH except for P02 and P07 where the position range was comparable or slightly larger.

Table 6-4. The difference in inhalation and exhalation GTVs with CBH and AVBH in each MRI session. A negative value indicates that the GTV was larger in the inhalation GTV and a positive value indicates that it was smaller.

Patients	Sessions	Gross tumor volume (cm^3)					
		CBH			AVBH		
		Exhale	Inhale	Exhale – Inhale	Exhale	Inhale	Exhale – Inhale
P01	S1	23.9	18.7	5.3	22.1	20.6	1.4
	S2	14.4	16.3	-2.0	15.5	14.1	1.4
P02	S1	68.7	79.3	-10.5	80.0	83.9	-3.8
	S2	62.1	66.7	-4.6	61.4	64.3	-2.9
P03	S1	16.7	17.7	-1.0	20.3	20.0	0.3
	S2	3.5	4.6	-1.1	9.7	8.6	1.2
P04	S1	18.6	16.6	2.0	16.9	16.1	0.7
	S2	9.6	9.6	0.0	9.1	9.1	0.0
P05	S1	19.8	16.5	3.3	19.9	19.3	0.6
	S2	18.8	24.4	-5.5	18.1	17.7	0.4
P06	S1	74.2	69.2	5.0	71.5	75.3	-3.9
	S2	58.9	58.9	0.0	57.5	57.7	-0.2
P07	S1	131.0	159.5	-28.6	146.0	138.6	7.4
	S2	100.8	102.9	-2.1	103.9	103.0	0.9
P08	S1	78.3	73.5	4.8	79.1	82.3	-3.2
	S2	45.6	46.4	-0.8	44.6	46.2	-1.6
P09	S1	56.3	57.8	-1.5	55.6	55.7	-0.1
	S2	42.6	44.2	-1.6	46.6	45.0	1.6
RMS		**57.9**	**62.4**	**7.8**	**60.8**	**60.6**	**2.5**

In Table 6-4, compared with CBH, the difference in the intra-fraction GTV with AVBH was improved by 70% (p=0.023) from 7.8 cm^3 (CBH) to 2.5 cm^3 (AVBH).

Inhalation GTV with CBH was 4.5 cm^3 larger than exhalation GTV in 57.9 cm^3 and 62.4 cm^3 but inhalation and exhalation GTVs with AVBH in RMS were almost identical in 60.8 cm^3 and 60.7 cm^3. Similarly, the decrease of GTV between pre- and mid-treatment was 20.4 cm^3 (p=0.001) in CBH and 20.3 cm^3 (p<0.001) in AVBH. However, using AVBH, inhalation and exhalation GTVs were identical in both S1 (69.7 cm^3 and 69.3 cm^3) and S2 (50.3 cm^3 and 50.4 cm^3), whilst using CBH they varied in both S1 (65.2 cm^3 and 71.9 cm^3) and S2 (49.5 cm^3 and 51.2 cm^3).

6.4 Discussion

Medical imaging, patient setup,[154] and radiation treatment[53, 149] often requires the immobilization of lung tumors to reduce the magnitude of errors introduced by respiratory motion. In this study, we introduced AVBH which utilized the same breath-hold positions from the breath-hold training session across two MRI sessions to study lung tumor position and volume. Using AVBH, we demonstrated the improvement of inter-fraction lung tumor position reproducibility by 52% and intra-fraction volume consistency by 70% using GTV directly measured from 3D MR images.

Our current results for CBH can be compared with a previous study by Brock *et al.* measured the inhalation lung tumor position variation with respect to bony anatomy using CT scan with ABC breath hold from pre- and mid-treatment.[149] They found the mean of the absolute difference between the tumor positions was 3.6 mm, 3.5 mm and 5.1 mm in the LR, AP and SI, respectively. These findings are similar to our CBH MRI results of 3.6 mm, 4.9 mm and 6.3 mm in the LR, AP and SI, respectively. With AVBH in our study, the values were significantly reduced to 2.2 mm, 2.5 mm and 3.2 mm in the LR, AP and SI, respectively. From the similarity of the CBH results we can hypothesize that the use of AVBH with CT and ABC would yield similar 52% reductions in lung tumor position variations.

A practical and effective use of breath-hold techniques requires the breath-hold training session for patient comfort,[155] composed of a series of breath-holds at inhalation and exhalation positions and customizing the patient's breath-hold level. Consequently, lung tumor position reproducibility using AVBH can be improved across breath-hold MRI sessions, led to a consistent reproducibility of inhalation and exhalation breath-hold lung tumor positions, and resulted in a consistent decrease of inhalation and exhalation GTVs. In addition to a previously reported finding of up to 40% shrinkage during the course of radiation treatment,[33, 34, 156] this study found a 40% shrinkage of both inhalation and exhalation GTVs with AVBH between pre-treatment and mid-treatment. Our results indicate that an accurate lung tumor position with AVBH can be observed at the same level of respiration during the course of radiation treatment.[155]

Various internal and external respiratory signals as an input to AVBH can be utilized for the tumor motion management of thoracic and abdominal regions[60] to immobilize the target motion during medical imaging and radiation treatment, which could lead to the reduction of tumor motion margins,[58] and therefore the corresponding dose to the lung and heart.[53, 157] Inhalation and exhalation breath-hold MRI is an effective technique to determine lung tumor position and volume information for patient setup and treatment planning.[44, 158]

This study has two main limitations. First, that the inter-fraction changes were measured using only two MRI sessions, one (pre-treatment) and the other (mid-treatment) and therefore we can only hypothesize how generally this can be applied to a multi-fraction treatment. Second, the lung tumors were manually contoured by a physician so intra-observer errors, known to be a significant error source, may be present in our data.

6.5 Conclusions

This study was the first to assess the impact of audiovisual biofeedback on breath-hold lung tumor position and volume in breath-hold MRI. AVBH resulted in an improvement of inter-fraction tumor position reproducibility across two MRI sessions by an average of 3.4 mm (52%) along each direction and 6.1 mm (52%) in 3D vector, and also an improvement of intra-fraction tumor volume consistency by 5.3 cm^3 (70%) in each MRI session. These results demonstrate that AVBH can facilitate reproducible lung tumor breath-hold position and consistent volume, which could be a desirable technique for medical imaging and radiation therapy procedures.

Chapter 7: Audiovisual biofeedback improves image quality and reduces scan time for respiratory-gated 3D MRI

A version of this chapter has been published: Lee D, Greer B P, J, Arm J, Kim T and Keall P, " Audiovisual biofeedback improves image quality and reduces scan time for respiratory-gated 3D MRI.", Journal of Physics: Conference Series, ***489*** *(1), 012033,* *http://dx.doi.org/10.1088/1742-6596/489/1/012033*.

ABSTRACT

The purpose of this study was to test the hypothesis that audiovisual (AV) biofeedback can improve image quality and reduce scan time for respiratory-gated 3D thoracic MRI. For five healthy human subjects respiratory motion guidance in MR scans was provided using an AV biofeedback system, utilizing real-time respiratory motion signals. To investigate the improvement of respiratory-gated 3D MR images between free breathing (FB) and AV biofeedback (AV), each subject underwent two imaging sessions. Respiratory-related motion artifacts and imaging time were qualitatively evaluated in addition to the reproducibility of external (abdominal) motion. In the results, 3D MR images in AV biofeedback showed more anatomic information such as a clear distinction of diaphragm, lung lobes and sharper organ boundaries. The scan time was reduced from 401±215 s in FB to 334±94 s in AV (*p-value* 0.36). The root mean square variation of the displacement and period of the abdominal motion was reduced from 0.4±0.22 cm and 2.8±2.5 s in FB to 0.1±0.15 cm

and 0.9±1.3 s in AV (*p-value* of displacement <0.01 and *p-value* of period 0.12). This study demonstrated that audiovisual biofeedback improves image quality and reduces scan time for respiratory-gated 3D MRI. These results suggest that AV biofeedback has the potential to be a useful motion management tool in medical imaging and radiation therapy procedures.

7.1 Introduction

Respiratory-related motion blurring and ghost artifacts[159] can be reduced using respiratory-gating techniques with RF navigator[160], respiratory bellows belt[113], or real-time position management system (RPM).[51] However, variations in cycle-to-cycle breathing can cause inadequate respiratory-gating in image acquisition, resulting in image artifacts and increased scan time.[161]

Audiovisual (AV) biofeedback was proposed to monitor real-time respiratory motion using a marker on the abdomen with feedback to the human subject for respiratory motion management.[73, 74, 76, 162] A number of respiratory cycles are acquired at the beginning of AV biofeedback to prepare a guiding waveform for each subject and the guiding waveform is displayed. The regular respiration can be reproduced in that the subject matches the red ball corresponding to the present respiratory position of the subject to the guiding waveform. AV biofeedback has been previously demonstrated to improve breathing regularity in 2D MRI[76] but not in 3D MRI. The aim of this study is thus to investigate whether AV biofeedback improves image quality and reduces scan time for respiratory-gated 3D MRI.

7.2 Methods

7.2.1 AV biofeedback system setup in MRI

An AV biofeedback system has been employed to provide respiratory guidance during MR scans. Figure 7-1 shows the experimental setup of the AV biofeedback system for MRI. The respiratory motion signals were obtained using the real-time position management (RPM) system (Varian, Palo Alto, USA) consisting of an infrared camera and a marker block on the abdomen.

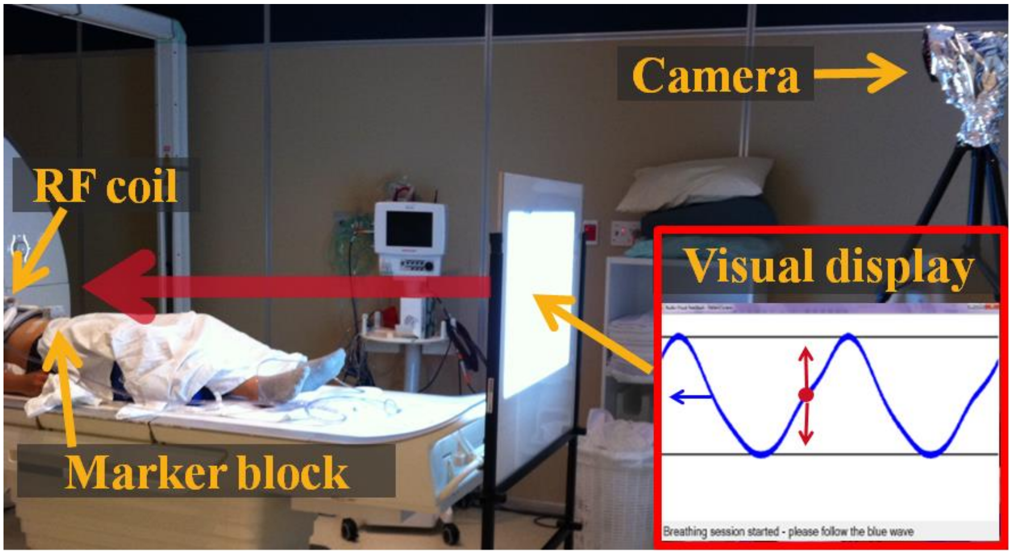

Breathing session started - please follow the blue wave

Figure 7-1 AV biofeedback system for respiratory-gated 3D MR imaging in a 3T Skyra Siemens MRI.

To guide real-time patient breathing in a 3T system (Skyra, Siemens Healthcare Erlangen, Germany), the visual display of the guiding waveform and red ball was displayed on a screen during MR imaging. An 18-channel body matrix coil for thoracic imaging and a head mounted mirror for the patient's view of the visual display were used.

7.2.2 Respiratory-gated 3D MRI

The improvement in respiratory-gated 3D MR images using the AV biofeedback system combined with thoracic MRI was investigated with five healthy male subjects (aged 33 ± 6). For thoracic imaging, T2-weighted 3D SPACE (Sampling Perfection with Application optimized Contrast using different angle Evolutions) MR pulse sequence with an RF navigator placed on liver dome was employed. Typical parameters were TR/TE = 2200/89 ms, flip angle = 170^0, FOV = 380×380 mm^2, voxel size = $1.19 \times 1.19 \times 4$ mm^3 and image matrix = $320 \times 320 \times 52$.

In this study, each subject underwent two sessions to assess the image quality and gating efficiency with (AV: AV biofeedback) and without (FB: Free breathing). In order to reduce the effect of AV training on the FB results, a 15 – 20 minute AV training session was performed after the FB session and before the AV session. Respiratory-gated 3D MR images were acquired at three gating target positions with designated acceptance windows in the MR pulse sequence. The gating target positions at 10% (near maximum exhalation), 50% (middle) and 90% (near maximum inhalation) were set with a ±2 mm or ±4 mm acceptance window range.

The improvement of respiratory-gated 3D MR images using the AV biofeedback has been evaluated in terms of respiratory-related artifacts. The gating efficiency and the 3D MR data acquisition time have been compared. The abdominal motion was evaluated using the root mean square error (RMSE) in displacement and period obtained from the RPM system.

7.3 Results and Discussion

7.3.1 Image quality and gating efficiency improvement

Using the AV biofeedback system, respiratory-related blurring artifacts have been noticeably improved and scan time was considerably reduced as shown in Figure 7-2.

3D MR images with FB (subject 1 and subject 2) were significantly blurred due to the variation of the baseline shift and amplitude in respiration. In contrast, there was noticeable reduction of blurring artifacts due to the more regular respiratory motion in the same subjects with AV (subject 1 and subject 2). 3D MR images in AV included more anatomic information such as a clear distinction of diaphragm and lung lobes. In addition, the edge and intersection of organs on 3D images were sharpened.

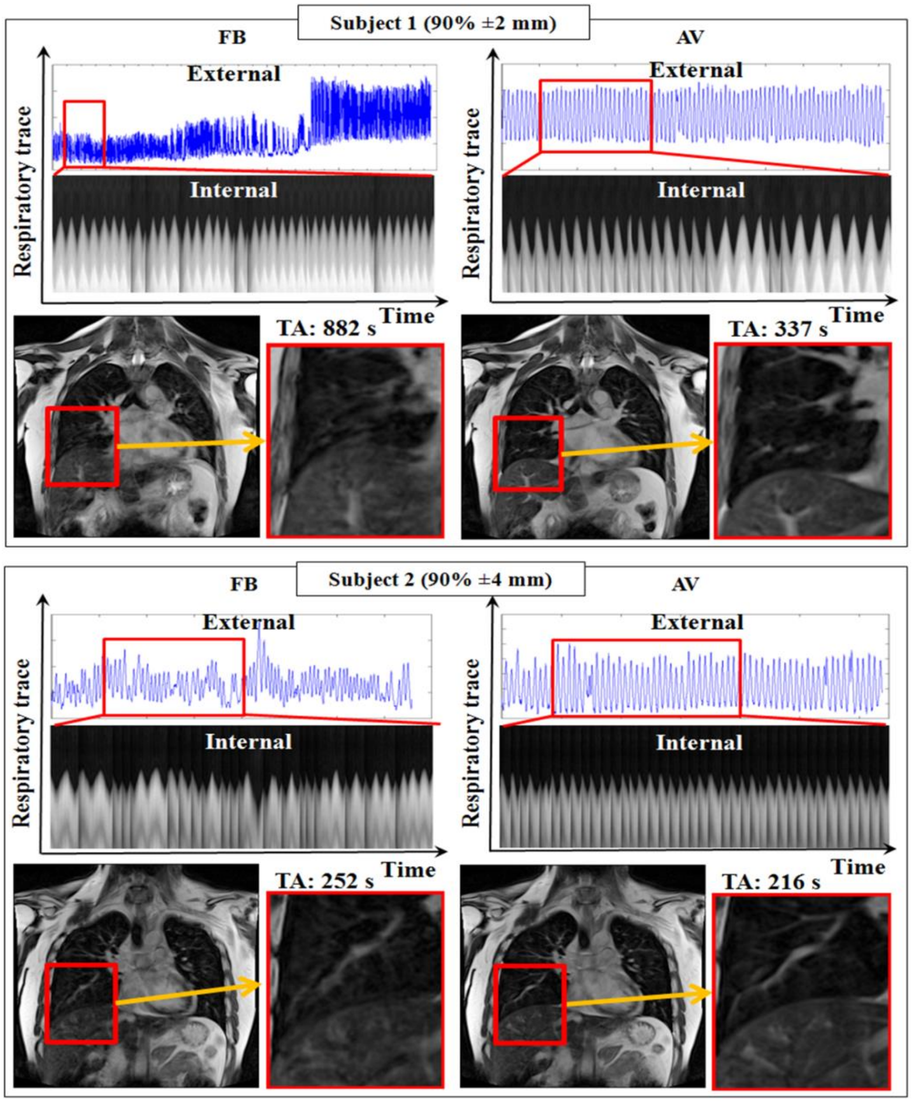

Figure 7-2. An example of improved image quality and total acquisition time (TA) when AV biofeedback was employed during gated 3D MR imaging for subject 1 (top) and subject 2 (bottom). Free-breathing results (left) and AV results (right) are shown. The external respiratory signal, internal diaphragm signal and images are shown. Gating was triggered at 90% of the breathing cycle (near maximum inhalation) with ±2 mm (subject 1) and ±4 mm (subject 2) gating thresholds. The regular external (abdomen) respiration correlated with the regular internal

(diaphragm) respiration, leading to better image quality and shorter scan time.

In addition, regular respiratory motion using AV biofeedback reduced the incidence of unsuccessful gating, leading to a reduction of MR scan time. The scan time reduced up to 545 s and 36 s during respiratory-gated 3D MRI at 90% acceptance window in subject 1 and 2, respectively. A ±2 mm range required relatively longer MR scan time, compared to ±4 mm range, to acquire the same number of images due to the small range of acceptance window. In other volunteer cases, the considerable gating efficiency in AV compared to FB was found at 10% and 90% acceptance windows but it was quite similar at 50% acceptance window between the two breathing conditions.

The impact of AV biofeedback for gating target positions corresponding to the three acceptance positions is shown in Figure 7-3.

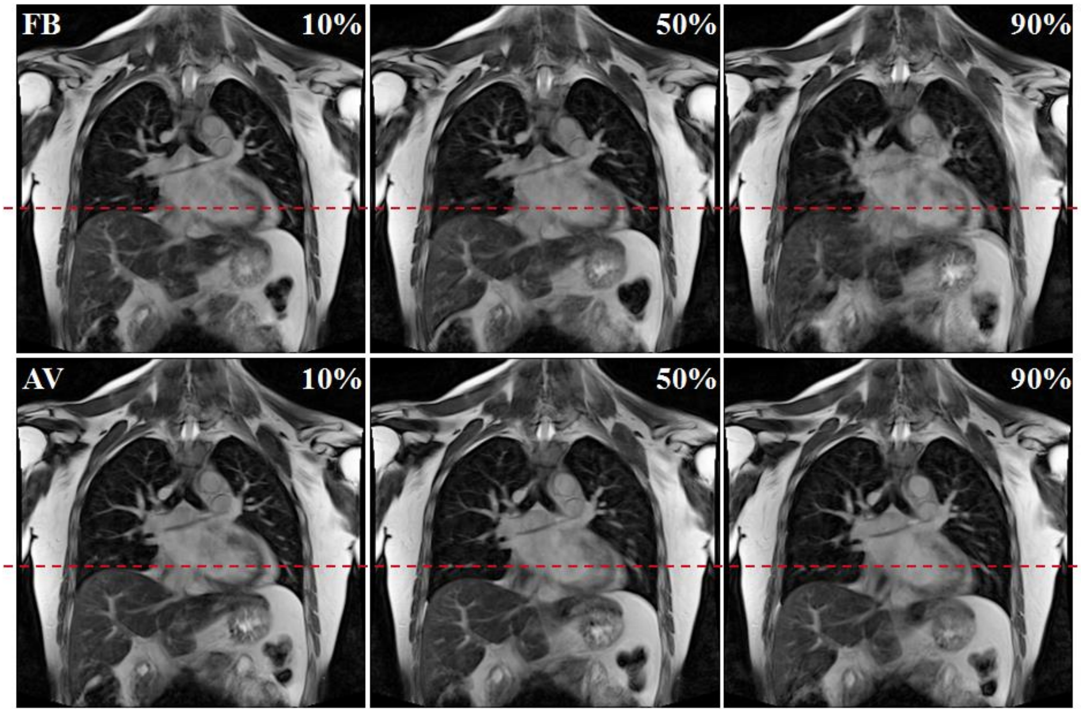

Figure 7-3. Improvement of gating target positions corresponding to the three acceptance windows in AV compared to FB (subject 1).

A red dashed line at the top of the diaphragm for the 10% gated scan shows only small differences in the diaphragm positions for FB, however there is clearer evidence of inspiration for the MR scan where the inferior motion of the diaphragm with inspiration is apparent.

7.3.2 Scan time and breathing variation

Scan time was reduced (or similar) at all gating target positions due to the improvement of breathing regularity: the reduction of root mean square error (RMSE) in displacement and period in Table 7-1.

Table 7-1. Scan time and breathing variation of respiratory-gated 3D MRI.

Session	Average scan time (s)	RMSE in Average variation in displacement (cm)	RMSE in Average variation in Period (s)
FB	401 ± 21	0.4 ± 0.22	2.8 ± 2.5
AV	334 ± 94	0.1 ± 0.15	0.9 ± 1.3
% reduction with AV	17%	75%	68%
p-values	0.36	<0.01	0.12

An average reduction in scan time was from 401 s in FB to 334 s in AV, coming from the reduction of breathing variation in displacement (–75%) and period (–68%).

This study demonstrated the improvement of respiratory-gated 3D MR images with AV biofeedback due to improved respiratory motion reproducibility, leading to regular internal organ displacement. In addition, scan time was simultaneously reduced. The images in this study spanned the thorax and abdomen, indicating that AV biofeedback can be broadly applicable to imaging sites affected by respiration, provided that both a respiratory signal and a patient display system are available.

A limitation of the current study was that healthy human subject volunteers, and not patients, were used. Therefore, without further testing, the application of this study can only be extended to patients with similar age and lung function characteristics to the volunteers, for example some lymphoma, breast, pancreas and kidney cancer patients. In order to investigate the potential benefits of AV biofeedback for a quite different population, lung cancer patients, a clinical study has been initiated.

A potential problem for real-time audiovisual biofeedback is the time delay between the patient breathing and the projected signal. Fortunately, using the 30 Hz RPM signal the time delay between the patient breathing and the projected signal is undetectable to the user. However, with a different respiratory monitor with either a lower frame rate and/or using more processing time the projected real-time respiratory signal could be delayed or discontinuous. For such systems it is likely that further processing algorithms, such as signal prediction or smoothing algorithms would be needed.

7.4 Conclusions

This study demonstrated, for the first time, that audiovisual biofeedback improves image quality and reduces scan time for respiratory-gated 3D MRI. These results suggest that AV biofeedback has the potential to be a useful motion management tool in medical imaging and radiation therapy procedures.

Chapter 8: Summary and future work

Real-time image guidance can reduce variability in lung tumour motion, thus improving cancer radiotherapy outcomes for thoracic and abdominal regions. Based on the results from this thesis, the dynamic keyhole method could increase the temporal resolution by a factor of five, when compared with full k-space methods. The increase in temporal resolution can compensate the system latency of tracking and gating techniques for clinical applications such as real-time tumour monitoring in image-guided radiotherapy.

Respiratory guidance can control variability in tumour motion, position and volume, thus improving cancer radiotherapy outcomes for thoracic and abdominal regions. Based on the results from this thesis, AV biofeedback compared with CBH significantly improved (1) intra- and inter-fraction tumour motion consistency, resulted in the reduction of the outlier motion ratio, (2) inter-fraction lung tumour position reproducibility and intra-fraction lung tumour volume consistency and (3) image quality with shorter scan time for 3D thoracic images.

This thesis has described the achievements of the dynamic keyhole method and AV biofeedback respiratory guidance. These results are evident that the dynamic keyhole method can provide a pathway to achieve more accurate tumour information and AV biofeedback can provide the potential to be a useful motion management tool for lung cancer radiotherapy. For further advantages of a technique offering an image of sufficient quality, the dynamic keyhole method could be prospectively implemented to directly measure real-time tumour motion and shape translation for image- and MRI-guided radiotherapy. In addition, AV biofeedback could be utilized for tumour motion guidance required that reproducible tumour motion and consistent tumour shape through the course of radiotherapy.

For future work, the dynamic keyhole method could be clinical implemented to achieve a reduction in scan time without compromising image quality for real-time tumour information, which could provide clinical benefits to thoracic and abdominal cancer patients.

Bibliography

1. Siegel RL, Miller KD, Jemal A. Cancer statistics, 2015. CA: a cancer journal for clinicians 2015;65(1): 5-29.

2. Australian Institute of Health and Welfare 2014. Cancer in Australia: an overview, 2014. Cancer series no. 78. Cat. no. CAN 75. Canberra: AIHW. Available from URL: http://www.aihw.gov.au/WorkArea/DownloadAsset.aspx?id=60129550202.

3. Barton MB, Jacob S, Shafiq J, et al. Estimating the demand for radiotherapy from the evidence: a review of changes from 2003 to 2012. Radiotherapy and Oncology 2014;112(1): 140-44.

4. Keall PJ, Mageras GS, Balter JM, et al. The management of respiratory motion in radiation oncology report of AAPM Task Group 76. Medical physics 2006;33(10): 3874-900.

5. Shah AP, Kupelian PA, Waghorn BJ, et al. Real-time tumor tracking in the lung using an electromagnetic tracking system. International Journal of Radiation Oncology* Biology* Physics 2013;86(3): 477-83.

6. Haas ML. Advances in radiation therapy for lung cancer. Seminars in oncology nursing: Elsevier, 2008:34-40.

7. Erasmus JJ, Sabloff BS. CT, positron emission tomography, and MRI in staging lung cancer. Clinics in chest medicine 2008;29(1): 39-57.

8. Lardinois D, Weder W, Hany TF, et al. Staging of non–small-cell lung cancer with integrated positron-emission tomography and computed tomography. New England Journal of Medicine 2003;348(25): 2500-07.

9. Webb W, Gatsonis C, Zerhouni E, et al. CT and MR imaging in staging non-small cell bronchogenic carcinoma: report of the Radiologic Diagnostic Oncology Group. Radiology 1991;178(3): 705-13.

10. Hsieh J. Computed tomography: principles, design, artifacts, and recent advances: SPIE Bellingham, WA, 2009.
11. Ito M, Ikeda K, Nishiguchi M, et al. Multi-detector row CT imaging of vertebral microstructure for evaluation of fracture risk. Journal of bone and mineral research 2005;20(10): 1828-36.
12. Pearce MS, Salotti JA, Little MP, et al. Radiation exposure from CT scans in childhood and subsequent risk of leukaemia and brain tumours: a retrospective cohort study. The Lancet 2012;380(9840): 499-505.
13. Nehmeh S, Erdi Y, Pan T, et al. Four-dimensional (4D) PET/CT imaging of the thorax. Medical physics 2004;31(12): 3179-86.
14. Nehmeh SA, Erdi YE, Ling CC, et al. Effect of respiratory gating on quantifying PET images of lung cancer. Journal of Nuclear Medicine 2002;43(7): 876-81.
15. Spaepen K, Stroobants S, Dupont P, et al. Prognostic value of positron emission tomography (PET) with fluorine-18 fluorodeoxyglucose ([18F] FDG) after first-line chemotherapy in non-Hodgkin’s lymphoma: is [18F] FDG-PET a valid alternative to conventional diagnostic methods? Journal of Clinical Oncology 2001;19(2): 414-19.
16. Huang B, Law MW-M, Khong P-L. Whole-body PET/CT scanning: estimation of radiation dose and cancer risk 1. Radiology 2009;251(1): 166-74.
17. Li G, Citrin D, Camphausen K, et al. Advances in 4D medical imaging and 4D radiation therapy. Technology in cancer research & treatment 2008;7(1): 67-81.
18. Keall P. 4-dimensional computed tomography imaging and treatment planning. Seminars in radiation oncology: Elsevier, 2004:81-90.

19. Ue H, Haneishi H, Iwanaga H, Suga K. Nonlinear motion correction of respiratory-gated lung SPECT images. Medical Imaging, IEEE Transactions on 2006;25(4): 486-95.

20. Parker W, Patrocinio H. Clinical treatment planning in external photon beam radiotherapy. Podgorsak, I 2005.

21. Jones D. ICRU report 50—prescribing, recording and reporting photon beam therapy. Medical physics 1994;21(6): 833-34.

22. Wambersie A, Landgerg T. ICRU Report 62: Prescribing, Recording and Reporting Photon Beam Therapy. ICRU Publ Bethesda MD 1999.

23. Chang JY, Dong L, Liu H, et al. Image–Guided Radiation Therapy for Non–small Cell Lung Cancer. Journal of Thoracic Oncology 2008;3(2): 177-86.

24. Jaffray DA. Image-guided radiotherapy: from current concept to future perspectives. Nature Reviews Clinical Oncology 2012;9(12): 688-99.

25. Galvin JM. The multileaf collimator: a complete guide. Proc. AAPM annual meeting, 1999.

26. Otto K. Volumetric modulated arc therapy: IMRT in a single gantry arc. Medical physics 2008;35(1): 310-17.

27. Hugo G, Vargas C, Liang J, Kestin L, Wong JW, Yan D. Changes in the respiratory pattern during radiotherapy for cancer in the lung. Radiotherapy and oncology 2006;78(3): 326-31.

28. Yamamoto T, Langner U, Loo BW, Shen J, Keall PJ. Retrospective analysis of artifacts in four-dimensional CT images of 50 abdominal and thoracic radiotherapy patients. International Journal of Radiation Oncology* Biology* Physics 2008;72(4): 1250-58.

29. Balter JM, Ten Haken RK, Lawrence TS, Lam KL, Robertson JM. Uncertainties in CT-based radiation therapy treatment planning associated with patient breathing. International Journal of Radiation Oncology* Biology* Physics 1996;36(1): 167-74.
30. Ge J, Santanam L, Noel C, Parikh PJ. Planning 4-dimensional computed tomography (4DCT) cannot adequately represent daily intrafractional motion of abdominal tumors. International Journal of Radiation Oncology* Biology* Physics 2013;85(4): 999-1005.
31. Nøttrup TJ, Korreman SS, Pedersen AN, et al. Intra-and interfraction breathing variations during curative radiotherapy for lung cancer. Radiotherapy and oncology 2007;84(1): 40-48.
32. Suh Y, Dieterich S, Cho B, Keall PJ. An analysis of thoracic and abdominal tumour motion for stereotactic body radiotherapy patients. Physics in medicine and biology 2008;53(13): 3623.
33. Britton KR, Starkschall G, Tucker SL, et al. Assessment of gross tumor volume regression and motion changes during radiotherapy for non–small-cell lung cancer as measured by four-dimensional computed tomography. International Journal of Radiation Oncology* Biology* Physics 2007;68(4): 1036-46.
34. Erridge SC, Seppenwoolde Y, Muller SH, et al. Portal imaging to assess set-up errors, tumor motion and tumor shrinkage during conformal radiotherapy of non-small cell lung cancer. Radiotherapy and Oncology 2003;66(1): 75-85.
35. Murphy MJ. Tracking moving organs in real time. Seminars in radiation oncology: Elsevier, 2004:91-100.

36. Keall PJ, Colvill E, O’Brien R, et al. The first clinical implementation of electromagnetic transponder-guided MLC tracking. Medical physics 2014;41(2): 020702.

37. Gendrin C, Furtado H, Weber C, et al. Monitoring tumor motion by real time 2D/3D registration during radiotherapy. Radiotherapy and oncology 2012;102(2): 274-80.

38. Shirato H, Shimizu S, Shimizu T, Nishioka T, Miyasaka K. Real-time tumour-tracking radiotherapy. The Lancet 1999;353(9161): 1331-32.

39. Ng JA, Booth JT, Poulsen PR, et al. Kilovoltage intrafraction monitoring for prostate intensity modulated arc therapy: first clinical results. International Journal of Radiation Oncology* Biology* Physics 2012;84(5): e655-e61.

40. Park S-J, Ionascu D, Hacker F, Mamon H, Berbeco R. Automatic marker detection and 3D position reconstruction using cine EPID images for SBRT verification. Medical physics 2009;36(10): 4536-46.

41. Keall P, Todor A, Vedam S, et al. On the use of EPID-based implanted marker tracking for 4D radiotherapy. Medical physics 2004;31(12): 3492-99.

42. Berbeco RI, Hacker F, Ionascu D, Mamon HJ. Clinical feasibility of using an EPID in CINE mode for image-guided verification of stereotactic body radiotherapy. International Journal of Radiation Oncology* Biology* Physics 2007;69(1): 258-66.

43. Li HH, Rodriguez VL, Green OL, et al. Patient-Specific Quality Assurance for the Delivery of 60 Co Intensity Modulated Radiation Therapy Subject to a 0.35-T Lateral Magnetic Field. International Journal of Radiation Oncology* Biology* Physics 2015;91(1): 65-72.

44. Mutic S, Dempsey JF. The ViewRay System: Magnetic Resonance–Guided and Controlled Radiotherapy. Seminars in radiation oncology: Elsevier, 2014:196-99.

45. Lagendijk JJ, Raaymakers BW, van Vulpen M. The magnetic resonance imaging–linac system. Seminars in radiation oncology: Elsevier, 2014:207-09.

46. Fallone BG. The rotating biplanar linac–magnetic resonance imaging system. Seminars in radiation oncology: Elsevier, 2014:200-02.

47. Keall PJ, Barton M, Crozier S. The Australian magnetic resonance imaging–linac program. Seminars in radiation oncology: Elsevier, 2014:203-06.

48. KRILAVIČIUS T, MAN K. Timed model of the radiation therapy system with respiratory motion compensation 2011.

49. Krilavicius T, Zliobaite I, Simonavicius H, Jarusevicius L. Predicting respiratory motion for real-time tumour tracking in radiotherapy. arXiv preprint arXiv:1508.00749 2015.

50. Hoogeman M, Prévost J-B, Nuyttens J, Pöll J, Levendag P, Heijmen B. Clinical accuracy of the respiratory tumor tracking system of the cyberknife: assessment by analysis of log files. International Journal of Radiation Oncology* Biology* Physics 2009;74(1): 297-303.

51. Kini VR, Vedam SS, Keall PJ, Patil S, Chen C, Mohan R. Patient training in respiratory-gated radiotherapy. Medical Dosimetry 2003;28(1): 7-11.

52. George R, Vedam S, Chung T, Ramakrishnan V, Keall P. The application of the sinusoidal model to lung cancer patient respiratory motion. Medical physics 2005;32(9): 2850-61.

53. Murphy MJ, Martin D, Whyte R, Hai J, Ozhasoglu C, Le Q-T. The effectiveness of breath-holding to stabilize lung and pancreas tumors during radiosurgery.

International Journal of Radiation Oncology* Biology* Physics 2002;53(2): 475-82.

54. Wong JW, Sharpe MB, Jaffray DA, et al. The use of active breathing control (ABC) to reduce margin for breathing motion. International Journal of Radiation Oncology* Biology* Physics 1999;44(4): 911-19.

55. Heinzerling JH, Anderson JF, Papiez L, et al. Four-dimensional computed tomography scan analysis of tumor and organ motion at varying levels of abdominal compression during stereotactic treatment of lung and liver. International Journal of Radiation Oncology* Biology* Physics 2008;70(5): 1571-78.

56. Eccles CL, Patel R, Simeonov AK, Lockwood G, Haider M, Dawson LA. Comparison of liver tumor motion with and without abdominal compression using cine-magnetic resonance imaging. International Journal of Radiation Oncology* Biology* Physics 2011;79(2): 602-08.

57. Wunderink W, Romero AM, De Kruijf W, De Boer H, Levendag P, Heijmen B. Reduction of respiratory liver tumor motion by abdominal compression in stereotactic body frame, analyzed by tracking fiducial markers implanted in liver. International Journal of Radiation Oncology* Biology* Physics 2008;71(3): 907-15.

58. Engelsman M, Sharp G, Bortfeld T, Onimaru R, Shirato H. How much margin reduction is possible through gating or breath hold? Physics in medicine and biology 2005;50(3): 477.

59. Nakamura K, Shioyama Y, Nomoto S, et al. Reproducibility of the abdominal and chest wall position by voluntary breath-hold technique using a laser-based

monitoring and visual feedback system. International Journal of Radiation Oncology* Biology* Physics 2007;68(1): 267-72.

60. Nakamura M, Shibuya K, Shiinoki T, et al. Positional reproducibility of pancreatic tumors under end-exhalation breath-hold conditions using a visual feedback technique. International Journal of Radiation Oncology* Biology* Physics 2011;79(5): 1565-71.

61. Yan H, Yin F-F, Zhu G-P, Ajlouni M, Kim JH. The correlation evaluation of a tumor tracking system using multiple external markers. Medical physics 2006;33(11): 4073-84.

62. Hanley J, Debois MM, Mah D, et al. Deep inspiration breath-hold technique for lung tumors: the potential value of target immobilization and reduced lung density in dose escalation. International Journal of Radiation Oncology* Biology* Physics 1999;45(3): 603-11.

63. Peng Y, Vedam S, Chang JY, et al. Implementation of feedback-guided voluntary breath-hold gating for cone beam CT-based stereotactic body radiotherapy. International Journal of Radiation Oncology* Biology* Physics 2011;80(3): 909-17.

64. Darby SC, McGale P, Taylor CW, Peto R. Long-term mortality from heart disease and lung cancer after radiotherapy for early breast cancer: prospective cohort study of about 300 000 women in US SEER cancer registries. The lancet oncology 2005;6(8): 557-65.

65. Kumar A, Welti D, Ernst RR. NMR Fourier zeugmatography. Journal of magnetic resonance 2011;213(2): 495-509.

66. Brigham EO, Morrow R. The fast Fourier transform. Spectrum, IEEE 1967;4(12): 63-70.

67. Metcalfe P, Liney G, Holloway L, et al. The potential for an enhanced role for MRI in radiation-therapy treatment planning. Technology in cancer research & treatment 2013;12(5): 429-46.

68. Lustig M, Donoho DL, Santos JM, Pauly JM. Compressed sensing MRI. Signal Processing Magazine, IEEE 2008;25(2): 72-82.

69. Scheffler K, Hennig J. Reduced circular field-of-view imaging. Magnetic resonance in medicine 1998;40(3): 474-80.

70. Peters DC, Korosec FR, Grist TM, et al. Undersampled projection reconstruction applied to MR angiography. Magnetic resonance in medicine 2000;43(1): 91-101.

71. Meyer CH, Hu BS, Nishimura DG, Macovski A. Fast spiral coronary artery imaging. Magnetic resonance in medicine 1992;28(2): 202-13.

72. Jackson J, Meyer CH, Nishimura DG, Macovski A. Selection of a convolution function for Fourier inversion using gridding [computerised tomography application]. Medical Imaging, IEEE Transactions on 1991;10(3): 473-78.

73. George R, Chung TD, Vedam SS, et al. Audio-visual biofeedback for respiratory-gated radiotherapy: impact of audio instruction and audio-visual biofeedback on respiratory-gated radiotherapy. International Journal of Radiation Oncology* Biology* Physics 2006;65(3): 924-33.

74. Venkat RB, Sawant A, Suh Y, George R, Keall PJ. Development and preliminary evaluation of a prototype audiovisual biofeedback device incorporating a patient-specific guiding waveform. Physics in medicine and biology 2008;53(11): N197.

75. Cui G, Gopalan S, Yamamoto T, Berger J, Maxim PG, Keall PJ. Commissioning and quality assurance for a respiratory training system based on audiovisual biofeedback. Journal of applied clinical medical physics/American College of Medical Physics 2010;11(4): 3262.

76. Kim T, Pollock S, Lee D, O’Brien R, Keall P. Audiovisual biofeedback improves diaphragm motion reproducibility in MRI. Medical physics 2012;39(11): 6921-28.

77. Pollock S, Lee D, Keall P, Kim T. Audiovisual biofeedback improves motion prediction accuracy. Medical physics 2013;40(4): 041705.

78. Lu W, Neuner GA, George R, et al. Audio-Visual Biofeedback Does Not Improve the Reliability of Target Delineation Using Maximum Intensity Projection in 4-Dimensional Computed Tomography Radiation Therapy Planning. International Journal of Radiation Oncology* Biology* Physics 2014;88(1): 229-35.

79. Raaymakers B, Lagendijk J, Overweg J, et al. Integrating a 1.5 T MRI scanner with a 6 MV accelerator: proof of concept. Physics in medicine and biology 2009;54(12): N229.

80. Keall PJ, Cattell H, Pokhrel D, et al. Geometric accuracy of a real-time target tracking system with dynamic multileaf collimator tracking system. Int J Radiat Oncol Biol Phys 2006;65(5): 1579-84.

81. Cervino LI, Du J, Jiang SB. MRI-guided tumor tracking in lung cancer radiotherapy. Physics in medicine and biology 2011;56(13): 3773.

82. Xu H-X, Lu M-D, Liu L-N, Guo L-H. Magnetic navigation in ultrasound-guided interventional radiology procedures. Clinical radiology 2012;67(5): 447-54.

83. Seimenis I, Tsekos NV, Keroglou C, Eracleous E, Pitris C, Christoforou EG. An approach for preoperative planning and performance of MR-guided interventions demonstrated with a manual manipulator in a 1.5 T MRI scanner. Cardiovascular and interventional radiology 2012;35(2): 359-67.

84. Sharp GC, Jiang SB, Shimizu S, Shirato H. Prediction of respiratory tumour motion for real-time image-guided radiotherapy. Physics in medicine and biology 2004;49(3): 425.

85. Steel H, Pollock S, Lee D, Keall P, Kim T. The internal–external respiratory motion correlation is unaffected by audiovisual biofeedback. Australasian Physical & Engineering Sciences in Medicine 2014: 1-6.

86. Keall PJ, Mageras GS, Balter JM, et al. The management of respiratory motion in radiation oncology report of AAPM Task Group 76. Medical physics 2006;33: 3874.

87. Chida K, Kaga Y, Haga Y, et al. Occupational Dose in Interventional Radiology Procedures. American Journal of Roentgenology 2013;200(1): 138-41.

88. Kolling S, Oborn B, Keall P. Impact of the MLC on the MRI field distortion of a prototype MRI-linac. Medical physics 2013;40(12): 121705.

89. Dempsey JF. System and method for image guidance during medical procedures: WO Patent App. PCT/US2011/066,605, 2011.

90. Fallone B, Murray B, Rathee S, et al. First MR images obtained during megavoltage photon irradiation from a prototype integrated linac-MR system. Medical physics 2009;36: 2084.

91. Uecker M, Zhang S, Voit D, Karaus A, Merboldt KD, Frahm J. Real-time MRI at a resolution of 20 ms. NMR in Biomedicine 2010;23(8): 986-94.

92. Zhang S, Olthoff A, Frahm J. Real-time magnetic resonance imaging of normal swallowing. Journal of Magnetic Resonance Imaging 2012.

93. Niebergall A, Zhang S, Kunay E, et al. Real-time MRI of speaking at a resolution of 33 ms: Undersampled radial FLASH with nonlinear inverse reconstruction. Magnetic resonance in medicine 2012.

94. Wood ML, Henkelman RM. MR image artifacts from periodic motion. Medical physics 1985;12: 143.

95. Van Vaals JJ, Brummer ME, Thomas Dixon W, et al. “Keyhole” method for accelerating imaging of contrast agent uptake. Journal of Magnetic Resonance Imaging 1993;3(4): 671-75.

96. Yang RK, Roth CG, Ward RJ, Mitchell DG. Optimizing Abdominal MR Imaging: Approaches to Common Problems1. Radiographics 2010;30(1): 185-99.

97. Duerk JL, Lewin JS, Wu DH. Application of keyhole imaging to interventional MRI: a simulation study to predict sequence requirements. Journal of Magnetic Resonance Imaging 1996;6(6): 918-24.

98. Hanson JM, Liang ZP, Wiener EC, Lauterbur PC. Fast dynamic imaging using two reference images. Magnetic resonance in medicine 1996;36(1): 172-75.

99. Glover G, Pauly J. Projection reconstruction techniques for reduction of motion effects in MRI. Magnetic resonance in medicine 2005;28(2): 275-89.

100. Meyer CH, Hu BS, Nishimura DG, Macovski A. Fast spiral coronary artery imaging. Magnetic resonance in medicine 2005;28(2): 202-13.

101. Block KT, Uecker M, Frahm J. Undersampled radial MRI with multiple coils. Iterative image reconstruction using a total variation constraint. Magnetic resonance in medicine 2007;57(6): 1086-98.

102. Peters DC, Rohatgi P, Botnar RM, Yeon SB, Kissinger KV, Manning WJ. Characterizing radial undersampling artifacts for cardiac applications. Magnetic resonance in medicine 2006;55(2): 396-403.

103. Smith DS, Gore JC, Yankeelov TE, Welch EB. Real-Time Compressive Sensing MRI Reconstruction Using GPU Computing and Split Bregman Methods. International Journal of Biomedical Imaging 2012;2012.

104. Baraniuk RG. Compressive sensing [lecture notes]. Signal Processing Magazine, IEEE 2007;24(4): 118-21.

105. Song R, Tipirneni A, Johnson P, Loeffler RB, Hillenbrand CM. Evaluation of respiratory liver and kidney movements for MRI navigator gating. Journal of Magnetic Resonance Imaging 2011;33(1): 143-48.

106. Wade O. Movements of the thoracic cage and diaphragm in respiration. The Journal of physiology 1954;124(2): 193-212.

107. Korin HW, Ehman RL, Riederer SJ, Felmlee JP, Grimm RC. Respiratory kinematics of the upper abdominal organs: a quantitative study. Magnetic resonance in medicine 1992;23(1): 172-78.

108. Davies S, Hill A, Holmes R, Halliwell M, Jackson P. Ultrasound quantitation of respiratory organ motion in the upper abdomen. British journal of radiology 1994;67(803): 1096-102.

109. Stemmer A, Kiefer B. Phase navigator for respiratory triggering. Proceedings of the 18th Annual Meeting of ISMRM, Stockholm, Sweden (2010).

110. Carlson J, Minemura T. Imaging time reduction through multiple receiver coil data acquisition and image reconstruction. Magnetic resonance in medicine 2005;29(5): 681-87.

111. Deshmane A, Gulani V, Griswold MA, Seiberlich N. Parallel MR imaging. Journal of Magnetic Resonance Imaging 2012;36(1): 55-72.

112. Spincemaille P, Nguyen TD, Prince MR, Wang Y. Kalman filtering for real-time navigator processing. Magnetic resonance in medicine 2008;60(1): 158-68.

113. Santelli C, Nezafat R, Goddu B, et al. Respiratory bellows revisited for motion compensation: Preliminary experience for cardiovascular MR. Magnetic resonance in medicine 2011;65(4): 1097-102.

114. Li XA, Stepaniak C, Gore E. Technical and dosimetric aspects of respiratory gating using a pressure-sensor motion monitoring system. Medical physics 2006;33: 145.

115. Lujan AE, Larsen EW, Balter JM, Ten Haken RK. A method for incorporating organ motion due to breathing into 3D dose calculations. Medical physics 1999;26(5): 715-20.

116. Vedam S, Keall P, Docef A, Todor D, Kini V, Mohan R. Predicting respiratory motion for four-dimensional radiotherapy. Medical physics 2004;31(8): 2274-83.

117. Gierga DP, Brewer J, Sharp GC, Betke M, Willett CG, Chen GT. The correlation between internal and external markers for abdominal tumors: implications for respiratory gating. International Journal of Radiation Oncology* Biology* Physics 2005;61(5): 1551-58.

118. Seppenwoolde Y, Shirato H, Kitamura K, et al. Precise and real-time measurement of 3D tumor motion in lung due to breathing and heartbeat, measured during radiotherapy. International Journal of Radiation Oncology* Biology* Physics 2002;53(4): 822-34.

119. Ionascu D, Jiang SB, Nishioka S, Shirato H, Berbeco RI. Internal-external correlation investigations of respiratory induced motion of lung tumors. Medical physics 2007;34(10): 3893-903.

120. Lagendijk JJ, Raaymakers BW, Raaijmakers AJ, et al. MRI/linac integration. Radiotherapy and Oncology 2008;86(1): 25-29.

121. Mutic S, Dempsey JF. The ViewRay System: Magnetic Resonance–Guided and Controlled Radiotherapy. Seminars in radiation oncology 2014;24(3): 196-99.

122. Bjerre T, Crijns S, af Rosenschöld PM, et al. Three-dimensional MRI-linac intra-fraction guidance using multiple orthogonal cine-MRI planes. Physics in medicine and biology 2013;58(14): 4943.

123. Lee D, Greer P, Arm J, Keall P, Kim T. Audiovisual biofeedback improves image quality and reduces scan time for respiratory-gated 3D MRI. Journal of Physics: Conference Series 2014;489(1): 012033.

124. Kim T, Pollock S, Lee D, O'Brien R, Keall P. Audiovisual biofeedback improves diaphragm motion reproducibility in MRI. Medical physics 2012;39: 6921.

125. Lee D, Pollock S, Whelan B, Keall P, Kim T. Dynamic keyhole: A novel method to improve MR images in the presence of respiratory motion for real-time MRI. Medical physics 2014;41(7): 072304.

126. Feng M, Balter JM, Normolle D, et al. Characterization of pancreatic tumor motion using cine MRI: surrogates for tumor position should be used with caution. International Journal of Radiation Oncology* Biology* Physics 2009;74(3): 884-91.

127. Stevens CW, Munden RF, Forster KM, et al. Respiratory-driven lung tumor motion is independent of tumor size, tumor location, and pulmonary function. International Journal of Radiation Oncology* Biology* Physics 2001;51(1): 62-68.

128. Otsu N. A threshold selection method from gray-level histograms. Automatica 1975;11(285-296): 23-27.

129. Lewis C, Prato F, Drost D, Nicholson R. Comparison of respiratory triggering and gating techniques for the removal of respiratory artifacts in MR imaging. Radiology 1986;160(3): 803-10.

130. Keall P, Kini V, Vedam S, Mohan R. Motion adaptive x-ray therapy: a feasibility study. Physics in medicine and biology 2001;46(1): 1.

131. Sarma M, Hu P, Rapacchi S, et al. Accelerating Dynamic Magnetic Resonance Imaging (MRI) for Lung Tumor Tracking Based on Low-Rank Decomposition in the Spatial–Temporal Domain: A Feasibility Study Based on Simulation and Preliminary Prospective Undersampled MRI. International Journal of Radiation Oncology* Biology* Physics 2014;88(3): 723-31.

132. Smith RP, Bloch P, Harris EE, et al. Analysis of interfraction and intrafraction variation during tangential breast irradiation with an electronic portal imaging device. International Journal of Radiation Oncology* Biology* Physics 2005;62(2): 373-78.

133. Juhler Nøttrup T, Korreman SS, Pedersen AN, et al. Intra-and interfraction breathing variations during curative radiotherapy for lung cancer. Radiotherapy and oncology 2007;84(1): 40-48.

134. Liu HH, Balter P, Tutt T, et al. Assessing respiration-induced tumor motion and internal target volume using four-dimensional computed tomography for radiotherapy of lung cancer. International Journal of Radiation Oncology* Biology* Physics 2007;68(2): 531-40.

135. Matsugi K, Narita Y, Sawada A, et al. Measurement of interfraction variations in position and size of target volumes in stereotactic body radiotherapy for lung cancer. International Journal of Radiation Oncology* Biology* Physics 2009;75(2): 543-48.

136. Yamamoto T, Langner U, Loo Jr BW, Shen J, Keall PJ. Retrospective analysis of artifacts in four-dimensional CT images of 50 abdominal and thoracic

radiotherapy patients. International Journal of Radiation Oncology* Biology* Physics 2008;72(4): 1250-58.

137. Ge J, Santanam L, Yang D, Parikh PJ. Accuracy and consistency of respiratory gating in abdominal cancer patients. International Journal of Radiation Oncology* Biology* Physics 2013;85(3): 854-61.

138. Lee D, Greer P, Arm J, Keall P, Kim T. Audiovisual biofeedback improves image quality and reduces scan time for respiratory-gated 3D MRI. Journal of Physics: Conference Series: IOP Publishing, 2014:012033.

139. Steel H, Pollock S, Lee D, Keall P, Kim T. The internal–external respiratory motion correlation is unaffected by audiovisual biofeedback. Australasian Physical & Engineering Sciences in Medicine 2014;37(1): 97-102.

140. Keall P, Yang J, Yamamoto T, et al. SU-D-17A-04: The Impact of Audiovisual Biofeedback On Image Quality During 4D Functional and Anatomic Imaging: Results of a Prospective Clinical Trial. Medical Physics 2014;41(6): 117-17.

141. Pollock S, Lee D, Kim T, et al. SU-E-J-142: Respiratory Guidance for Lung Cancer Patients: An Investigation of Audiovisual Biofeedback Training and Effectiveness. Medical Physics 2013;40(6): 183-83.

142. Fitzpatrick MJ, Starkschall G, Antolak JA, et al. Displacement-based binning of time-dependent computed tomography image data sets. Med Phys 2006;33(1): 235-46.

143. Gonzalez RC, Woods RE, Eddins SL. Digital image processing using MATLAB. New Jersey, Pearson Prentice Hall, 2004.

144. Akino Y, Oh R-J, Masai N, Shiomi H, Inoue T. Evaluation of potential internal target volume of liver tumors using cine-MRI. Medical physics 2014;41(11): 111704.

145. Van Herk M. Errors and margins in radiotherapy. Seminars in radiation oncology: Elsevier, 2004:52-64.

146. Li XA, Stepaniak C, Gore E. Technical and dosimetric aspects of respiratory gating using a pressure-sensor motion monitoring system. Medical physics 2006;33(1): 145-54.

147. Ge Y, O'Brien RT, Shieh C-C, Booth JT, Keall PJ. Toward the development of intrafraction tumor deformation tracking using a dynamic multi-leaf collimator. Medical physics 2014;41(6): 061703.

148. Berson AM, Emery R, Rodriguez L, et al. Clinical experience using respiratory gated radiation therapy: comparison of free-breathing and breath-hold techniques. International Journal of Radiation Oncology* Biology* Physics 2004;60(2): 419-26.

149. Brock J, McNair HA, Panakis N, Symonds-Tayler R, Evans PM, Brada M. The Use of the Active Breathing Coordinator Throughout Radical Non–Small-Cell Lung Cancer (NSCLC) Radiotherapy. International Journal of Radiation Oncology* Biology* Physics 2011;81(2): 369-75.

150. Kaza E, Symonds-Tayler R, Collins D, et al. First MRI application of an active breathing coordinator. Physics in medicine and biology 2015;60(4): 1681.

151. Park Y-K, Kim S, Kim H, Kim IH, Lee K, Ye S-J. Quasi-breath-hold technique using personalized audio-visual biofeedback for respiratory motion management in radiotherapy. Medical physics 2011;38(6): 3114-24.

152. Kim T, Kim S, Park Y-K, Youn KK, Keall P, Lee R. Motion management within two respiratory-gating windows: feasibility study of dual quasi-breath-hold technique in gated medical procedures. Physics in medicine and biology 2014;59(21): 6583.

153. Kim T, Pollock S, Lee D, Keall P. Audiovisual Biofeedback Improves Anatomical Position Management in Breath-hold. International Journal of Radiation Oncology* Biology* Physics 2012;84(3): S216.

154. Nakamura M, Akimoto M, Ono T, et al. Interfraction positional variation in pancreatic tumors using daily breath-hold cone-beam computed tomography with visual feedback. Journal of Applied Clinical Medical Physics 2015;16(2).

155. Keall PJ, Mageras GS, Balter JM, et al. The management of respiratory motion in radiation oncology report of AAPM Task Group 76a). Medical physics 2006;33(10): 3874-900.

156. Kupelian PA, Ramsey C, Meeks SL, et al. Serial megavoltage CT imaging during external beam radiotherapy for non–small-cell lung cancer: Observations on tumor regression during treatment. International Journal of Radiation Oncology* Biology* Physics 2005;63(4): 1024-28.

157. Vikström J, Hjelstuen MH, Mjaaland I, Dybvik KI. Cardiac and pulmonary dose reduction for tangentially irradiated breast cancer, utilizing deep inspiration breath-hold with audio-visual guidance, without compromising target coverage. Acta Oncologica 2011;50(1): 42-50.

158. Wooten HO, Green O, Yang M, et al. Quality of Intensity Modulated Radiation Therapy Treatment Plans Using a (60) Co Magnetic Resonance Image Guidance Radiation Therapy System. International journal of radiation oncology, biology, physics 2015;92(4): 771-78.

159. Wood ML, Henkelman RM. MR image artifacts from periodic motion. Medical physics 1985;12(2): 143-51.

160. Taylor AM, Jhooti P, Wiesmann F, Keegan J, Firmin DN, Pennell DJ. MR navigator-echo monitoring of temporal changes in diaphragm position:

Implications for MR coronary angiography. Journal of Magnetic Resonance Imaging 1997;7(4): 629-36.

161. Hu Y, Caruthers SD, Low DA, Parikh PJ, Mutic S. Respiratory amplitude guided 4-dimensional magnetic resonance imaging. International Journal of Radiation Oncology* Biology* Physics 2013;86(1): 198-204.

162. Yang J, Yamamoto T, Cho B, Seo Y, Keall PJ. The impact of audio-visual biofeedback on 4D PET images: Results of a phantom study. Medical physics 2012;39(2): 1046-57.